Addis Ababa University
አዲስ አበባ ዩኒቨርሲቲ
Seek Wisdom, Elevate your Intellect and Serve Humanity

SCHOOOL OF GRADUATE STUDIES

COLLEGE OF NATURAL AND COMPUTATIONAL SCIENCES

SCHOOL OF EARTH SCIENCES

Assessment of geothermal sources using integrated geophysical methods: a case study of the Aluto-Langano geothermal field and its environs, Central Main Ethiopian Rift, Ethiopia

A thesis submitted to

The School of Graduate Studies of Addis Ababa University in partial fulfillment of the requirements for the degree of Master of Science in Applied Geophysics

By

Gemeda Demissie

Addis Ababa University

Addis Ababa, Ethiopia

June, 2021

ADDIS ABABA UNIVERSITY

SCHOOL OF GRADUATE STUDIES

SCHOOL OF EARTH SCEINCES

This is to certify that the thesis prepared by **Gemeda Demissie**, entitled: "**Assessment of geothermal sources using integrated geophysical methods: a case study of the Aluto-Langano geothermal field and its environs, Central Main Ethiopian Rift, Ethiopia**" and submitted in partial fulfillment of the requirements for the degree of Master of Science in Applied Geophysics complies with the regulations of the university and meets the accepted standards with respect to originality and quality.

Approved by examining committee:	Signature	Date
Dr. Balemwal Atnafu	_____	_____
(Head, School of Earth Sciences)		
Dr. Abera Alemu	_____	_____
(Advisor)		

(Internal examiner)	_____	_____

(External Examiner)	_____	_____

DECLARATION

I, the undersigned, hereby declare that the thesis entitled with "**Assessment of geothermal sources using integrated geophysical methods: a case study of the Aluto-Langano geothermal field and its environs, Central Main Ethiopian Rift, Ethiopia**" is my original work carried out under the supervision of Dr. Abera Alemu and has not been presented to any university or institution for the award of any degree or diploma program and all sources of materials used for the thesis are duly acknowledged.

Name of the candidate	Signature	Date
Gemeda Demissie	_____	_____

This is to certify that the above declaration made by the candidate is correct to the best of my knowledge and it has been submitted for examination with my approval as university advisor.

Advisor name	Signature	Date
Dr. Abera Alemu	_____	_____
(Advisor)		

ABSTRACT

The Main Ethiopian Rift is one of the world's most tectonically active areas with widespread volcanisms and enhanced geothermal gradient. However, the areal extent, nature and depth of the geothermal resources remain imprecise. The study area which mainly comprises the Aluto-Langano geothermal field, the Munesa escarpment and the Gedemota ridge is located in the central part of the Main Ethiopian Rift. The Aluto-Langano geothermal field is bounded by Lake Ziway to the north, Lake Langano to the southeast and Lake Abiyata to the southwest. The hydraulic gradient of Lake Ziway dips towards the south and is thought to feed water to the Aluto-Langano geothermal. The Aluto-Langano geothermal system encompasses younger NNE-SSW oriented en-echelon faults of the WFB and NE-SW oriented boarder faults. The fault systems belonging to the WFB are generally thought to generate fracturing of rocks that could favor the development of geothermal reservoirs beneath the study area. Gravity and magnetic studies constrained by the available geological, borehole and geophysical data are conducted over an area consisting of the Aluto-Langano geothermal field and its environs. Data enhancement techniques (upward continuation, analytical signal, tilt derivative, Euler deconvolution and reduction to pole) have been applied to the observed gravity and magnetic data in order to isolate the effects of deep seated and shallow origin geologic sources. Interpretations of the gravity and magnetic data in combination with the available data (seismic, geological and well-log data) have provided important clue about the geothermal sources of the study area. 2D gravity models computed for the study area and running across and along the rift axis reveal six density layers (silicic products, lacustrine sediments, basalts, Tertiary ignimbrite, Mesozoic sediments and crystalline basements). The computed 2D gravity models show occurrence of a magma chamber/intrusion occurring at depths between 2km and 3km beneath the Aluto volcanic complex. A detailed investigation of the shallow subsurface using 2D gravity models, volcano-tectonic evidences, surface thermal manifestations, various gravity and magnetic maps has revealed the existence of a potential heat source/magma chamber occurring beneath the Aluto volcanic complex. Quaternary faults of the Wonji Fault Belt are inferred to play a vital role in transporting melt from a deeper intrusion to the magma chamber, in acting as conduits for migration of surface and/or groundwater to the magma chamber and in transporting thermal fluid to the surface (detected as surface thermal manifestations) beneath the Aluto-Langano geothermal system.

***Key words**: Aluto-Langano geothermal field, Geothermal Sources, Gravity anomaly maps, Magnetic anomaly maps, 2D gravity models*

ACKNOWLEDGMENT

I would have never been successful, but God made everything possible. I have no word to express my filling more than “Thanks for his long-lasting love.”

Next to God, I am very much grateful to my advisor Dr. Abera Alemu for his memorable help during my field work, fatherly approach, excellent supervision, encouragement, crucial comments, guidance, reviewing and editing the thesis and providing secondary gravity and magnetic data including all the relevant literatures and information for successfully producing this MSc thesis work.

I would like to thank all of my instructors in the School of Earth Sciences, AAU. The Staff members of the Geophysics stream, particularly Prof. Tilahun Mammo and Prof. Tigistu Haile were very positive and supportive and deserve special acknowledgement.

My special thanks go to Mr. Aklilu Teka, staff member of Reykjavik geothermal company for his incredible support and assistance in processing gravity and magnetic data using Geosoft Oasis Montaj software. His encouragements, constructive comments, endless suggestions and immense knowledge have made me assertive to independently compile different maps using Geosoft Oasis Montaj software, Map Info, Global Mapper and Arc GIS.

I would also like to thank the PhD candidates of the geophysics stream at the School of Earth Sciences, Addis Ababa University particularly, Mr. Muluken Kassa who helped me during my field work and data processing.

My deepest appreciation also goes to my family particularly, my father Demissie Awash and my mother Meskerem Teshoma who have delivered me with proper education, endless supports, encouragements and so much love. My heartfelt thanks go to all my sisters and brothers for their long lasting financial and moral support throughout my academic life.

Last but not least, I would like to express my deepest gratitude to the 2021bach graduate students of the geophysics stream for their discussion and encouragement during this MSc thesis work.

Table of Contents

List of Figures

List of Tables

LIST OF ACRONYMS

AS	**Analytical Signal**
CMER	**Central Main Ethiopian Rift**
EAGLE	**Ethio-Afar Geoscientific Lithospheric Experiment**
EARS	**East African Rift System**
ED	**Euler Deconvolution**
GBL	**Goba-Bonga Lineament**
GPS	**Geographic positioning system**
GSE	**Geological survey of Ethiopia**
HDR	**Horizontal Derivative**
IGRF	**International Geomagnetic Reference Field**
IGSN	**International Gravity Standardization Network**
UGG	**International Union of Geodesists and Geophysicists**
Ka	**Thousand years ago**
Ma	**Million years ago (million)**
MER	**Main Ethiopian Rift**
mGal	**milliGal**
MSL	**Mean Sea Level**
nT	**Nano Tesla**
NE–SW	**North East–South West**
N-E	**North–East**
NMER	**Northern Main Ethiopian Rift**
NNE	**North North East**
NW	**North West**

NW-SE	**North West–South East**
NNE–SSW	**North North East–South South West**
NNW	**North–North–West**
N–S	**North–South**
RTP	**Reduction to Pole**
SE	**South East**
SI	**Structural Index**
SMER	**Southern Main Ethiopian Rift**
SSW	**South South West**
S –W	**South–West**
TDR	**Tilt Derivative**
WFB	**Wonji Fault Belt**
YTVTL	**Yerer Tuluwelel Volcano-tectonic Lineament**
2D	**Two dimensional**

CHAPTER ONE

INTRODUCTION

1.1 General background

Geophysical exploration is the science that deals with measurement of the physical properties of the earth. It is one of the three most important disciplines for surface geothermal exploration. Almost all geophysical methods have been used to assess geothermal systems, the success (or failure) of each method depends on the geological and hydrological setting as well as the type of the geothermal system. Geophysical methods that can be used in geothermal field exploration are divided into two. These are I) the direct geophysical methods (thermal method, electrical resistivity method and self-potential method) which gives detailed information on different parameters that are very much influenced by the geothermal activities and II) the indirect geophysical methods (magnetic method, gravity method and active seismic method) that gives the detailed information about subsurface structures or geological bodies that are very important for the understanding of a geothermal system. In this paper gravity and magnetic methods from indirect geophysical methods are used. In this work the main focus is on parameters (temperature, porosity, permeability and water saturation) that are directly and/or indirectly influenced by geothermal activity. However, these parameters cannot be measured directly through conventional geophysical methods. But temperature, electrical resistivity, thermal conductivity, gravitational field measurement and magnetic field measurement can give us a clue about the above parameters.

The Aluto-Langano geothermal prospect area is located in the Central Main Ethiopian Rift which is part of the East African Rift System. The East African Rift originates from Aden Junction and continues in the direction of SW-SSW traverse longitudinally connecting the eastern African countries including Djibouti, Eritrea, Ethiopia, Kenya, Uganda and Tanzania. Generally, the East African Rift is characterized by the geological occurrence of active faults, active volcanoes and hot springs, which indicates the existence of geothermal source. The Aluto-Langano geothermal field is suited in the young volcanic activity because geysers, fumaroles (also called solfataras), hydrothermal alterations and hot springs which are manifested in the study area are most

commonly found in regions of young volcanic activity. Geophysical surveys over moderately steep terrain can usually be used to assess the lateral extent of a geothermal reservoir. This is because there is a significant contrast in physical parameters between the surrounding rocks and the reservoir rocks which is resulted from fluid rock interactions. The areal extent of geothermal prospects can often be obtained from the study of surface manifestations if fluids affect the ground surface of the geothermal prospect area. However, in most volcanic settings such as the Aluto-Langano geothermal prospect area, hydrothermally altered rocks are hidden by vegetation and/or a weathered layer or covered by younger deposits of tephra and alluvium. Not only this, but also thermally altered ground exhibits physical properties that differ with respect to those of unaltered ground. Therefore, geophysical exploration methods are essential to detect such subsurface geological environments.

In porous and permeable areas surface water percolates downward through the aquifer rock below the Earth's surface to high-temperature regions surrounding a magma reservoir (either active or recently solidified but still hot). Following this, the water is heated, becomes less dense and rises back to the surface along fractures, lineament, fissures and cracks. Sometimes, the above features are called "dying volcanoes" because they seem to represent the last stage of volcanic activity as the magma at depth cools and hardens. Geothermal energy potential is located beneath the Earth’s surface with the most desirable high temperature sources being concentrated in regions of active geologically young volcanoes and igneous intrusions. The replenishment of subsurface magma bodies can drive structurally controlled geothermal systems (Hill et al., 1985; Moore et al., 2008). Fluid migration at high temperature has the potential to provide an abundant renewable energy resource which is called geothermal resource (Hill et al., 1985; Moore et al., 2008). The Aluto-Langano geothermal field is identified as a promising geothermal prospect area for the generation of renewable energy. The gravity and magnetics survey of the study area was conducted in an attempt to delineate the subsurface geological structures and understand their relationship with the geothermal system.

The main objective of conducting the present study is to assess sources of the geothermal potential associated with the Aluto-Langano geothermal prospect area located in the central sector of Main Ethiopian Rift using gravity and magnetic geophysical methods.

The complied gravity and magnetic data were analyzed using integrated gradient interpretation techniques (Horizontal Gradient (HG), Source Edge Detection (SED), Analytic Signal (AS), Tilt Derivative (TDR) and Euler deconvolution (ED) methods). The applied geophysical techniques detected several subsurface faults that were readily compared with the apparent surface faults revealed on the available geological map (Fig. 2.7) of the study area.

1.2 Description of the study area

1.2.1 Location and Accessibility

The Aluto-Langano geothermal field is located in the Central Main Ethiopian Rift about 200 km south of Addis Ababa (Fig. 1.1). The study area is approximately bounded by UTM coordinates 429600m-504600m Easting and 810000m-886250m Northing. The altitude in the study area ranges from 2904m to1567m above mean sea level (m.s.l).

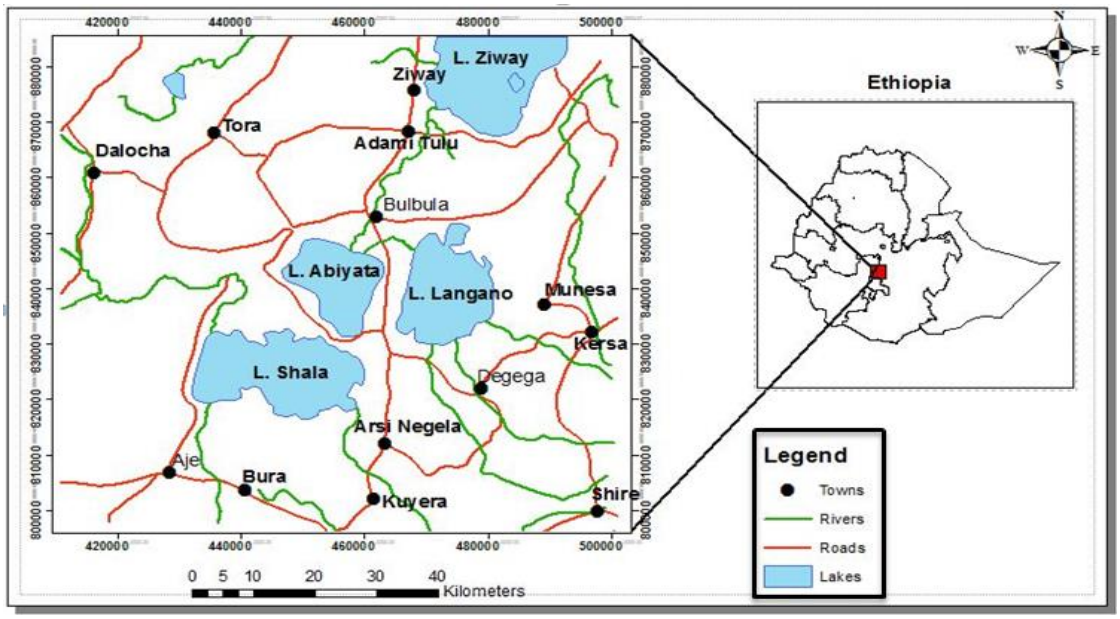

Figure 1.1 Location map of the study area complied using Arc GIS and Geosoft Oasis Montaj

The study area is accessed via two main asphaltic roads running from Addis Ababa via Bishoftu – Mojo – Ziway – Adami Tulu town and via Alemgena - Butajira - Ziway - Adami Tulu town.

1.2.2 Physiography

The Main Ethiopian Rift where the present study lies is part of the East African rift system that extends more than 1000 km in the NE-SW to N-S direction from the Afar depression (Red Sea-

Gulf of Aden junction) to Turkana depression in south. The MER separates the uplifted Somalian and Ethiopian plateau which rise for more than 2000m above mean sea level. The elevation of the rift floor increases from the Turkana depression towards the main watershed lying between the Meki and Awash rivers. Northwards from the Awash-Meki watershed the elevation of rift floor decreases as we go to the Afar depression and reaches to values below mean sea level at the Dallol area. Therefore, the physiography of the rift valley in general and the study area in particular exhibits undulations (ups and downs) due to the occurrence of volcanic centers and well-defined NNE–SSW oriented fault scarps. In the study area the western rift margin is marked by deep gorges and canyons relative to the eastern rift margin (Fig. 1.2). This is because of regional marginal fault system is concentrated in the western rift margin.

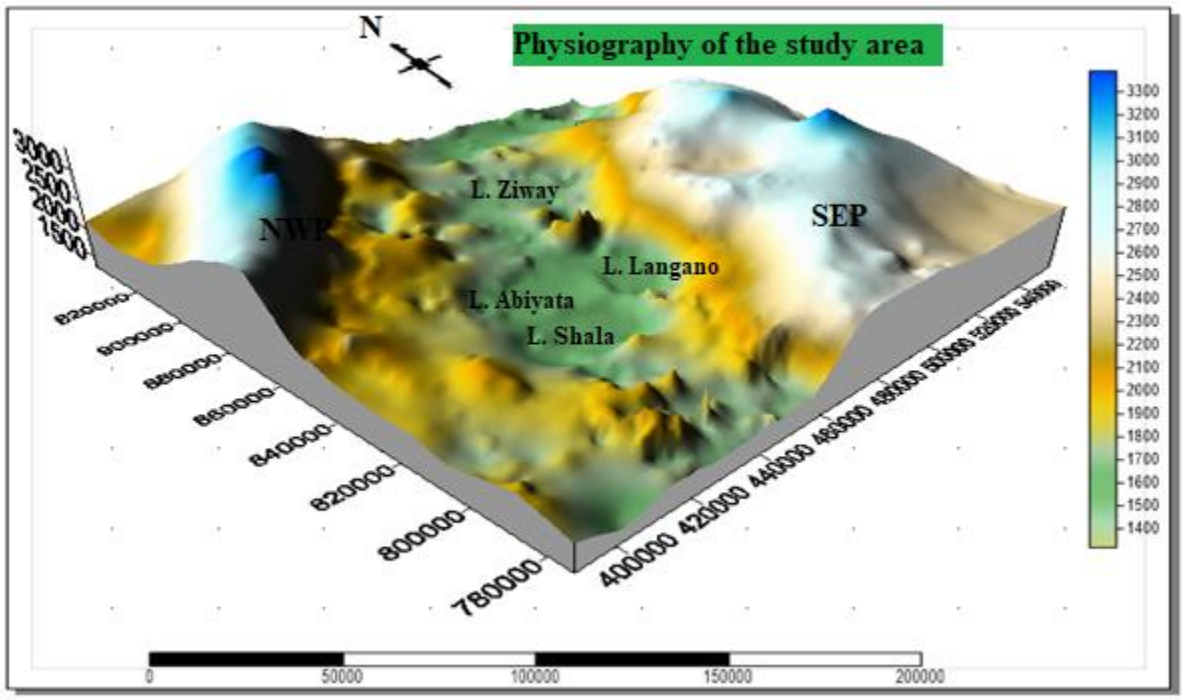

Figure 1.2 physiography of the study area complied using Surfer v10

1.3 Statement of problem

There are a number of investigations that have been done regarding to the geothermal energy resource in the Central Main Ethiopian Rift (Hill et al., 1985; Meseret Teklemariam & Kibret Beyene, 2002; Matthew et al., 2007; Moore et al., 2008; Abebe Tolasa, 2008; Biggs et al., 2011). The deep conditions of the geothermal reservoir using chemical and gas data from deep wells of the Aluto-Langano geothermal field were investigated (Mekuria et al., 1987; Berhanu Gizaw,

1989; Meseret Teklemariam, 1996). The subsurface geology and mineralogy of different wells using various analytical methods (binocular microscope analysis, petrography microscope analysis, X-ray diffractometer analysis and Inductively Coupled Plasma-Optical Emission Spectroscopy (ICP-OES) analysis) have been conducted (Selamawit Worku, 2016). In Aluto Langano geothermal field, eight exploration wells (LA- 1 to LA-8) were drilled in 1981 to 1986 with a maximum depth of 2500m, reaching temperature of up to 335°C (Meseret Teklemariam & Kibret Beyene, 2002).

Therefore, based on results of the above cited research works and that of other researchers the author of this thesis is tempted to assess sources of the geothermal system associated with the Aluto-Langano geothermal field using gravity and magnetic data corroborated by the available geological and structural data.

1.4 Hypothesis/research question

To identify the research problem the following research questions are formulated.

- Why is geothermal potential concentrated in the Aluto volcanic complex?
- How are subsurface structure and geothermal system related to each other?
- Is there any relationship between geothermal system and hydrology of the area?

1.5 Objectives of the research

1.5.1. General objective

The main objective of this work is to assess heat sources of the geothermal potential associated with the Aluto-Langano geothermal field located in the central sector of Main Ethiopian Rift using gravity and magnetic data.

1.5.2. Specific objective

The specific objectives of the thesis are:

- Map the geophysical anomalies that are related to the volcano-tectonic structures occurring beneath the study area.

- Locate geological structures (faults, contacts, etc.) and ascertain physical properties (density and susceptibility) that are related to geothermal sources of the study area.
- Identify the elements (heat source, reservoir and sealing system/cap rocks) of the geothermal systems based on the geophysical signatures they produce.

1.6 Expected outcomes and significance of the study

This thesis work uses gravity and magnetic data to assess geothermal sources within a bounded area. The outcomes of the research work could be used to assess sources of geothermal system in areas which are not well studied. The anticipated outcomes of the research work are:

- ✓ A total magnetic anomaly (TMA) map and its derivative maps
- ✓ A complete Bouguer gravity anomaly (CBA) map and its derivative maps
- ✓ 2D gravity models

The outcomes of the thesis may facilitate the understanding of other geothermal prospect areas identified within the Main Ethiopian Rift, for which the exploration activities have not yet reached the same level of knowledge as that of the Aluto-Langano geothermal field. Moreover, the outcomes of the MSc research could lead to a better understanding of the geothermal system in the study area and could be used as a reference material for future researchers.

1.7 Materials and Methodology

1.7.1 Materials

Up to the end of this thesis work different materials, instruments and software were used. Topographic map, Compass and GPS were used to find the location (Easting, northing and elevation) during magnetic data collection in the magnetic field survey and to analyze the topographical variation of the study area. Earth Magnetometer has been used for Magnetic surveying. All the primary and secondary data were converted to a scientific information using different software's which include Geosoft Oasis Montaj (version 7.0), GYM SYS, Arc GIS (version 10.5), Global mapper, Digital Elevation Model (DEM), CorelDraw (Version 12), Surfer (version 9), Microsoft Office and Google earth.

1.7.2 Methodology

This thesis work utilizes magnetic and gravity methods. The methodology consists of three steps: the desk survey or pre-field work, field work and post field work.

1.7.2.1 Pre-study or desk Survey

The thesis research has been developed based on an extensive desk review of literatures. A theoretical review of the existing literature has been done and secondary data have been used to analyses the existing situation. The sources of the secondary data include published and unpublished papers, MSc. and PhD thesis, journals, books, seminar papers, magazines, bulletins, newspapers and thematic data such as Bouguer anomaly maps, geological maps, topographic maps, geomorphologic maps and hydro geological maps were collected and pre-analysis about the study area were conducted. Secondary gravity and magnetic data were obtained. The aerial photo and topographical map of the study area and all field equipment were collected.

1.7.2.2 Field work

During the field work:

- Magnetic data were collected randomly with an average station spacing of 3-5Km depending on the suitability for the instruments, accessibility, objectives of the study and geological conditions of the area.
- Different geothermal manifestations such as: Fumaroles, hot springs and hydrothermally altered grounds of the study area were identified and/or visited;
- Lithological units of the area were identified and
- Geological structures (fault, joint, fissures and contacts/boundary of different lithological units) of the study area were identified.

1.7.2.3 After field work

- All the primary and secondary row data's were organized, reduced and corrected for use;
- Using Geosoft Oasis Montaj (version 7.0), GYM SYS, Arc GIS (version 10.6), Global mapper, Digital Elevation Model (DEM), CorelDraw (Version 12), Surfer (version 9), Microsoft Office and Google earth different maps and graphs were prepared and

- Based on the collected data and review of the related literatures data interpretations, analysis and conclusions were made.

Flow chart of the methodology followed in this thesis work can be summarized as follows:-

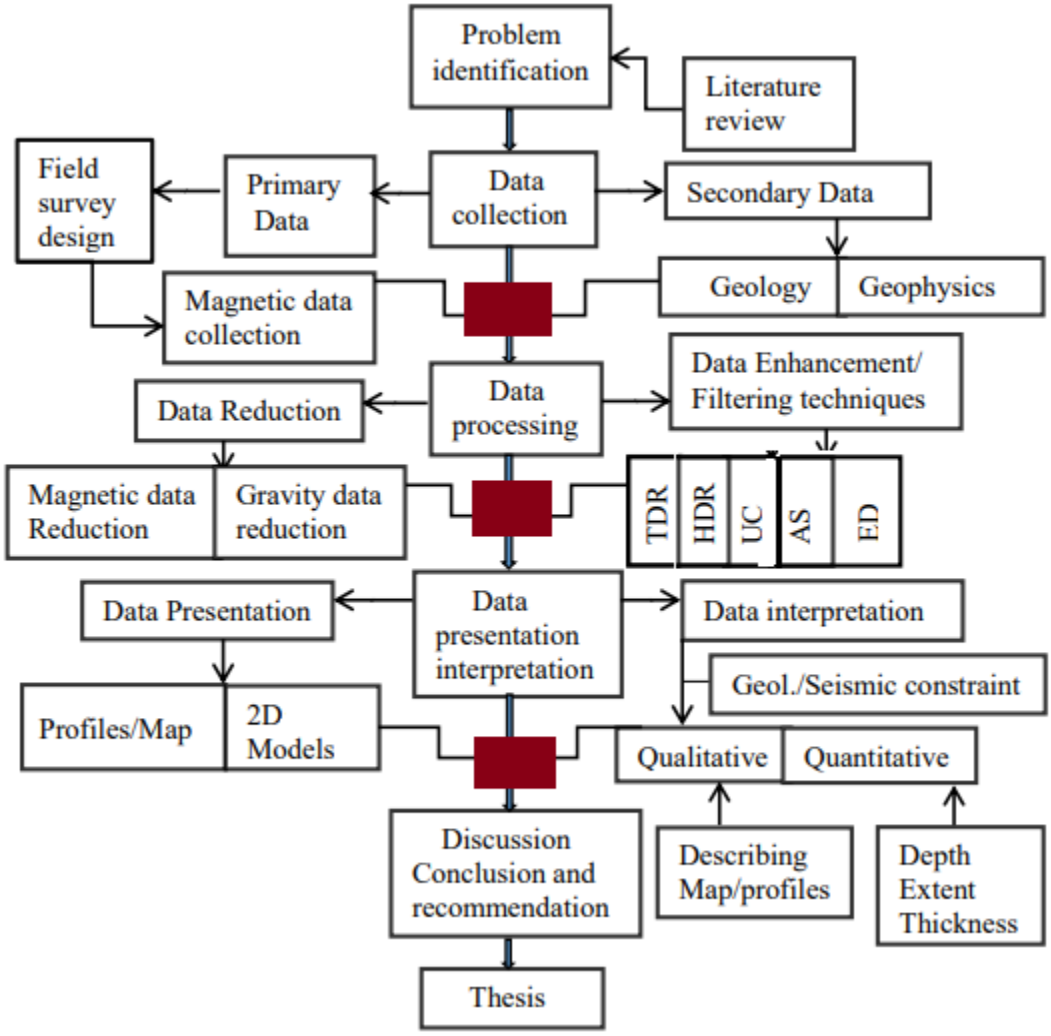

Figure 1.3 Methodological approach and work flow of the study

1.8 Structure of the thesis

This thesis constitutes of eight chapters. The first chapter deals with the introduction and general background by introducing the general frame work of the application of gravity and magnetic methods to map the subsurface structures that control sources of geothermal systems. On the other hand, chapter one includes location and accessibility, physiography of the study area, statement of the problem, research questions formulated to solve the problem, general and

specific objectives of the thesis work, its expected outcomes and contribution to the scientific world and the materials, instruments and software utilized and the methodology adopted to solve the problem. Finally, the overall structure of the thesis work is also included in this chapter. The second chapter deals with the regional geologic and tectonic setting of the East African Rift (EAR), the Main Ethiopian Rift (MER) and the local geologic and tectonic setting of the study area. The third chapter is all about theory of the gravity and magnetic methods adopted in the thesis work. The fourth chapter talks about data acquisition, processing, and presentation. The fifth Chapter deals with the results of the thesis work including analysis and interpretations of the geophysical survey. In addition to this, different data filtering and data enhancement techniques used in the thesis work are briefly discussed. The six chapter talks about 2D forward gravity modeling. The seventh chapter is all about discussion and implication of the results of the thesis work. The last chapter explains conclusions and recommendations based on the thesis work. At the end of this chapter a list of references according to Addis Ababa University /Sinet journal format is presented.

CHAPTER TWO

TECTONIC AND GEOLOGIC SETTING

2.1 Tectonic setting of the East African Rift System

The East African Rift System (EARS) is one of the major tectonic structures of the earth where the heat energy of the interior of the earth escapes to the surface. This energy flow takes the form of volcanic eruptions, earthquakes and the upward transport of heat by hot springs and natural vapor emissions (Ebinger, 2005; Corti, 2009; Corti et al., 2013a). According to Corti (2009), the EARS originated during the Oligocene with the progressive uplifting of East Africa and part of the Arabian Peninsula to form the Afro-Arabian Dome in the Early Tertiary (Upper Eocene) along with tensional tectonic movements. This process caused a continental break-up with intense normal faulting and associated widespread flood basalt eruptions of the Trap Series. The EARS extends for about 6,500km from the Middle East (Dead Sea-Jordan Valley) in the north to Mozambique in the south. The EARS is further divided into the eastern branch and the western branch and consists of several interacting segments (Fig. 2.1). According to Meseret Teklemariam (2013), the EARS passes through Eritrea, Djibouti, Ethiopia, Kenya, Tanzania, Uganda, Rwanda, the Democratic Republic of Congo (DRC), Zambia, Malawi, Mozambique and Madagascar (Fig. 2.1). Moreover, the estimated geothermal energy resource potential associated with the EARS is more than 15,000 MW.

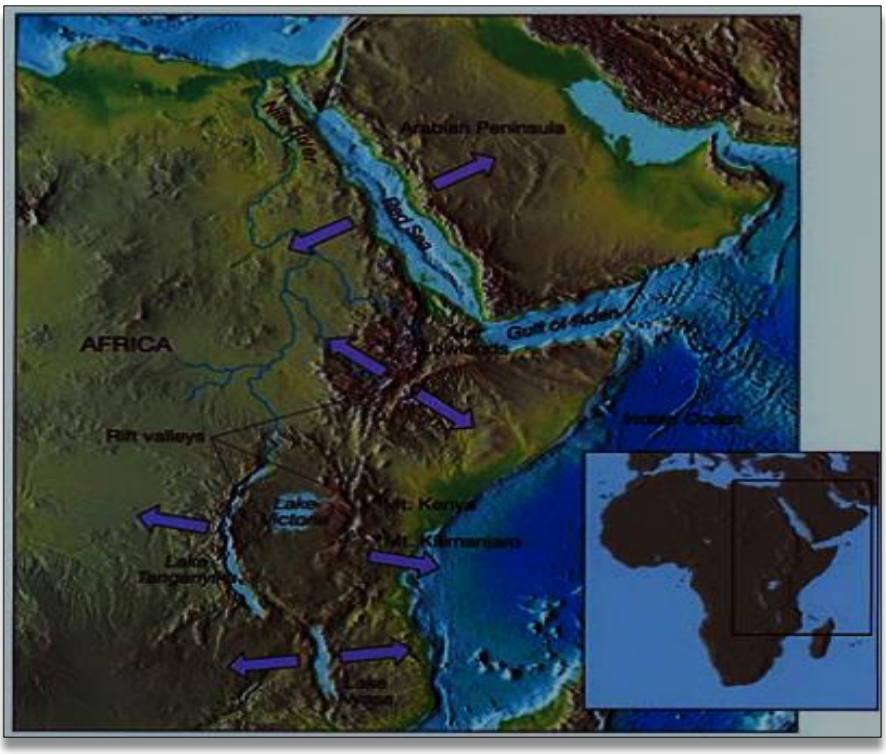

Figure 2.1 Tectonic setting of east African rift system (modified from Meseret Teklemariam, 2006)

2.2 Tectonic setting of the Ethiopian Rift System

The ERS is part of the eastern branch of the EARS and comprises a series of rift zones extending over a distance of about 1000 Km from the Afar Triple Junction (at Red Sea – Gulf of Aden intersection) to the Kenya Rift. According to Boccaletti et al., (1999), the Ethiopian rift system (ERS) consists three segments namely the Afar rift, the Main Ethiopian Rift (MER) and the Southern Ethiopian rift (SER) (Fig. 2.2). The ERS is one of the seismically and volcano-tectonically active places where rift evolution from broadly distributed to focused strain can be followed (Ebinger and Casey, 2001).

2.3 Tectonic setting of the Main Ethiopian Rift System

According to Gidey Woldegebriel et al., (1990), the Ethiopian Plateau (Northwestern Plateau) and the Somalian Plateau (Southeastern Plateau) (Fig. 2.2) is divided by a symmetrical graben with uplifted margins and steep border faults called the Main Ethiopian Rift (MER). The MER is believed to be the result of tensional movements that affected the uplifted Ethio-Somalia plateau

(Di Paola, 1972; Mohr, 1986). The MER is a magmatic rift that recorded all the different stages of the rift evolution from the rift initiation to break up and emerging oceanic spreading (Ebinger, 2005; Corti, 2009).

The MER extends in NE/NNE-SW/SSW direction beginning from the southern Afar rift ($9^0$30'N) to Konso highland ($5^0$15'N) in the southern Ethiopia (Giday et al., 1990). This rift sector consists of three caldera related basins (Ziway-Langano-Abiyata-Shala-Awasa) connected by WFB and Bilate river drainage basins (Giday Woldegebriel et al., 1990). In the MER active faulting and volcanic activity are mostly localized along NNE-SSW trending fault system (Wonji Fault Belt), developed within the rift floor (Kazmin, 1980). Wonji Fault Belt (WFB) is characterized by active extensional fractures and normal faults, which are related to fissural or central volcanic activity.

Geographically, the three sectors of the MER are the Northern Main Ethiopian rift (NMER), the Central Main Ethiopian rift (CMER) and the Southern Main Ethiopian rift (SMER) (Bonini et al., 2005; Gidey Woldegebriel et al., 1990; 1999) (Fig. 2.2). The NMER extends from the MER–Afar Rift boundary southwards to Lake Koka area following the middle course of the Awash River valley, where it is separated from the CMER by the Boru Toru structural highland (Bonini et al., 2005). As indicated by Kazmin et al., (1980); Mohr (1983); Tadiwos Chernet et al., (1998); Wolfenden et al., (2004), early syn-rift volcanism due to the main border faults in the NMER started at about 10-11Ma. The NMER is characterized by two distinct fault sets, namely the NE–SW trending border faults on the margins of the rift and a set of closely spaced NNE–SSW trending faults (Hutchison et al., 2015). Further to the south, the boundary between the CMER and the SMER can be placed at about ~7°N around Lake Awasa area, where the rift margin rotates from NE–SW to N–S (Bonini et al., 2005). The age of the earliest syn-rift volcanic deposits in the CMER sector is estimated to be 6-8Ma (Giday Woldegebriel et al., 1990). The SMER extends south of Lake Awasa towards a 300km wide system of basins and ranges that characterize the overlapping area between the Ethiopian and Kenya Rifts (Bonini et al., 2005 and references therein). Bonini et al., (2005) suggest that in the SMER volcanism started in the early Miocene around 18-21Ma. Width of the MER increases from the SMER (30-60km) to the CMER (65-90km) and the NMER (80-120km) sectors and amounts to more than 200 km wide in the southern Afar Rift. The three sectors of the MER represent different stages of

extensional process, from early rifting in the SMER to more evolute stages in the CMER and NMER preceding the incipient seafloor spreading in Afar (Hayward and Ebinger, 1996).

2.4 Tectonic setting of the Central Main Ethiopian Rift

The Central Main Ethiopian Rift (CMER) consists most of the Lakes region including Lake Ziway, Lake Langano, Lake Abiyata, Lake Shala and Lake Awasa (Fig. 2.2). The border faults encompassed by the CMER are claimed to be formed at about 6-8Ma (Giday Woldegebriel et al., 1990; Bonini et al., 2005) while the Wonji Fault Belts (WFB) occurring along the rift axis are claimed to be initiated at about 2Ma (Corti, 2009). In the CMER, the border faults are still seismically active (Hutchison et al., 2015) and much of the active tectonic deformation occurs along the magmatic segments running through the NNE–SSW oriented WFB (Keir et al., 2006), favoring the occurrence of prominent geothermal reservoir.

The study area is sited in the seismically and tectono-magmatically active part of the CMER which is bounded by the Yerer-Tullu-Wellel volcano-tectonic lineament (YTVL) to the north and the Goba-Bonga tectonic lineament (GBTL) to the south (Fig. 2.2). More specifically, the study area is bounded by the Munesa fault escarpment (a major rift border fault) to the east, the Gurage escarpment (a major rift border fault) to the west of the rift floor, the Lake Ziway to the north and the Lake Shala to the south.

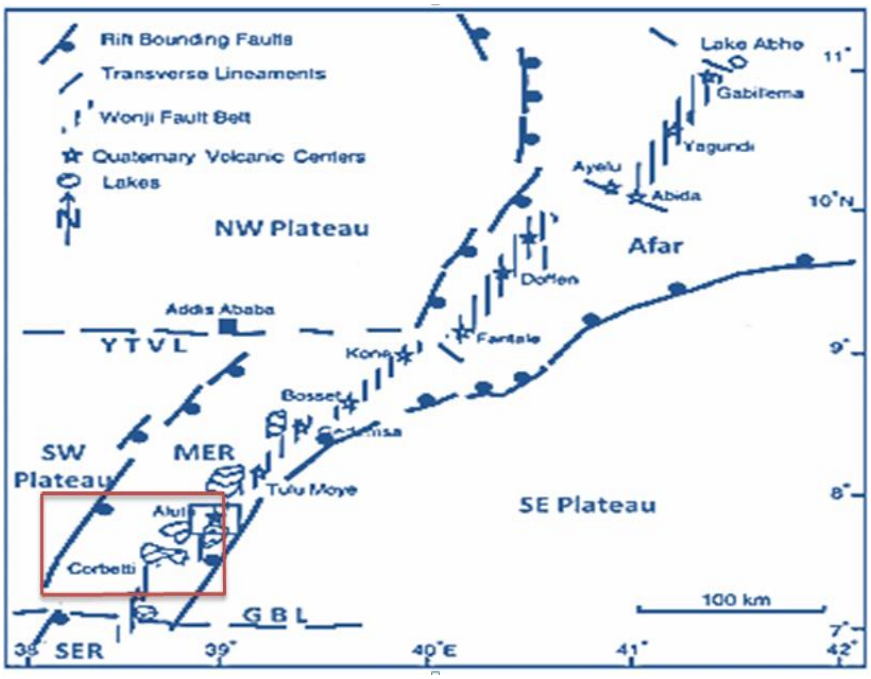

Figure 2.2 Regional structural configurations of the Main Ethiopian and Southern Afar Rifts**.** MER = Main Ethiopian Rift, SER = Southern Ethiopian Rift, GBL = Goba-Bonga Lineament, YTVL = Yerer-Tullu-Wellel volcano tectonic Lineament, the red rectangle is the study area (modified from Giday Woldegebriel et al., 1990)

2.5 Tectonic setting of the study area

According to Selamawit Worku (2016), the Aluto Volcanic Complex is affected by the Wonji Fault Belt (WFB), which is trending NNE-SSW. The Aluto-Langano geothermal field encompasses several faults, complex sets of intersecting structural lineations, discontinuities and open fissures trending in NNE-SSW, NW-SE, N-S, NE-SW and E-W directions (Fig. 2.3). The eastern part of the Aluto-Langano geothermal field is intersected by NE trending structural alignments, whereas, the western part is dominated by NNE trending fracture lines (Fig. 2.3). Most of the recent volcanoes and craters in the study area are aligned along the NNE-SSW trending and some extents are trending to E-W direction (Teklu, 2004). In addition to this, faults that strike in a NNE-SSW direction and dipping towards the west are observed west of the deep exploratory wells LA-3 and LA-6, consistent with the orientation of the WFB (Selamawit Worku, 2016). According to Selamawit Worku (2016), a fault that is located between the deep exploratory wells LA-4 and LA-5 having a NNE-SSW strike and dipping towards west has

caused a total loss of circulation during drilling indicating existence of hydraulic gradient which favours fluid migration beneath the Aluto-Langano geothermal field. It is determined that fluid migration is an essential component for an effective utilization of a geothermal potential.

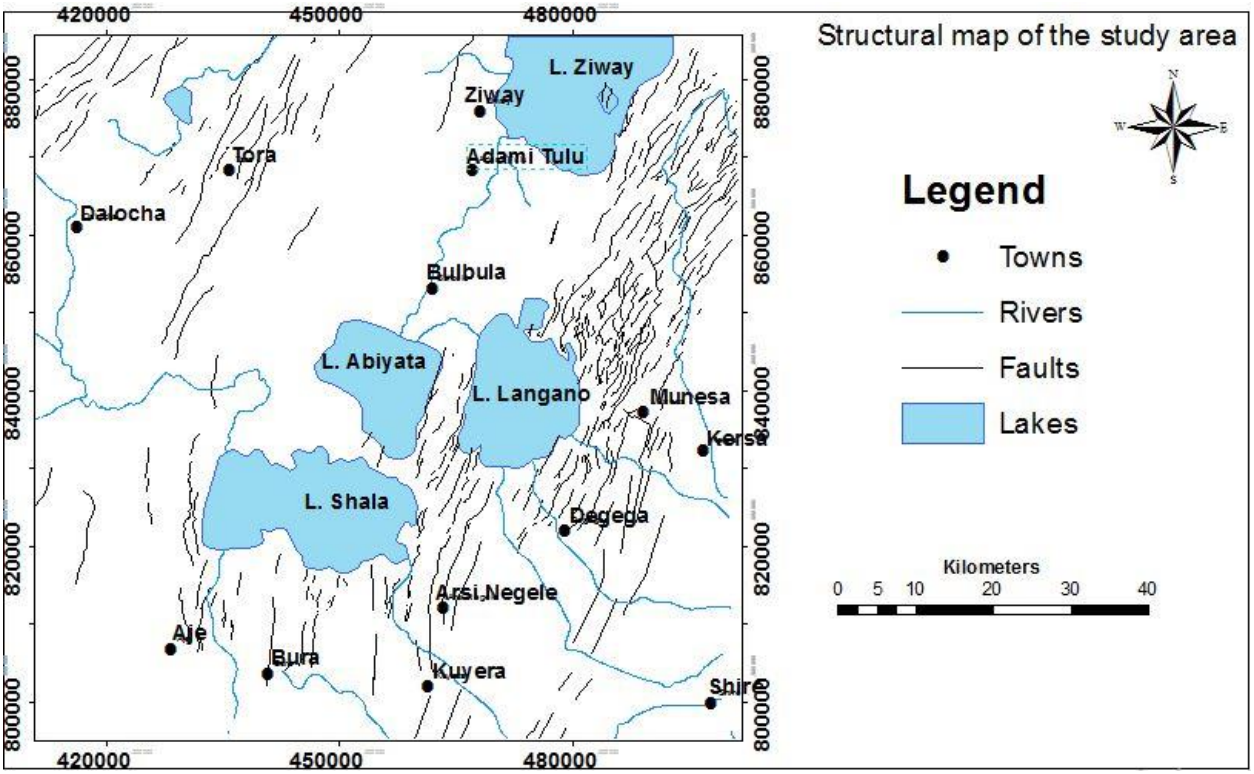

Figure 2.3 Structural map of the study area

2.6 Geology of the Ethiopian Rift System

According to Corti (2009), pre-rift geology of Ethiopia is composed by an extremely folded and foliated basement rock. Mainly those rocks are exposed in the SMER, western rift escarpment of the CMER and the northern Afar (Fig. 2.4). These rocks are overlain by Mesozoic sediments. Volcanisms in Ethiopia were started during the Eocene-Late Oligocene with the eruption of the Ethiopia–Yemen flood-basalt province (Trap series) (Mohr and Zanettin, 1988). Mohr and Zanettin (1988); Kieffer et al., (2004) suggests that the composition of this volcanic episode varies from tholeiitic to alkaline lava flows and felsic lavas with pyroclastic rocks of rhyolitic and trachytic compositions interbedded with the flood basalts. The first eruption of flood basalts was mostly occurred through fissures at places controlled by pre-existing weak zone (Mohr and Zanettin, 1988; Mege and Tesfaye Korme, 2004). Most of the basalts and associated felsic rocks

were apparently erupted in a rather short time interval (~5Ma) with the extreme eruption rates occurring from 31-28Ma (Baker et al., 1996; Hoffman et al., 1997). The second eruption is Miocene in age and is characterized by the construction of huge basaltic shield volcanoes like Termaber Megazez Formation. A large number of shield volcanoes developed from 30Ma to about 10Ma on the surface of the volcanic plateau immediately after the peak of volcanic activity (Kieffer et al., 2004). This subsequent, less voluminous volcanic activity formed some of the highest reliefs of the plateau (e.g. Mts. Simien and Choke) (Mohr and Zanettin, 1988; Kieffer et al., 2004). The third stage, Pliocene-Quaternary in age, is directly related to the main phases of opening of the main Ethiopian rift and Afar rift (Wolfenden et al., 2004). Volcanism in the MER is dominated by per-alkaline rhyolitic ignimbrites, pumice and ash-fall deposits with minor lava flows. Silicic rocks are associated with volumetrically subordinate basaltic products that form cinder cones and lava flows mostly aligned along the WFB (Mohr, 1971) (Fig. 2.3). Most recent acidic products in the NMER have been erupted from central volcanoes with large summit caldera. Fissural eruptions of silicic rocks have been inferred, but rarely demonstrated by field studies for the lowest exposed silicic rocks forming the rift-floor ignimbrites (Di Paola, 1972; Boccaletti et al., 1999). In terms of geology, the floor of the rift valley is predominantly covered by volcanic rocks such as rhyolite, trachyte, pyroclastic fall, ignimbrite and basalt (Giday Woldegebriel et al., 1990). According to Giday Woldegebriel et al., (1990), the central sector of the MER in which the study area is sited can be classified into six chronostratigraphic units (Table 2.1).

Table 2.1 Stratigraphy of the CMER (after Giday Woldegebriel et al., 1990)

Absolute age			Central MER Lithology
Era	Age		
Cenozoic	Quaternary 1.6		Quaternary sediment Wonji Group
	Pliocene (5.3)		Chillalo trachyte
			Butajira ignimbrite
	Miocene	upper 11.2	----------
			Guraghe basalt
		Middle 16.6	

			Shebele trachyte
		Late 23.7	
			---------- ----------
	Oligocene	Upper 30	
			Kella Basalt
		Lower 36.6	
			---------- ----------
	Eocene		
Mesozoic	Jurassic	Upper	Variegated shale
		middle	
			Antalo limestone
		lower	Adigrat sandstone
Pre-Cambrian			Crystalline basement

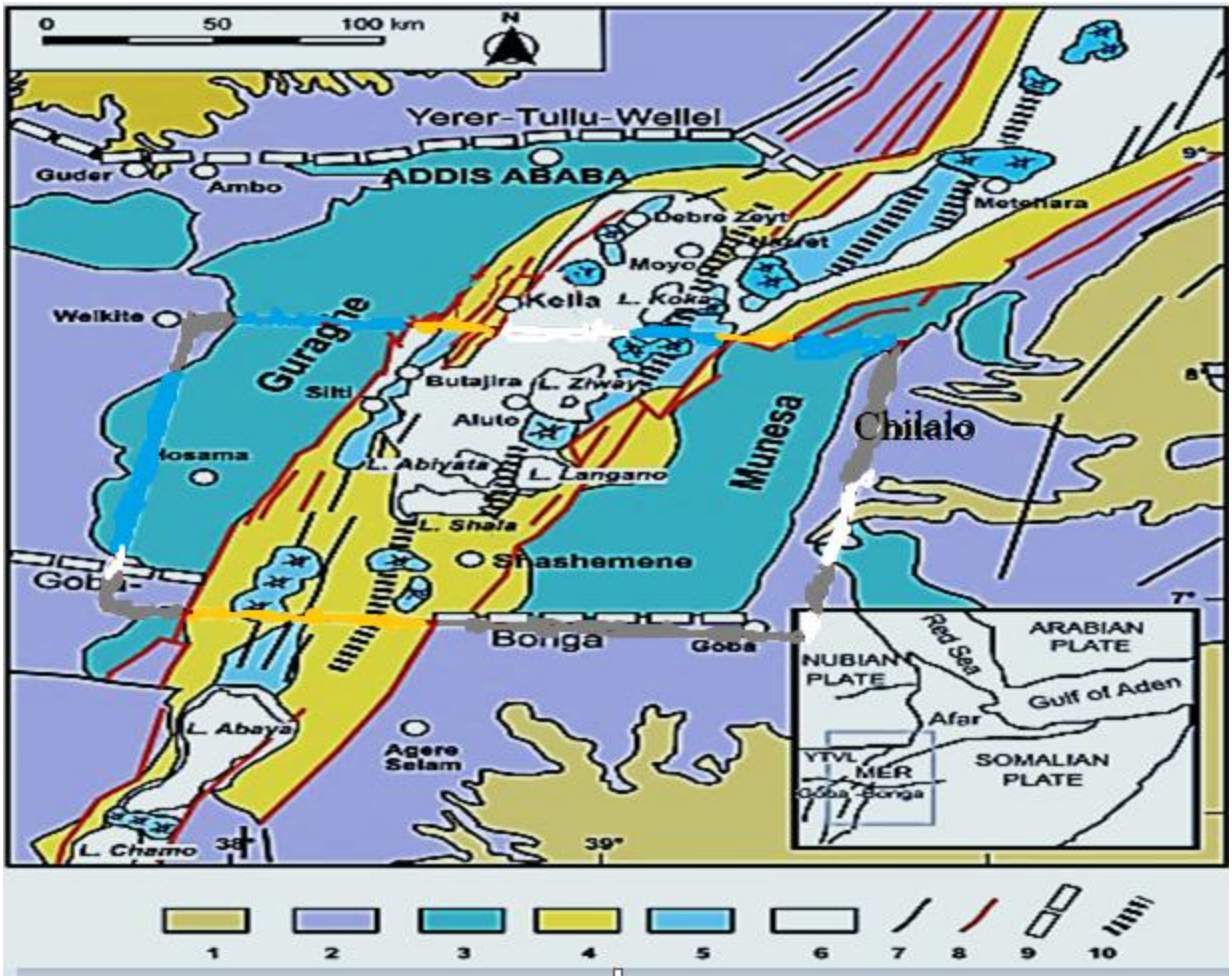

Figure 2.4 Simplified geological map of central Ethiopia (modified from Tsegaye Abebe et al., 2010).

(1) Pre-Tertiary sediments and crystalline basement, (2) Oligocene (32-29Ma) and lower Miocene (12-8Ma) plateau volcanics, (3) Miocene–Pliocene rift-shoulder trachytic–rhyolitic volcanics and pyroclastic layers, (4) Plio-Pleistocene rift floor, (5) Quaternary central volcanics and basaltic lava flows, associated scoria cones and phreato-magmatic deposits, (6) Quaternary lacustrine sediments and inter-bedded pyroclastics, (7) faults, (8) major rift border faults, (9) major transversal tectonic lineaments in the basement, (10) Wonji Fault Belt segments. In the inset: YTVL, Yerer-Tullu-Wellel volcano-tectonic lineament and GBTL, Goba-Bonga tectonic lineament.

2.7 Regional geology of the Main Ethiopian Rift

During the early stages of the MER, several central volcanoes erupted and formed very thick pyroclastic deposits, thought to have been partially produced from fissures. These volcanic products have ages of about 5Ma and are known as the Nazreth group (Kazmin and Berhe, 1978; Tadiwos Chernet et al., 1998; Boccaletti et al., 1999; Giday Woldegebriel et al., 1999; Abebe et al., 2005). Meyer et al., (1975) identified two volcano-tectonic units in the northern part of the MER which include the Nazreth series and the Wonji series. The Nazreth series extends from the Turkana rift in Kenya through the MER axis to the South Afar and the South Eastern Escarpment (Baker, Mohr and Williams, 1972). The composition of the Nazreth series is dominated by silicic rocks such as Ignimbrites, Rhyolites and Pumice. The age of this unit is about 5.2 Ma and with a thickness of not more than 150 m. This series is overlain by Lacustrine and fluvial sediments. The younger unit (Wonji series) is of Pleistocene to Holocene age and lies with an unconformity of the Nazreth series. According to Meyer et al., (1975); Mohr (1971), the Wonji series is mainly composed of basaltic flows with some silicic and intermediate rocks. The silicic and intermediate rocks (also known as the Wonji group), generally located near the Wonji fault belt (Kazmin and Berhe, 1978) include all the rift volcanics formed after the major episode of rift faulting following the accumulation of the Bofa basalt, Pantelleritic volcanic centers represents eruptions of Perkaline rhyolites, Trachytes, pumice and obsidian. The rocks belonging to the Wonji series are generally aligned in "en echelon" arrangements along all segments of the Wonji fault belt. Meyer, et al., (1975) further classifies the Wonji series into two parts as the lower part and the upper part. The lower part is characterized by the Welenchiti basalt with an unconformity and a thick layer of loam situated between the two.

According to Mohr (1971), the deepest lithological unit of the crust in the central part of MER is little known. However, the general succession of strata in the horn of Africa consists of metamorphic, Mesozoic sedimentary sequence, Tertiary flood basalts and silicic lava flows with pyroclastic sediments interstratified overlain by Quaternary sediments and alkali silicic lava flows. These sequences and one of the aged rocks, the crystalline basement/Precambrian rocks dominantly outcrop being associated with margins of CMER and tops of the Gurage Mountain ranges (Giday Woldegebriel et al., 1999).

The MER in which the study area is embedded is developed beginning from the Oligocene to the Quaternary. Major volcanic episodes are recognized in the Oligocene, middle Miocene, late Miocene, early-middle Pleistocene and Holocene (Giday WoldeGabriel et al., 1990). According to Giday WoldeGabriel et al., (1990), the oldest volcanic formations exposed in and around the rift margins (e.g. Blue Nile gorge) are basaltic and rhyolitic flows in the Oligocene. By the middle Miocene, some parts of the CMER were dominated by containment basaltic flows. In the Pliocene, a huge pyroclastic flow covered the eastern and western part of study area. This characteristic pyroclastic flow deposits are currently identified to occur at a depth of around 2100m by geothermal wells sunk in the rift floor (Giday Woldegebriel et al., 1990; 2000). In the Pleistocene, the Wonji Fault Belt (WFB) was formed in the rift floor with basaltic and rhyolitic flows exposed along its axis. The Aluto Volcanic Complex (AVC), being formed during Late Pleistocene to Holocene period, is governed by the nature of the WFB, though the NW-SE and ENE-WSW oriented transversal structures also played an important role. Volcanic products of the AVC cover an area of about 120 km^2 forming a rhombic area elongated in a NW-SE direction. Sediments of Lacustrine origin surrounding the AVC are well represented and cover a large area of the rift floor with large thicknesses at places. These rift sediments are the only non-volcanic formations in the CMER with considerable thicknesses ranging from about 400m along the Bulbula River, 500m along the Boru and Meki rivers and to more than 1000m between the Mojo and Koka localities.

Tenalem Ayenew (1998) compiled a general stratigraphic map of the MER (Fig. 2.5), with a chronological order ranging from the older to the younger. These formations include the Nazret group and Dino formation undifferentiated, the Afar group, Chilalo volcanics, Balchi rhyolite, basalts and associated flows of the rift, central rift volcanic complexes (Aluto volcanics, Gedemotta rhyolite, Corbetti volcano, Bora-Bericho and Fike) and volcano-sedimentary rocks and lacustrine sediments (Fig. 2.5).

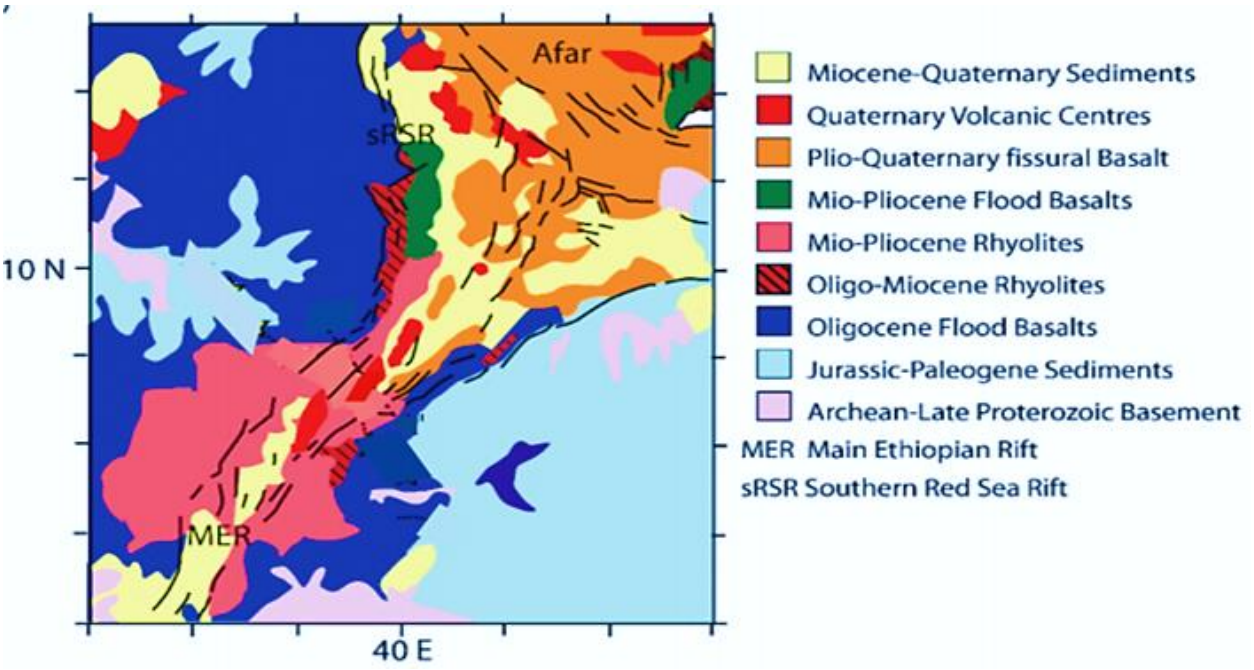

Figure 2.5 Simplified geological map of the MER and Afar region (after Wolfenden, 2003)

2.8 Geological setting of the study area

Geology of the study area (Fig. 2.7) which consists of the Aluto-Langano geothermal field and its environs is summarized as follows. The Aluto volcanic complex which lies in the center of the study area is an active volcanic system within the CMER (Selamawit Worku, 2016). According to Electroconsult (1986), the caldera rocks of the post-syn are dated at about 55 ka and those of the old rocks are dated at about 150ka. The caldera collapse most probably occurred between 50 to 80ka. The outcropping rocks in the study area which consists of the Aluto-Langano geothermal field are mainly volcanic complexes and Quaternary lacustrine sediments (Fig. 2.7). The volcanic activity of the AVC started around 150ka with an explosive eruption of ignimbrite (Electroconsult, 2015) and build-up of rhyolitic flow domes being interrupted by explosive pyroclastic pumice eruptions and major caldera forming pyroclastic eruption (Ernst & Nihon, 2010). Following post-caldera collapse, rhyolitic flow domes with minor pyroclastic products occurring along the NE-SW segment of the Aluto caldera rim were overlaid by pumiceous ignimbrites and older rhyolite. The rhyolite flow domes were followed by strong uplift of E-W oriented faults. Following the uplifting phase, volcanic activity continued with the emplacement of several rhyolitic domes. Rhyolitic post-caldera lavas and pyroclastics erupted from several craters appear to be controlled by either a caldera ring fracture or NNE-SSW

trending faults of the WFB. Minor basaltic lava flows occur along the NNE-SSW trending border faults observed east of the Aluto massive. The Aluto caldera is covered by alluvial sediments. According to Ernst & Nihon (2010), the most recent volcanic products beneath the Aluto volcanic complex include a series of obsidian lava flows which are mainly concentrated on the southern, eastern and western parts of the caldera.

The general lithological units of the Aluto-Langano geothermal field and its environs, designated from the older to the younger are summarized in the following sections.

2.8.1 Nazreth series

The name Nazreth series is given to a thick succession of ignimbrites with fiamme, pumice, ash, rhyolitic flows and domes with rare intercalations of basaltic flows (Meyer et al., 1978). The Nazreth series are mapped on the southeastern part of the geologic map (Fig. 2.7) compiled for the study area. In the outcrops of this rock unit vertical and sub-horizontal aligned joints are visible. They are slightly weathered owing to their composition, texture and color. The Nazreth series are composed of sub-alkaline rhyolites and trachyte with rare peralkaline varieties (Morbedelli et al., 1973). The texture of ignimbrite is porphyritic. The Nazerth series are the oldest rock unit in the study area and have ages ranging from 9Ma to 3Ma owing to their relation to the Miocene-Pliocene lacustrine sediments of the Chorora formation and some absolute K/Ar age determinations (Tiercelin et al., 1980; Kazmin and Berhe, 1978).

Based on their degree of weathering and composition the Nazerth series tend to have moderate density and low magnetic susceptibility values as compared to the Quaternary basalts that reside in the study area. Thicknesses of the ignimbrite unit are about 200m to 250m beneath the rift floor and tend to thin out on the escarpments of the study area. Moreover, on the plateau margins a thickness of about 1m to 30m was reported at several localities.

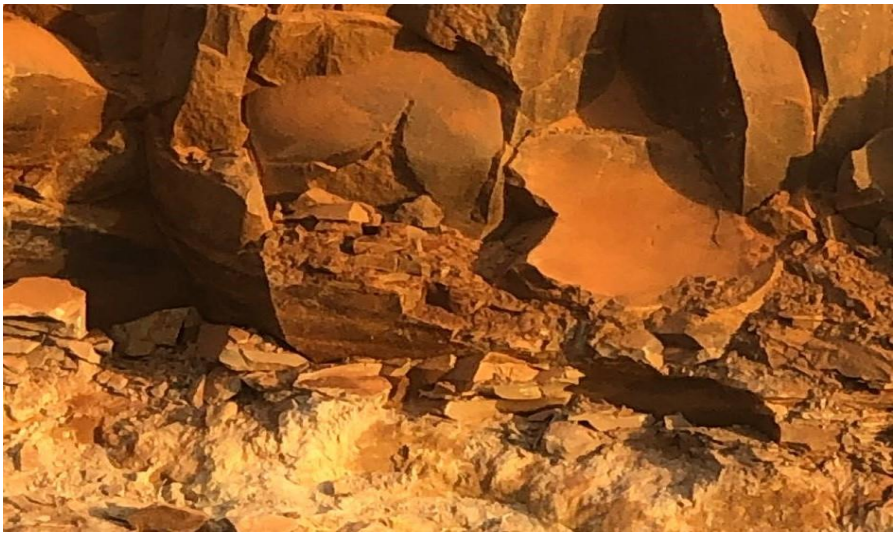

Figure 2.6 Ignimbrite units residing the study area (photo taken during field work)

2.8.2 Chilalo formation (Nc and Ncb)

According to Kazmin and Berhe (1981), a group of Early Pliocene shield volcanic complexes which developed on both sides of the rift floor caldera and margins of the MER are named as the Chilalo formation. Trachytic lava flows (alkaline basalt) and pyroclastic deposits that compose the Chilalo formation (Nc and Ncb) are mapped in the southeastern part of the study area (Fig.2.7). These formations have a general texture of porphyritic with feldspar and biotite as phenocrysts and hornblende and augite as groundmass. Two volcanic units constitute this formation which include the lower (Nc) and the upper (Ncb) as distinguished by Kazmin and Berhe (1981). The lower unit (Nc) comprises intercalation of peralkaline ignimbrites and trachyte which show clear flow structures. The dominant rock type corresponding to the lower unit is strongly porphyritic dark grey trachyte with sanidine phenocrysts. The upper unit (Ncb) which commonly forms the top part of the shield volcanoes is invariably represented by fresh flows of porphyritic alkaline basalts.

Owing to their composition (chemical composition and mineralogical content) the Chilalo formation could be considered to have high density and susceptibility values as compared to the Nazerth series (ignimbrites with fiamme, pumice, ash, rhyolitic flows and domes).

2.8.3 Dino formation (Qd)

Green and gray ignimbrites (with well-developed fiamme) and unwelded pyroclastics with occasional intercalated lacustrine beds and aphyric basalts are named as the Dino formation (Kazmin and Berhe, 1978; 1980). These rock units are mapped in the eastern, western and southern parts of the study area and enclose the Quaternary sediments mapped in the center of the study area (Fig. 2.7). These rock units form geological structures which include NNE-SSW and NE-SW trending faults mapped in the study area (Fig. 2.3). Next to the Quaternary lacustrine sediments the dominant rock units in the study area include the Dino formation (Fig. 2.7). The Dino formation comprises felsic lava of peralkaline composition. Pyroclastics of the Dino Formation could be thought to have sources from the axial centers (rhyolitic volcanic center (Qr)) of the rift floor.

The rocks (ignimbrite and unwelded pyroclastics) that compose the Dino formation could be thought to have low density and susceptibility values as compared to the Nazerth series (ignimbrites with fiamme, pumice, ash, rhyolitic flows and domes) and Quaternary basalts mapped in the study area (Fig. 2.7).

2.8.4 Rhyolitic volcanic complexes (Qr)

The rhyolitic volcanic complexes (Qr) encompass products of volcanic centers composed of trachyte to peralkaline rhyolites (pantellerites and commendites). The rhyolitic volcanic complexes are mapped in the study area, particularly north and west of Lake Langano and south of Lake Shala (Fig. 2.7). The most recent stages of volcanic activity related to the rhyolitic volcanic complexes are marked by obsidian flows, pumice, ignimbrite, tuffs and scoriaceous basalt. The Quaternary central volcanic complexes which are situated along the axial zones of the MER mainly along the WFB and Afar have produced peralkaline lavas and pyroclastics (Morbeddelli et al., 1975).

The rock units (obsidian flows, pumice, ignimbrite, tuffs and scoriaceous basalt) comprised by the Quaternary central volcanic complexes are considered to have low density and susceptibility values similar to those of the Dino formation.

2.8.5 Quaternary basalt (Qb)

Generally, it is determined that Quaternary basalts are olivine rich basalts occasionally showing a trend towards picritic types. The Quaternary basalts dominantly occur south of Lake Shala and western part of the study area (Fig. 2.7). The chemical compositions of these rock units are intermediate between alkali basalts and tholeiites. The mineralogical compositions of these rocks are alkali basalts. Two stages of development are distinguishable in several places; the first is a fissural stage with eruptions of basalts of transitional composition and the second stage was the central type eruption of basalts of tholeiitic composition which produced the differentiates of basalts through intermediate iron-rich varieties (ferro-basalts, hawaiites, mugearites and dark quartz rich trachytes) to a very limited amounts of alkaline and peralkaline silicic (Qbt) (Varet, 1978).

The rock units (ferro-basalts, hawaiites, mugearites and dark quartz rich trachytes) comprised by the Quaternary basalts are considered to have high density and susceptibility values as compared to other lithological units of the study area.

2.8.6 Quaternary sediments

Quaternary sediments of different origin (fluvial, lacustrine, Aeolian, eluvial and marine) are widely spread all over Ethiopia. In the CMER which consists of the study area, the Quaternary sediments are mostly of lacustrine, Alluvial and Colluvial origin. Lacustrine beds are interbedded with Pliocene-Pleistocene pyroclastics in the Lakes region and on the rift shoulder (Mohr, 1966; Lloyd, 1980). The lacustrine beds are mostly redeposited volcanic sands, tuff with calcareous materials and diatomite. The thickness of these sediments of undifferentiated continental origin (gravel, sand, silt and clay) reaches 10 to 20 meters in the rift floor at places and tend to increase towards the plateau escarpments (Kazmin, 1972). Quaternary sediments of lacustrine and alluvial-colluvial origin mapped in the central part of the study area (Fig. 2.7) are the most dominant lithological units. The alluvial-colluvial sediments are found in areas of higher elevation as compared to the lacustrine sediments.

In general the Quaternary sediments that reside in the study area could be associated with low density and susceptibility values as compared to the Quaternary basalts that occur in the south of Lake Shala and western part of the study area (Fig. 2.7).

2.8.6.1 Pleistocene Lacustrine deposits (Qpl)

These Lacustrine sediments occupy a very wide area and are found intercalated with the pumiceous pyroclastics and/or ash deposits of the AVC. Generally these deposits vary from sandy gravel to fine silt and clay size being very rich in diatomite. Hence, they are thought to be candidates of rock units favoured in geothermal exploration due to their high permeability and porosity to act as reservoirs and cap rock in sandy and clay enviroments, respectively. According to Le Turdu et al., (1999), Lake Abiyata and Lake Langano which occur between Lakes Ziway and Shalla were formed in relation to the collapse of the Gedemota caldera. This event could be very important for the modification of the rift floor lake basins. According to Giday Woldegebriel et al., (1999), formation of the Gurage escarpment on the western margin and the Munesa escarpment on the eastern margin at about 3.5Ma significantly modified the rift structure with pronounced subsidence. This event is thought to correspond to the initial formation of the rift lakes.

2.8.6.2 Alluvial and Colluvial Deposits (Al)

These units have a wide range of origin and composition consisting of mainly soil that overlie ignimbrite and basaltic lava flows and developed due to weathering and erosion of the substratum rock. The alluvial deposits occurring over rivers and old river beds and colluvial deposits occurring over slope screep and rock falls (particularly under big fault scarps) are transported by water and gravity.

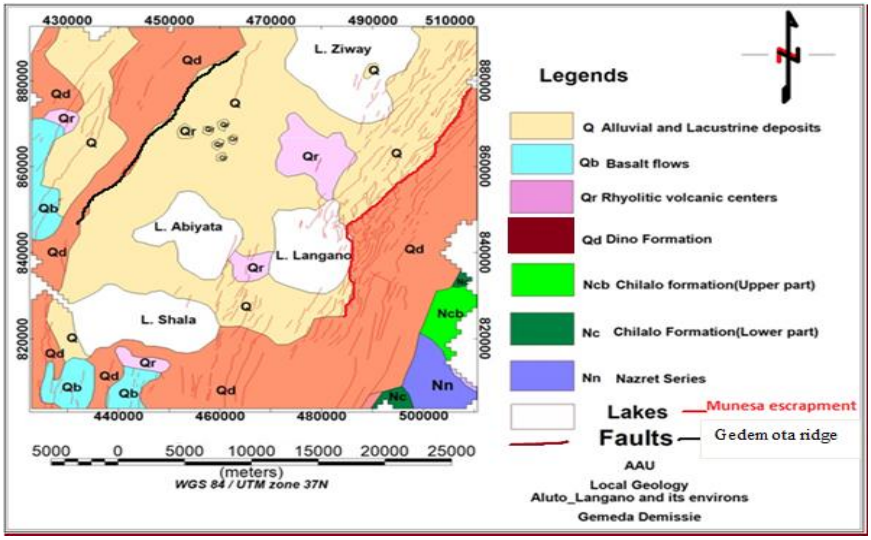

Figure 2.7 simplified geological map of the study area

CHAPTER THREE

THEORETICAL FOUNDATIONS OF GRAVITY AND MAGNETIC METHODS

3.1 Introduction

Geophysical exploration is the science that deals with measurement of the physical properties of the earth. Different geophysical methods study the variation in physical properties of the subsurface material. Generally, these geophysical methods can be divided into two. These are: the passive geophysical methods and the active geophysical methods. The passive geophysical method uses natural sources. This includes gravity, SP, and magnetic method. Whereas the active geophysical methods uses artificially generated sources. These are electrical methods, seismic methods and etc.

Geophysical exploration is one of the three most important disciplines for surface geothermal exploration. In this work the main focus is on parameters (temperature, porosity, permeability, salinity and water saturation) that are directly and/or indirectly influenced by geothermal activity. These parameters cannot be measured directly through conventional geophysical methods. But temperature, electrical resistivity, thermal conductivity, gravitational field measurement and magnetic field measurement can give us a clue about the above parameters. Geophysical methods that can be used in geothermal field exploration are divided into two. These are I) the direct geophysical methods (thermal methods, electric resistivity methods and self-potential methods) which gives detailed information on different parameters that are very much influenced by the geothermal activities and II) the indirect geophysical methods (magnetic method, gravity method and active seismic method) that gives the detailed information about subsurface structures or geological bodies that are very important for the understanding of a geothermal system. In this work gravity and magnetic method from indirect geophysical method are used. A review of different scientific papers clearly shows that there is considerable geothermal energy resource in the rift system. The replenishment of subsurface magma bodies can drive structurally controlled geothermal systems. Fluid migration at high temperature has the

potential to provide an abundant renewable energy resource which is called geothermal resource (Hill et al., 1985, Moore et al., 2008). Geophysical methods have contributed invaluably through remotely sensing the nature and structure of the lithosphere (Hinze et al., 2013). Gravity and magnetic methods continue to have an important role as there are notable variations in density and magnetization properties of the crust and upper mantle that make up the lithosphere. This is particularly true in the crystalline portion of the lithosphere where structural deformation and intrusive events are more likely to result in near-vertical contacts, produces much more identifiable gravity and magnetic anomalies. Magnetometer and gravimeter are often referred to as structural methods. They have much in common, complement each other and supply more information about the subsurface than either technique on its own (Reynolds, 1997). In geophysics, the gravity method exploits the earth's gravity field difference caused by lateral density variations. It plays two fundamentally useful roles in the earth sciences: 1) inexpensively detect "anomalies" worth studying. 2) Falsifies and eliminates models by forward computations. The method is also used in modeling the earth's crust and it is the basis for the study of the earth's shape (Telford et al., 1990). Geomagnetic methods can provide a wide variety of applications and range from small to large-scale regional geological mapping to determine gross structure (e.g., concealed igneous dyke intrusion, fault zones) (Reynolds, 1997). The field varies inversely one power faster with distance than does the gravity field; it is more sensitive to the source depth which is an important objective in interpretation of the observations. Despite its high resolving power (Hinze et al., 2013), it is much more complex due to dipolar nature and time based variation of the magnetic field (Telford et al., 1990).

3.2 Gravity method

3.2.1 Introduction

Gravity method is a non-destructive geophysical method that measures differences in the earth's gravitational field at specific locations. The gravity method is a relatively cheap, non-invasive, non-destructive remote sensing method. It is a method that studies subsurface geology on the basis of variations in the Earth's gravitational field that arise from differences of densities between subsurface rocks. The most important idea to be kept in mind is that the concept of a causative body, which is a rock unit of different density from its surroundings. A causative body

represents a subsurface zone of anomalous mass and causes a localized perturbation in the gravitational field known as a gravity anomaly. Interpretation of gravity anomalies allows an assessment to be made of the probable depth and shape of the causative body.

3.2.2 Basic theory

The basis of the gravity survey method is universal Law of gravitation and Newton's second law of motion. Newton's universal law of gravitation states that the force of attraction **F** between two masses $\mathbf{m_1}$ and $\mathbf{m_2}$, whose dimensions are small with respect to the distance **r** between them, is given by equation 3.1 and Newton's second law of motion states that the force is directly proportional to the acceleration and mass of the object which is given by equation 3.2.

$$F = G\frac{m_1 m_2}{r^2} \ldots\ldots\ldots 3.1$$

$$F = m_2 g \ldots\ldots\ldots\ldots 3.2$$

Where, F = Force of attraction between the two objects (N);

G = $6.67*10^{-11}$ $m^3kg^{-1}s^{-2}$ is the Universal Gravitational Constant;

m_1m_2 is Product of the masses of the two objects in kg;

r is Distance between the two masses and

g is gravitational acceleration or gravity.

Let us, consider the Earth is spherical in shape, homogeneous and non-rotating of mass **M** and radius **R** so that the mass of the sphere is concentrated at the center of the sphere and gravitational attraction of a small mass **m** on its surface can simply be calculated us follows (eq.3.3). And also, according to newton's second law of motion force is proportional to acceleration. Therefore,

$$F = G\frac{m_1 m_2}{r^2} = m_2 g \ldots\ldots\ldots\ldots 3.3$$

Where, **g** is gravitational acceleration or simply, gravity (ms^{-2})

Thus, from equation 3.3 $g = \frac{GM}{R^2}$ ……..*3.4*

Where, g is the gravitational acceleration or, simply, **gravity**.

Equation 3.4 shows that the magnitude of acceleration due to gravity on Earth (**g**) is directly proportional to the mass (**M**) of the Earth and inversely proportional to the square of the Earth's radius (**R**). During gravity surveying, our interest is to measure the gravitational acceleration which is the time rate of change of a body's speed under the influence of the gravitational force.

The **weight** of the mass is given by **mg**. On such an Earth, gravity would be constant. However, since the Earth is ellipsoidal in shape, rotated, irregular surface relief and internal mass distribution the gravitational acceleration or gravity will vary over its surface. Therefore the gravitational field is most usefully defined in terms of the gravitational potential **U (eq.3.4).** The gravitational acceleration **g** is a vector quantity, having magnitude and direction (vertically downwards) whereas the gravitational potential **U** is a scalar quantity, having magnitude only. The first derivative of **U** in any direction gives the component of gravity in that direction. Consequently, a potential field approach provides computational flexibility. Equipotential surfaces can be defined on which **U** is constant. The sea-level surface or geoid is the most easily recognized equipotential surface, which is everywhere horizontal, that is, at right angles to the direction of gravity.

$$\mathbf{U} = \frac{GM}{r} \quad \ldots\ldots\ldots\ldots 3.5$$

3.2.3 Units of gravity

The mean value of gravity at the Earth's surface is about **9.8ms^{-2}**. The variations in gravity which is caused by density variations in the subsurface materials are of the order of **100µms^{-2}**. This unit which is micrometer per Second Square is referred to as the gravity unit (**gu**). In ground gravity surveys an accuracy of **±0.1gu** is readily attainable, corresponding to about one hundred millionth of the normal gravitational field whereas in ship borne gravity survey the accuracy obtainable is considerably less, about **±10gu**. The c.g.s. unit of gravity is the milligal (1mgal = 10^{-3} gal = 10^{-3}cms^{-2} = 10^{-5}ms^{-2}), equivalent to **10gu**. The density of the rocks depends mainly on the rock composition and its porosity, but partial saturation of the rocks may also influence the values. Normally the density is between ~2-3g/cm^3. Generally, sedimentary rocks are lighter than crystalline rocks (basement rock).

3.2.4 Theoretical gravity

The determination of a standard formula for the theoretical value of gravity at any point of the ellipsoid was done in 1930 when the International Union of Geodesy and Geophysics adopted the International Gravity Formula (Reynolds, 1997) whose general form is given by:

$$g_\phi = g_0(1 + \alpha sin^2\phi - \beta sin^4\phi) \ldots\ldots\ldots 3.6$$

Where, g_ϕ = gravitational acceleration at latitude ϕ;

g_0 = gravity at the equator and

α, β = are constants dependent on the shape and speed of rotation of the Earth.

In 1967, the increasing computational capabilities of computers, as well as better value for earth parameters given by satellite measurements allowed scientists to refine the parameters of equation 3.6 to define the new standard. The International Gravity Formula (IUGG, 1967), presented here allows the determination of the theoretical value of **g** on the ellipsoid at a given latitude (ϕ): $g_\phi = 978031.846(1 + 0.005278895\sin^2\phi - 0.000023462 sin^4\phi)$. Therefore we also used this equation for the determination of the theoretical value of **g**.

3.2.5 Gravity field and figure of the Earth

For a small mass, moving with a velocity, on the surface of the earth rotating with angular velocity as shown in the figure 3.1a, different forces are acting on it and it is possible to develop the theoretical gravity or the normal gravity value of the earth. To develop the theoretical gravity or normal gravity value of the earth let us consider the earth to be a smooth ellipsoid. To start with, assuming the earth to be a spheroid (Heiskanen and Moritz, 1967) and that a body of mass m is moving with a velocity of **v** on the surface of the earth (M = mass of the earth, R = radius of the earth), the possible forces acting on the body are:

1. The mass attraction force g_m (eq.3.7)

   $$g_m = \frac{GM}{R^2} \ldots\ldots\ldots 3.7$$

2. The radial component of the centrifugal force per unit mass which is caused due to the rotation of the earth with angular velocity ώ about its axis of rotatiobn (eq.3.8)

$g_{ώ} = ώ(ώ \ x \ R)……3.8$

from the above equation we can conculed that the maximum force is at the equator and zero at the poles and it opposes the attractive force of the earth.

3. The Coriolis force per unit mass acting on m_2 due to the motion of the mass with linear velocity v on the earth's surface can be given by

   $C = 2(ώ \ x \ v)……..3.9$

   from this equation we can say something. That is if the mass is at rest on the surface of the earth V = 0 and therefore C = 0

4. The tidal force per unit mass acting on m due to mass attraction with other heavenly bodies (T). Therefore, the net gravitational field or gravity is given by

   $g = g_m + g_{ώ} + C + T……..3.10$

   Where, g_m - attraction force per unit mass acting on due to earth's mass;

   $g_{ώ}$ - Centrifugal force per unit mass acting on due to earth's rotation with;

   T - Tidal force per unit mass acting on due to mass attraction of heavenly bodies and

   C - Coriolis force acting on due to its motion and its value is zero if it is at rest.

Since heavenly bodies constantly change their arrangements with respect to the position of the earth the number of the heavenly bodies and their magnitude of gravitational attraction vary from time to time and it is not simple to put it in a simple formula. It is not constant, but rather vary with the position of the heavenly bodies that impose garvitational force on our earth. Gravity survey shouldn't be administered during the time of significant tide; otherwise, for small magnitude of tide the effect of T on g is generally considered negligible. However, the Earth is not a perfect spheriod. At the pole it is flattened and deviates by about 14.2 km and at the equator it is bulged by about 7.1 km from the normal spheroid of constant radius of 6356.751 km. if 'a' is the equatorial radius of the earth and 'b' is the polar radius of the earth. The polar flattening f is defined as: $f = \frac{a-b}{a}$……...3.11

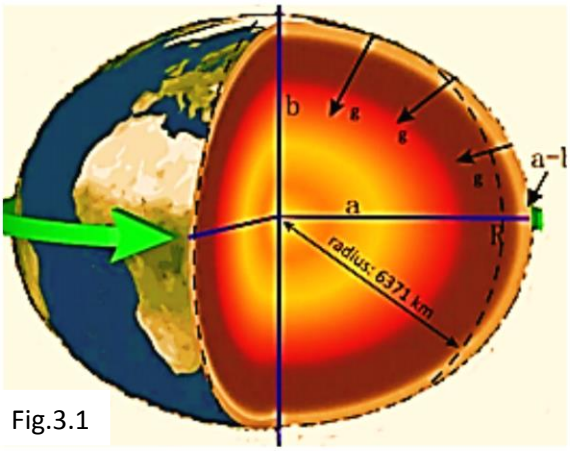

Fig.3.1

Figure 3.1 the gravity figure of the earth**.** Where, a-b is

the difference in equatorial and polar radius respectively. g: gravity and Fc=centrifugal force (after pierrick, 2015).

As can be seen in figure 3.1 the radius of the earth at the equator is greater than the radius at the pole by **a-b**. This shows that the earth is bulged outward at the equator due to its rotation and flattened at the pole. This figure also verifies equation (3.4) which shows gravity is higher at the pole and lowers at the equator since gravity is inverse proportional to square of the radius.

The flattening of the optimum reference ellipsoid of the earth was revised many times. The long worked supposition defined in 1930 was exactly f = 1/297. With the use of satellites and highly sensitive gravimeters, in 1980 the value was revised as f = 1/298.257 (Lowrie, 1997).

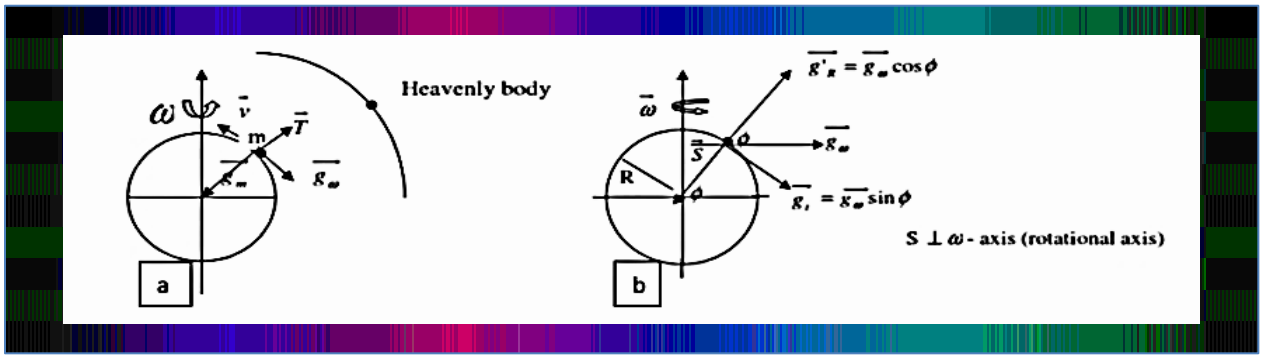

Figure 3.2 (a) Gravity force per unit mass acting on a mass, m on earth and (b) components of forces acting on mass, m on earth's surface (after Reynolds, 1997)

3.2.6 The geoids and the reference ellipsoid

Geodesist or geophysicists consider two surfaces that represent the average shape of rotationally distorted earth to study its gravity field, geoid and reference ellipsoid (Fig. 3.3). In geodetic and geophysical measurements reference surfaces (topography, geoid and ellipsoid) play key roles in theoretical calculations and physical measurements. The reference spheroid: A mathematically generated theoretical earth model, flattened at the poles and bulged at the equator, neglecting undulations on the earth's surface where as we have hills, mountains and depressions on the real earth. The flattening (f) of the earth is given by: $f = \frac{a-b}{a}$ = 1/298.257 (eq. 3.11) The theoretical value of gravity g_ϕ adopted by the International Union of Geophysics and Geodesy (IUGG) in 1930 and revised by the Geodetic Reference System in 1967 is given by:

$g_\phi = g_e(1 + B_1 sin^2{}_\phi + B_2 sin^2 2_\phi)$ (3.12) Where, g_e = 978031.846, B_1 = 0.005278895, B_2 = −0.0000059, and $\phi\ is\ th\ e$ latitude. The reference geoid, physical equipotential surface referred to mean sea level, forms a reference surface for measurements of acceleration due to gravity. Hence to account continental elevation and ocean depression, it is necessary to define the geoid, as the average sea level over the oceans and over the surface of sea water (Telford et al., 1990). Geoid warped upward under continents because of attracting material above and downward over the ocean basins due to the low density of water (Fig. 3.3).

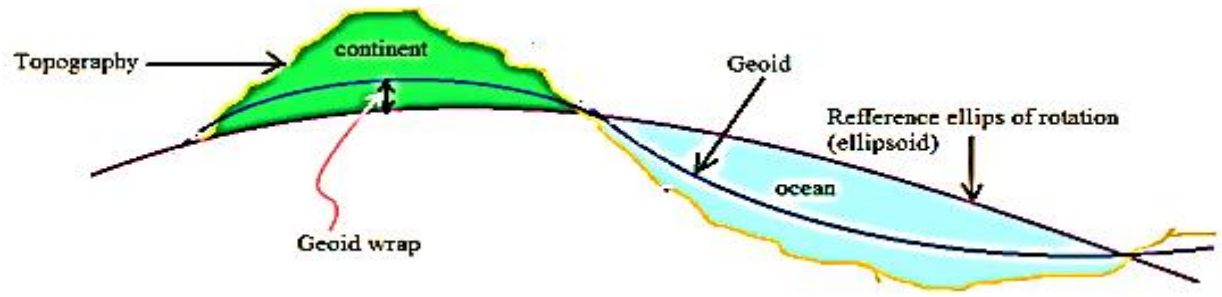

Figure 3.3 geophysical reference surfaces geoid, topography and ellipsoid (after Reynolds, 1997)

3.2.7 Gravity data reduction

Dentith and Mudge (2014) suggest that for most geophysical methods, it is necessary to apply a variety of corrections to the raw data obtained in the field. This means before the results of a gravity survey can be interpreted it is necessary to correct for all variations in the Earth's gravitational field which do not result from the differences of density of the subsurface medium. This process is known as gravity reduction (LaFehr, 1991) or reduction to the geoid, as sea-level is usually the most convenient datum level. So, reduction is a term which refers to the conversion of raw gravity data to a usable form.

3.2.7.1 Drift correction

According to Reynolds (1997) the basis for instrumental drift correction is change (drift) in gravimeter reading with time as a result of elastic creep in the springs. This change produces an apparent change in gravitational acceleration at a specific location. The base station is revised most commonly at every 1-2 hours (Reynolds, 1997). Correction for instrumental drift is based on repeated readings at a base station at recorded times throughout the day (Kearey et al., 2002).

After drift correction the difference in gravity between an observation point and the base station is found by multiplication of the difference in gravimeter reading by the calibration factor of the gravimeter. Knowing this difference in gravity, the absolute gravity at the observation point g_{obs} can be computed from the known value of gravity at the base station. The differences between successive measurements at the same station are plotted against time and drift to produce a drift curve which is assumed to be linear between consecutive base readings (Kearey et al., 2002) and the observed gravity values from intervening stations can be corrected by subtracting the amount of drift from the observed value (Reynolds, 1997).

3.2.7.2 Tidal Correction

According to Kearey et al., (2002), gravity measured at a fixed location varies with time because of periodic variation in the gravitational effects of the Sun and Moon associated with their orbital motions, and correction must be made for this variation in a high precision survey. In spite of its much smaller mass, the gravitational attraction of the Moon is larger than that of the Sun because of its proximity. Also, these gravitational effects cause the shape of the solid Earth to vary in much the same way that the celestial attractions cause tides in the sea. These solid Earth tides are considerably smaller than oceanic tides and lag farther behind the lunar motion. They cause the elevation of an observation point to be altered by a few centimeters and thus vary its distance from the center of mass of the Earth. The periodic gravity variations caused by the combined effects of Sun and Moon are known as tidal variations. They have maximum amplitude of some 3gu and a minimum period of about 12h. If a gravimeter with a relatively high drift rate is used, base ties are made at an interval much smaller than the minimum Earth tide period and the tidal variations are automatically removed during the drift correction. If a meter with a low drift rate is employed, base ties are normally made only at the start and end of the day so that the tidal variation has undergone a full cycle. In such a case, a separate tidal correction may need to be made. The tidal effects are predictable and can be computed by a small computer program (Kearey et al., 2002).

3.2.7.3 Latitude Correction

Gravity varies with latitude because of the non-spherical shape of the Earth and because the angular velocity of a point on the Earth's surface decreases from a maximum at the equator to zero at the poles as shown in figure 3.11(a) (Kearey et al., 2002). The centripetal acceleration

generated by this rotation has a negative radial component that consequently causes gravity to decrease from pole to equator. The true shape of the Earth is an oblate spheroid or polar flattened ellipsoid (Figure 3.11(b)) whose difference in equatorial and polar radii is some 21km. Consequently, points near the equator are farther from the center of mass of the Earth than those near the poles, causing gravity to increase from the equator to the poles. The amplitude of this effect is reduced by the differing subsurface mass distributions resulting from the equatorial bulge, the mass underlying equatorial regions being greater than that underlying polar region.

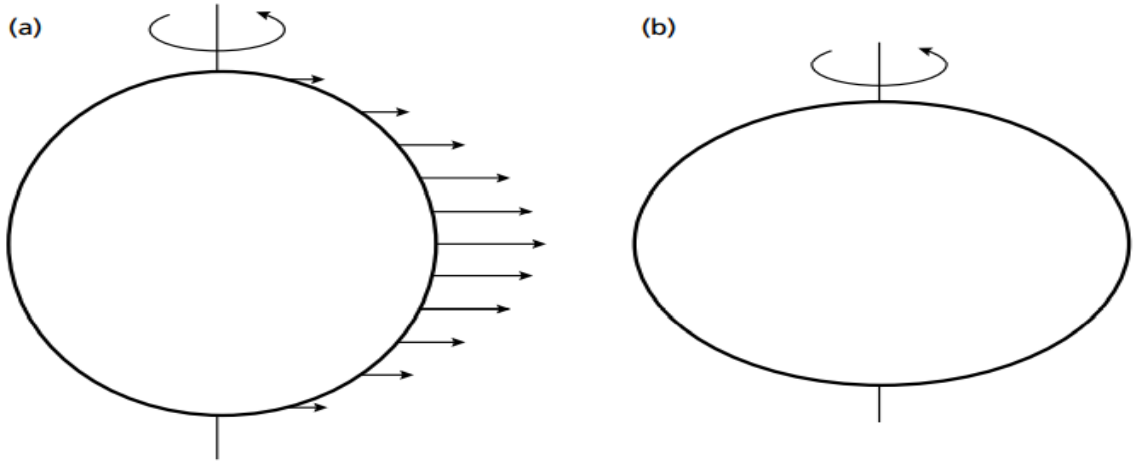

Figure (3.4) (a) the variation in angular velocity with latitude around the earth represented by vectors whose length are proportional to angular velocity. (b) An exaggerated representation of the shape of the Earth.

The true shape of this oblate ellipsoid of revolution results in a difference in equatorial and polar radii of some 21 km adopted from Kearey et al., (2002).

The net effect of these various factors is that gravity at the poles exceeds gravity at the equator by some 51860gu, with the north–south gravity gradient at latitude ϕ being $8.12\sin 2\phi$ gukm^{-1}.

Clairaut's formula relates gravity to latitude on the reference spheroid according to an equation of the form

$g_\phi = g_0(1 + \alpha\sin^2\phi - \beta\sin^2 2\phi)$……..3.11

$g_\phi = 978031.846(1 + 0.005278895\sin^2\phi - 0.000023462 sin^4\phi)$……3.12

Where, $g_\phi$is the predicted value of gravity at latitude φ;

g_0 is the value of gravity at the equator and

α and β are constants dependent on the shape and speed of rotation of the Earth. Equation (3.11) is, in fact, an approximation of an infinite series. The values of g_0, α and β in current use define the International Gravity Formula 1967 (where, g_0 = 9780318gu, α = 0.0053024, β = 0.0000059; IAG 1971). Prior to 1967 less accurate constants were employed in the International Gravity Formula (1930). Results deduced using the earlier formula must be modified before incorporation into survey data reduced using the Gravity Formula 1967 by using the relationship $g_\varphi(1967) - g_\varphi(1930) = (136\sin^2\varphi - 172)$gu. An alternative, more accurate, representation of the Gravity Formula 1967 (Mittermayer, 1969), in which the constants are adjusted so as to minimize errors resulting from the truncation of the series, is

$g_\phi = 978031.846(1 + 0.005278895\sin^2\phi - 0.000023462 sin^4\phi)$ gu……3.13

This form, however, is less suitable if the survey results are to incorporate pre-1967 data made compatible with the Gravity Formula 1967 using the above relationship. The value g_φ gives the predicted value of gravity at sea-level at any point on the Earth's surface and is subtracted from the observed gravity to correct for latitude variation.

3.2.7.4 Elevation corrections

Correction for the differing elevations of gravity stations is made in three parts:

- Free air Correction
- Bouger Correction
- Terrain Correction

3.2.7.5 The free-air correction

Since, gravity is inversely proportional to the square of the distance from the center of the earth it is necessary to correct for changes in elevation between stations to reduce field readings to a datum surface (Telford et al., 1990). The free-air correction accounts solely for variation in the distance of the observation point from the center of the Earth; no account is taken of the gravitational effect of the rock present between the observation point and datum. Free air

correction corrects for the decrease in gravity with height in free air resulting from increased distance from the center of the Earth, according to Newton's Law. The FAC is positive for an observation point above datum to correct for the decrease in gravity with elevation. The change in gravity (dg) with increasing distance from the center of the earth (d_R) is given by the first derivative of "g" with respect to "R" (Lillie, 1999):

$$g = \frac{GM}{R^2}$$

$$\frac{dg}{dR} = -2\frac{GM}{R^3} = -2\frac{GM}{R^2} \cdot \frac{1}{R} = -\frac{2g}{R}$$

By assuming the average value of: g = 9806.25 gu and R = 6367.00 m

FAC = 3. 086h gu (h in meters)……..3.14

The above equation (3.14) illustrates that for approximately every 3m upward from the surface of the Earth, the acceleration due to gravity decreases by about 1mGal (Lillie,1999).

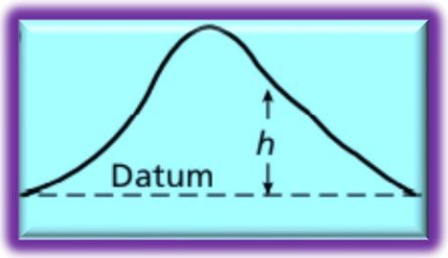

Figure 3.5 the free-air correction for an observation at a height h above datum (Kearey et al., 2002)

3.2.7.6 Bouguer correction

Lillie (1999) suggests that even after elevation correction is made, gravity reading varies from station to station due to differences in mass between the observation point and the sea level datum. The Bouguer correction of sea surface observations is positive to account for the lack of rock between surface and sea bed. The correction is equivalent to the replacement of the water layer by material of a specified rock density **ρr**. On land the Bouguer correction must be subtracted, as the gravitational attraction of the rock between observation point and datum must be removed from the observed gravity value. The Bouguer correction of sea surface observations

is positive to account for the lack of rock between surface and sea bed. The correction is equivalent to the replacement of the water layer by material of a specified rock density $\boldsymbol{\rho_r}$. The free-air and Bouguer corrections are often applied together as the combined elevation correction. The Bouguer correction makes the assumption that the topography around the gravity station is flat. Consequently, the Bouguer correction has overcorrected for these areas and their effect must be

$BC = 2\pi\rho_r Gh$.....3.15

Where, BC= Bouguer Correction

ρ_r= Density of the Slab

G= Universal gravitational Constant

h = Thickness of the slab

But, $\pi = 3.14$, $G = 6.67 \times 10^{-11} m^3 kg^{-1} s^{-2}$

Therefore, $BC = 0.0419\rho_r h$. If we assume the average value of the crustal density as $2.67 gcm^{-3}$,

$BC = 0.112(\frac{mGal}{m})h$……..3.16

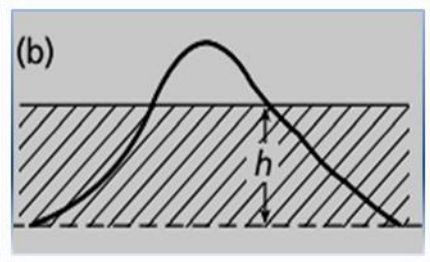

Figure 3.6 the Bouguer correction. The shaded region corresponds to a slab of rock of thickness **h** extending to infinity in both horizontal directions (after Kearey et al., 2002).

3.2.7.7 Terrain corrections

A correction applied to observed values obtained in geophysical surveys in order to remove the effect of variations in the observations due to the topography near observation sites.

The Bouguer correction assumes that the rock occupying the height interval between the datum level and the station is a uniform slab extending to infinity in all directions (Dentith and Mudge, 2014). In other words, the land surface is assumed to be represented by a subdued topography (i.e. the terrain around the observation point is perfectly flat). In reality, there exist "hills" (mountains) rising above the observation point and "valleys" below the observation point (figure 3.7). According to Telford et al., (1990), the terrain correction is thus, to allow for surface irregularities in the vicinity of the observation point. Hills above the elevation of the gravitation station exert an upward pull on the gravimeter, whereas valleys (lack of material) below it fail to pull down ward on it. Thus, both types of topographic undulations affect gravity measurements in the same sense as a result of which, the terrain correction is usually added to the observed gravity reading (e.g. Dobrin, 1988; Telford et al., 1990; Reynolds, 1997).

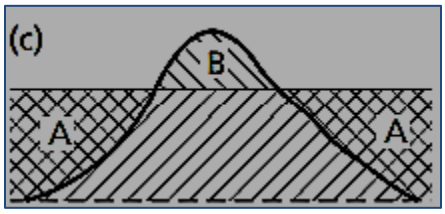

Figure 3.7 the terrain correction

3.2.8 Gravity Anomalies

A causative body represents a subsurface zone of anomalous mass and causes a localized perturbation in the gravitational field. In exploration geophysics, gravity measurements g (g_{obs}) are compared to a modeled value of g (g_{mod}). The differences between these values are called the gravity anomaly (Δg). After an appropriate row gravity data reduction, the final step of any gravity survey is to determine the gravity anomalies. A discrepancy between the corrected, measured gravity and the theoretical gravity is called a gravity anomaly (Lowrie, 2007). This anomaly can therefore be positive or negative, as it is related to a model and not to an absolute measurement of the gravity intensity:

$$\Delta g = g_{obs} - g_{mod} \quad \ldots\ldots\ldots\ldots\ldots\ldots\ldots\ldots 3.17$$

Gravity anomaly map yield the difference between the observed gravity values and the theoretical gravity values for a region of interest. A very wide range of geological situation give rises to zones of anomalous mass that produce significant gravity anomaly.

Depending on what we want to emphasize there are three gravity anomalies:

- Free-air or Faye anomaly
- Bouguer anomaly and
- Isostatic gravity anomaly

3.2.8.1 Free-air anomaly

Here only the effect of elevation of a station from the geoid is considered. In free-air anomaly the attraction of materials between the elevation and the geoid will not be taken into account and that is why it is called the free-air.

The free-air gravity anomaly (ΔgF_A) takes into account the latitudinal change in gravity on the Earth's best fitting ellipsoid represented by the theoretical gravity (g_ϕ) and the vertical change in gravity between the reference datum and the observation height assuming that the gravity station is located in free air, hence the name free air anomaly (Hinze et al., 2013). The equation for Free-Air anomaly (FAA) is given by:

$$\Delta gF_A = g_{obs} - g_\phi + FAC \quad \text{.....3.18}$$

Where, ΔgF_A is free-air gravity anomaly, g_{obs} is observed gravity, g_ϕ is theoretical gravity and FAC is free-air correction

From the equation 3.18 we can conclude that: Subtracting the theoretical gravity from the observed gravity corrects for the latitude, thus accounting for the flatten and bulge of the Earth and adding the "FAC" puts back the gravity lost to elevation, there by correcting the increased radius "R" from the Earth's center.

The FAA is nothing but squashing up all the mass above sea level into an infinitesimally thin layer at sea level, and measuring gravity there.

3.2.8.2 Bouguer anomaly

The Bouguer gravity anomaly, like the free air gravity anomaly reflects changes in mass distribution below the surface, except the Bouguer anomaly has had an additional correction, removing the effect of mass above sea level datum on land (Lillie, 1999). The Bouguer gravity anomaly is the most frequently used of the gravity anomalies in surveys of continental and in near shore marine areas (Hinze et al., 2013). The variation of the Bouguer anomaly should reflect the lateral variation in density such that a high density feature in a lower density medium should give rise to a positive (+Ve) Bouguer anomaly. Conversely, a low density feature in a high density medium should result in a negative (-Ve) Bouguer anomaly (Reynolds, 1997). Bouguer anomaly is the difference between the measured gravity value at the point of observation and the theoretical value calculated for that station, by considering a bouguer slab of appropriate density for the effect of earth's material between the geoid and the station. The simple Bouguer gravity anomaly (ΔgB_S) on land is computed from the free air gravity anomaly (Lillie, 1999). Complete Bouguer anomaly is equivalent to removing away everything above sea level and forms the basis for the interpretation of gravity data on land.

The Bouguer anomaly calculated by ignoring topographic effects is simple Bouguer anomaly (ΔgB_S)

$$\Delta gB_S = g_{obs} + FAC - BC - g_{\phi} \quad \text{.....3.19}$$

When the free-air, Bouguer and terrain correction are applied to the observed gravity, the resulting anomaly obtained by subtracting the standard theoretical gravity at the given latitude is called the complete Bouguer anomaly (ΔgB_C)

$$C.B.A = g_{obs} + FAC - BC - g_{\phi} + TC \quad \text{……3.20}$$

3.2.8.3 Isostatic gravity anomaly

Isostatic anomalies (IA) correspond to gravity anomalies resulting from a homogeneous crust having a flat surface, a standard reference density and constant thickness for the isostatic model (Airy-Heiskanen or Pratt-Heyford model). Thus it is given by the following equations:

Isostatic anomaly (IA) = Bouguer anomaly (BA) + Isostatic correction (IC)……3.21

3.3 Magnetic Method

3.3.1 Introduction

Like the gravity method, the magnetic method is a passive geophysical exploration technique in that it is based on mapping the natural or normal magnetic force field of the Earth (Hinze et al., 2013).The aim of a magnetic survey is to investigate subsurface geology on the basis of anomalies in the Earth's magnetic field resulting from the magnetic properties of the underlying rocks (Kearey et al., 2002). Although most rock-forming minerals are effectively non-magnetic, certain rock types contain sufficient magnetic minerals to produce significant magnetic anomalies. Similarly, man-made ferrous objects also generate magnetic anomalies. Magnetic surveying thus has a broad range of applications, from small scale engineering or archaeological surveys to detect buried metallic objects, to large-scale surveys carried out to investigate regional geological structure. Magnetic and gravity methods have much in common, but magnetics is generally more complex and variations in the magnetic field are more erratic and localized (Telford et al., 1990). This is partly due to the difference between the dipolar magnetic field and the mono-polar gravity field, partly due to the variable direction of the magnetic field, whereas the gravity field is always in the vertical direction. In addition, magnetic field varies with time whereas gravity field is time invariant (ignoring small tidal variations).The magnetic method has come into use for identifying and locating masses of hot igneous rocks that have relatively high concentrations of magnetite (Mohammad Zadeh et al., 2012). The magnetic rocks include basalt and gabbro, granite, granodiorite and rhyolite have only moderately high magnetic susceptibilities. The magnetic method is useful in mapping near-surface volcanic rocks that are kind of interest rocks in geothermal exploration (Zhdanov, 1994). In the USA, for example, a ground magnetic survey over the Coso volcanic field in California recorded low anomalies associated with the geothermal prospect (Roquemore, 1984). It is known that an area may have a geothermal power deposition if and only if the following four main factors occur at the same place simultaneously (e.g. Mohammad Zadeh et al., 2012):

1. A natural heat source of great output such as cooling magma;

2. An adequate water supply;

3. An «aquifer» or permeable reservoir and

4. An impermeable cap rock.

In geothermal application the main objective of the magnetic study is to contribute with information about the relationship among the geothermal activity, the tectonic and stratigraphy of the area by means of the anomalies interpretation of the underground rocks' magnetic properties (Escobar, 2005). Most of the rocks are not magnetic; however, certain types of rocks contain enough minerals to originate significant magnetic anomalies. The data interpretation that reflects differences in local abundance of magnetization is especially useful to locate faults and geologic contacts (Blakely, 1995).

3.3.2 Basic concepts and elementary theory

The theories of magnetic field are similar to that of electric and gravity in that, point magnetic poles are analogues to point electrical charges and point masses (Telford et al., 1990). Within the vicinity of a bar magnet a magnetic flux is developed which flows from one end of the magnet to the other (Fig. 3.8).This flux can be mapped from the directions assumed by a small compass needle suspended within it. The points within the magnet where the flux converges are known as the poles of the magnet. A freely-suspended bar magnet similarly aligns in the flux of the Earth's magnetic field. The pole of the magnet which tends to point in the direction of the Earth's North Pole is called the north-seeking or positive pole, and this is balanced by a south-seeking or negative pole of identical strength at the opposite end of the magnet (Kearey et al., 2002). The force **F** between two magnetic poles of strengths $\mathbf{p_1}$ and $\mathbf{p_2}$ separated by a distance **r** is given by:

$$F = \frac{\mu_o p_1 p_2}{4\pi \mu_R r^2} \ldots\ldots\ldots\ldots\ldots\ldots 3.22$$

Where, F is magnetic force;

μ_o and μ_R are constants corresponding to the magnetic permeability of vacuum and the relative magnetic permeability of the medium separating the poles respectively;

p_1 and p_2 are pole strengths and r is the distance between them.

The force is attractive if the poles are of different sign and repulsive if they are of like sign. Magnetic field strength, also called magnetic intensity or magnetic field intensity is the part of

the magnetic field in a material that arises from an external current and is not intrinsic to the material itself. It is expressed as the vector **H** and is measured in units of amperes per meter. The magnetic field strength, **H**, is defined as the force per unit pole strength exerted by a magnetic monopole $\boldsymbol{p_1}$. On the other hand magnetic field is nothing more than Coulomb's expression divided by $\boldsymbol{p_2}$. Thus, the magnetic field strength **H** is the magnetic analog to the gravitational acceleration, $\boldsymbol{g}$. The magnetic field **H** due to a pole of strength **p** at a distance **r** from the pole is defined as the force exerted on a unit positive pole at that point which is given by:

$$H = \frac{\mu_o p}{4\pi\mu_R r^2} \ldots\ldots\ldots\ldots\ldots\ldots .3.23$$

Where, the unit of force is Newton and of the magnetic monopole is Ampere-meter. Therefore, the unit of the magnetic field strength is Newton per Ampere-meter, N/(Amp-m). (Amp-m) is referred to as a tesla (T), named after the renowned inventor Nikola Tesla.

The magnetic flux density (B) is a measure of the actual magnetic field within a material considered as a concentration of magnetic field lines, or flux, per unit cross-sectional area. The magnetic flux lines between two poles per unit area, is the flux density **B** (and is measured in weber/m2 = Tesla). **H**, which is also called the "magnetic induction", is a vector quantity. The unit of Tesla are too large to be practical in geophysical work, so a sub-unit called a nanotesla (1 nT = 10^{-9} T) is used instead, where 1nT is numerically equivalent to 1 gamma in c.g.s. units (1 nT is equivalent to 10-5 gauss). The ratio of the flux density **B** to the magnetizing field strength **H** is a constant called the absolute magnetic permeability (μ).

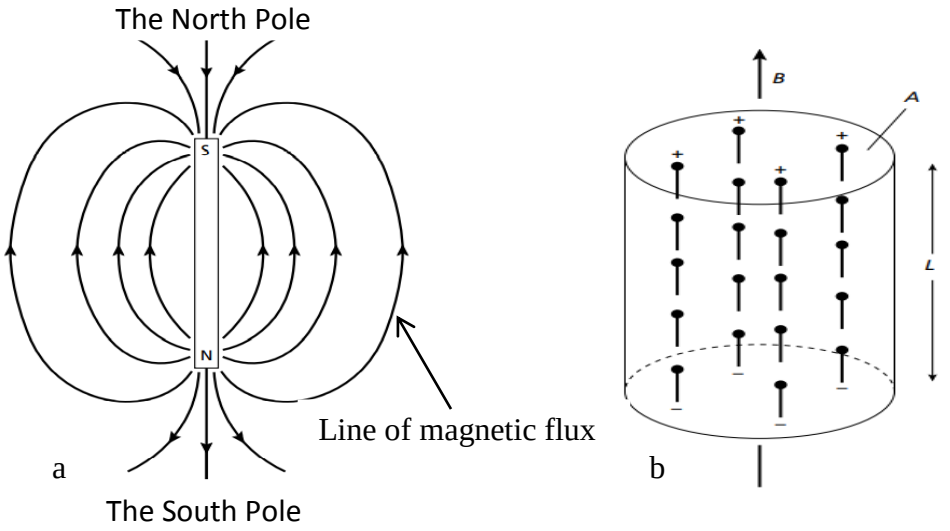

Figure 3.8 (a) the magnetic flux surrounding a bar magnet and (b) Schematic representation of an element of material in which elementary dipoles align in the direction of an external field B to produce an overall induced magnetization

Magnetic fields can be defined in terms of magnetic potentials in a similar manner to gravitational fields (Kearey et al., 2002). For a single pole of strength p, the magnetic potential V at a distance r from the pole is given by:

$$V = \frac{\mu_o p}{4\pi\mu_R r} \ldots\ldots\ldots\ldots\ldots\ldots\ldots\ldots 3.24$$

The magnetic field component in any direction is then given by the partial derivative of the potential in that direction. In the SI system of units, magnetic parameters are defined in terms of the flow of electrical current (e.g. Reilly, 1972). If a current is passed through a coil consisting of several turns of wire, a magnetic flux flows through and around the coil annulus which arises from a magnetizing force **H**. The magnitude of **H** is proportional to the number of turns in the coil and the strength of the current, and inversely proportional to the length of the wire, so that **H** is expressed in ampere per meter. The density of the magnetic flux, measured over an area perpendicular to the direction of flow, is known as the magnetic induction **B** of the coil which is given by: $B=\mu_0 H$. **B** is proportional to **H** and the constant of proportionality $\boldsymbol{\mu_0}$ is known as the magnetic permeability of free space and has a value (in SI) $4\pi*10^{-7}$. Lenz's law of induction relates the rate of change of magnetic flux in a circuit to the voltage developed within it, so that **B** is expressed in Vsm^{-2} (Weber (Wb) m^{-2}). The unit of the Wbm^{-2} is designated the tesla (T). Permeability is consequently expressed in $WbA^{-1}m^{-1}$ or Henry $(H)m^{-1}$. The c.g.s. unit of magnetic field strength is the gauss (G), numerically equivalent to 10^{-4}T. The tesla is too large a unit in which to express the small magnetic anomalies caused by rocks and a subunit, the nanotesla (nT), is employed ($1nT = 10^{-9}T$). The c.g.s. system employs the numerically equivalent gamma (g), equal to 10^{-5}G. Common magnets exhibit a pair of poles and are therefore referred to as dipoles. The magnetic moment **M** of a dipole with poles of strength **p** and a distance **r** apart is given by:

M = pr……..3.25

The magnetic moment of a current-carrying coil is proportional to the number of turns in the coil, its cross-sectional area and the magnitude of the current, so that magnetic moment is expressed in Am^2. When a material is placed in a magnetic field it may acquire a magnetization in the direction of the field which is lost when the material is removed from the field. This phenomenon is referred to as induced magnetization or magnetic polarization, and results from the alignment of elementary dipoles within the material in the direction of the field. As a result of this alignment of the material has magnetic poles distributed over its surface which correspond to the ends of the dipoles (Fig. 3.9). The intensity of induced magnetization $\mathbf{J_i}$ of a material is defined as the dipole moment per unit volume of material:

$J_i = \frac{M}{LA}$……3.26

where M is the magnetic moment of a sample of length L and cross-sectional area A. J_i is consequently expressed in Am^{-1}. In the c.g.s. system intensity of magnetization is expressed in $emucm^{-3}$ (emu = electromagnetic unit), where $1emucm^{-3} = 1000Am^{-1}$. The induced intensity of magnetization is proportional to the strength of the magnetizing force H of the inducing field:

$J_i = kH$…….3.27

Where, k is the magnetic susceptibility of the material. Since J_i and H are both measured in Am^{-1} , susceptibility is dimensionless in the SI system. In the c.g.s. system susceptibility is similarly dimensionless, but a consequence of rationalizing the SI system is that SI susceptibility values are a factor 4π greater than corresponding c.g.s. values. In a vacuum the magnetic field strength Band magnetizing force H are related by $B=\mu_0 H$ where μ_0 is the permeability of vacuum ($4\pi*10^{-7}Hm^{-1}$). Air and water have very similar permeability's to μ_0 and so this relationship can be taken to represent the Earth's magnetic field when it is undisturbed by magnetic materials. When a magnetic material is placed in this field, the resulting magnetization gives rise to an additional magnetic field in the region occupied by the material, whose strength is given by $\mu_0 J_i$. Within the body the total magnetic field, or magnetic induction, B is given by:

$B=\mu_0 H + \mu_0 J_i$……..3.28

Substituting equation 3.27

$B=\mu_0 H + \mu_0 kH = (1+k)\ \mu_0 H = \mu_R\ \mu_0 H$……3.29

Where, μ_R is a dimensionless constant known as the relative magnetic permeability. The magnetic permeability m is thus equal to the product of the relative permeability and the permeability of vacuum, and has the same dimensions as μ_0. For air and water μ_R is thus close to unity.

3.3.3 Magnetic susceptibility and intensity of magnetization

The geologically diagnostic parameter, magnetic susceptibility, k (equation 3.29), is measure of how susceptible a material is to becoming magnetized. The susceptibility (k) values ranges from -1 to 1 and for a vacuum, μ_r =1and k=0 which we called intensity of magnetization induced by the magnetizing force, H. Magnetization in the presence of applied external field H is called induced magnetization whereas the existence of measurable field in the absence of the external field is known as permanent or remanent magnetization (J_r). A rock mass containing magnetic minerals will have an induced as well as a remanent magnetization. The magnitude and orientation of the resultant (J) dictate both the amplitude and shape of a magnetic anomaly (Fig. 3.10).

3.3.4 The geomagnetic field and its component

Geomagnetism refers to the study of magnetic phenomena exhibited by the Earth and its atmosphere. Although the existence of the geomagnetic field has been recognized for a very long period of time (it was not until 1843), the variations in the field were used to locate deposits of magnetic ores (Telford et al., 1990). Unlike the gravity field (only varies in magnitude), the magnetic field observed at the Earth's surface varies considerably both in direction and magnitude (Milsom, 2003). Kearey et al., (2002) also verifies that the geomagnetic field is geometrically more complex than the gravity field of the Earth and exhibits irregular variation in both orientation and magnitude with latitude, longitude and time. The Earth's magnetic field strength varies from about 30000nT at the equator to around 60000nT at the poles. The main causes of the geomagnetic field is attributed to a dynamo action produced by the circulation of charged particles in coupled convictive cells within the liquid earth's outer core.

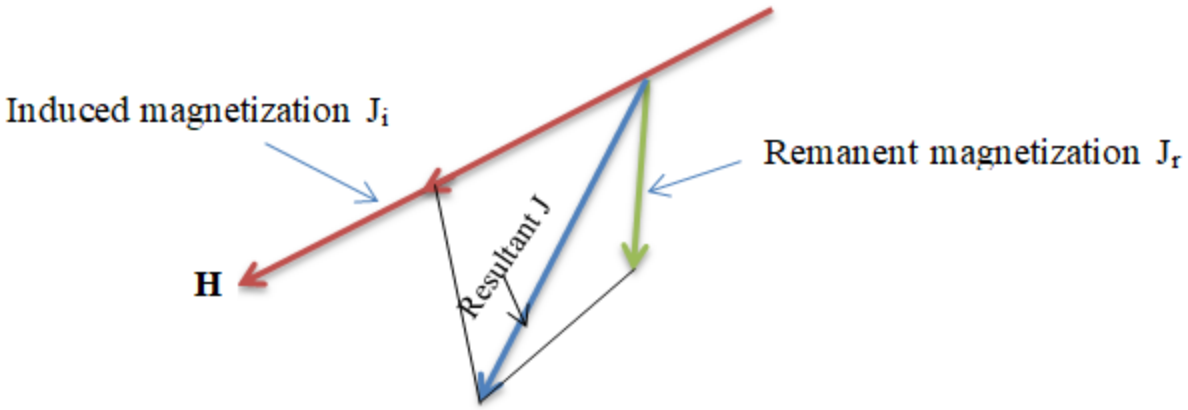

Figure 3.9 Vector diagram illustrating the relationship between induced (Ji), remanent (Jr) and total (J) magnetization components

There are three components of the Earth's magnetic field. These are A) the main dipole field, B) the rock magnetization field and C) the external field.

A. **The main dipole field -** This field represents the main components of the geomagnetic field and is believed to be originated in the Earth's outer core. This field varies relatively slowly and its magnitude on the earth's surface is given in terms of the geomagnetic field elements (Fig. 3.11). A vector is used to represent the Earth's magnetic field at an observation site (Kearey et al., 2002). The vector is described by a combination of seven quantities known as the magnetic elements (Fig. 3.11). The total field vector B has a vertical component Z and a horizontal component H in the direction of magnetic north. Inclination I is the angle between the directions of the B-field and the horizontal plane. Magnetic declination D is the horizontal angle between the geographic north and the magnetic north that is indicated by a compass. The horizontal component H can be further decomposed into a component X in the geographical north direction and a component Y in the geographical east direction.

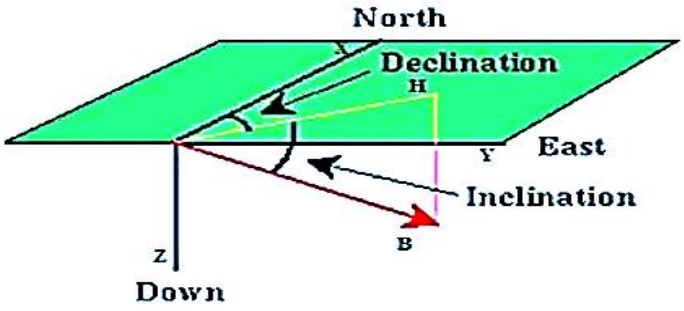

Figure 3.10 Elements of the Earth's magnetic field

The relationship between the seven earth's magnetic elements is given as follows:

$X = H\cos D$……3.20(a) $Y = H\sin D$…….3.20(b) $H = \sqrt{X^2 + Y^2}$…….3.20(c)

$H = B\cos I$……3.20(d) $Z = B\sin I$…...3.20(e) $B = \sqrt{H^2 + Z^2} = \sqrt{X^2 + Y^2 + Z^2}$….3.20(f)

Where, H, Z, D magnetic elements recorded at geomagnetic observatories. Any combination of three magnetic elements is sufficient to completely describe the Earth's magnetic field vector at an observation site.

B. **The rock magnetization field –** This is derived from the magnetization of rocks which depends on the magnetic mineral content of near surface rocks. This is the most important component of geomagnetic field in exploration geophysics. The sources of local magnetic anomalies cannot be very deep because of the Curie temperature, associated with features in the upper crust (Telford et al., 1990).

C. **The external field** - Electric currents in the ionized layers of the atmosphere, magnetosphere, results the remaining small portion of the geomagnetic field which is more rapid in time. The external field has a quite complicated appearance as it is strongly affected by the solar wind (Lowrie, 2007). The total magnetic field which is the sum of its components, is given by:

$B_T = B_{ext} + B_{int} = B_{ext} + B_D + B_{rm}$…… (3.21) Where, B_T=total field, B_{ext}=external field, B_D=dipole field, and B_{rm}=field of rock magnetism.

3.3.5 Variations in the geomagnetic field

The cause of the geomagnetic field is attributed to a dynamo action produced by the circulation of charged particles in coupled convective cells within the fluid earth's outer core. The exchange of dominance between such cells is believed to produce the periodic changes in polarity of the geomagnetic field revealed by palaeomagnetic studies. The circulation patterns within the core are not fixed and change slowly with time. That means the geomagnetic field cannot in fact result from permanent magnetism in the Earth's outer core. This results the temporal variation of the Earth's magnetic field that can be explained in terms of three temporal variations.

1. **Secular variations**: The circulation patterns within the core are not fixed and change slowly with time. This is reflected in a slow, progressive, temporal change in all the geomagnetic elements known as secular variation. Such variation is predictable and a well-known example is the gradual rotation of the north magnetic pole around the geographic pole (Kearey et al., 2002). They are monitored by measuring changes in I, D and B at observatories. Since secular variation results from a very long period of time that result from convective changes from the core it will not complicate data reduction efforts.
2. **Diurnal variations**: It is the daily variation of the geomagnetic field due to magnetic effects of external origin. Under normal conditions the diurnal variation is smooth and regular and has an amplitude of about 20–80nT, being at a maximum in polar region (Kearey et al., 2002). Such variation results from the magnetic field induced by the flow of charged particles within the ionosphere towards the magnetic poles, as both the circulation patterns and diurnal variations vary in sympathy with the tidal effects of the Sun and Moon (Kearey et al., 2002).
3. **Magnetic storms:** Some days (disturbed days) are distinguished by far less regular diurnal variations and involve large short term disturbance in the geomagnetic field with amplitude of up to 1000nT, known as magnetic storm, during this period magnetic survey should be ceased. The occurrence of such storms correlates with enhanced sunspot activity. Magnetic surveying should be discontinued during such storms because of the impossibility of correcting the data collected for the rapid and high amplitude changes in the magnetic field. Therefore, it is difficult to correct for them in acquired data (Kearey et al., 2002).

3.3.6 Magnetic anomalies

All magnetic anomalies caused by rocks are superimposed on the geomagnetic field in the same way that gravity anomalies are superimposed on the Earth's gravitational field. The magnetic case is more complex because it is characterized by the direction and magnitude of the effective magnetization and the shape, position, properties and history of the anomalous body whereas the gravitational field is everywhere, by definition, vertical. A magnetic anomaly is a local or regional disturbance caused by a change in the magnetization.

To obtain magnetic anomalies associated with local magnetic variations of rocks, it is necessary to remove the normal geomagnetic field from the data. The normal geomagnetic field used for the reduction was the International Geomagnetic Reference Field (IGRF). The anomaly depends on its magnetic latitude and the corresponding variation of the dip angle of the magnetization vector in the body.

A magnetic anomaly originates from the susceptibility contrasts between susceptibility of anomalous rock body and the susceptibility of the surrounding rock. The shape of magnetic anomaly depends not only on the shape and depth of the anomalous body but also on its orientation with respect to the direction of the profile considered and with respect to the direction of the inducing magnetic field, which itself varies in intensity and direction with respect to its geographical locations. The susceptibility contrast is due to induced magnetization Ji of crustal rocks.

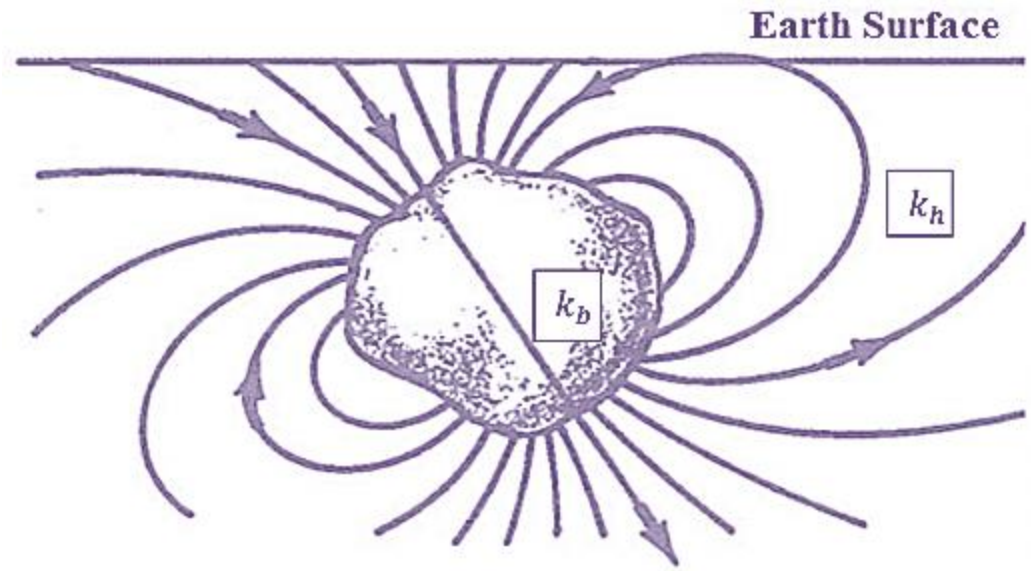

Figure 3.11 an ore body behaves like a huge buried magnet (after Buriner, 1999)

If k_b represent the susceptibility of an anomalous body and k_h is the susceptibility of the host rocks, the susceptibility contrasts Δk is given by:

$\Delta k = k_b - k_h$ ……..3.22

If $\Delta k > 0$ the magnetic anomaly is positive and $\Delta k < 0$ shows magnetic anomaly.

3.3.7 Magnetic data reduction

According to Kearey et al., (2002) the reduction of magnetic data is necessary to remove all causes of magnetic variation from the observations other than those arising from the magnetic effects of the subsurface.

Diurnal variation correction: The effects of diurnal variation may be removed in several ways. For ground magnetic survey a method similar to gravimeter drift monitoring may be employed in which the magnetometer is read at a fixed base station periodically throughout the day. The differences observed in base readings are then distributed among the readings at stations occupied during the day according to the time of observation (Kearey et al., 2002). It should be remembered that base readings taken during a gravity survey are made to correct for both the drift of the gravimeter and tidal effects; magnetometers do not drift and base readings are taken solely to correct for temporal variation in the measured field. Such a procedure is inefficient as

the instrument has to be returned periodically to a base location and is not practical in marine or airborne surveys. These problems may be overcome by use of a base magnetometer, a continuous-reading instrument which records magnetic variations at a fixed location within or close to the survey area. This method is preferable on ground survey as the survey proceeds faster and the diurnal variations are fully charted. Where the survey is of regional extent the records of a magnetic observatory may be used. Such observatories continuously record changes in all the geomagnetic elements. However, diurnal variations differ quite markedly from place to place and so the observatory used should not be more than about 100km from the survey area.

$$\delta B_D = B_i \pm [\frac{\Delta B}{\Delta t}] \Delta t_i \quad \text{.....3.23}$$

Where, δB_D = diurnally corrected data measured at time t_i, B_i = magnetic field measured at time t_i, $\Delta B = B_2 - B_1$; where B_1 and B_2 are base station reading at the beginning and end of the survey respectively. $\Delta t = t_2 - t_1$, where, t_1 and t_2 are base station time reading at the beginning and end of the survey respectively and $\Delta t_i = t_i - t_1$ is the time difference of any station and base station respectively.

Geomagnetic correction: The magnetic equivalent of the latitude correction in gravity surveying is the geomagnetic correction which removes the effect of a geomagnetic reference field from the survey data. The most rigorous method of geomagnetic correction is the use of the IGRF, which expresses the undisturbed geomagnetic field in terms of a large number of harmonics and includes temporal terms to correct for secular variation. The complexity of the IGRF requires the calculation of corrections by computer. It must be realized, however, that the IGRF is imperfect as the harmonics employed are based on observations at relatively few, scattered, magnetic observatories. The IGRF is also predictive in that it extrapolates forwards the spherical harmonics derived from observatory data. Consequently, the IGRF in areas remote from observatories can be substantially in error (Kearey et al., 2002).

The magnetic equivalent of latitude correction is IGRF correction given by:

$$B_{IGRF-corrected} = \delta B_D - IGRF \quad \text{.....3.24}$$

Where, $B_{IGRF-corrected}$ = IGRF corrected total magnetic intensity, δBD is diurnally corrected magnetic intensity value and IGRF is the International Geomagnetic Reference Field value defined by its latitude.

CHAPTER FOUR

DATA ACQUISITION, PROCESSING AND PRESENTATION

4.1 Introduction

Gravity and magnetic methods are utilized in this thesis work. The data used for the gravity method are secondary data obtained from previous sources (as explained in sections 4.2.1). The magnetic data include secondary data obtained from previous sources (as explained in sections 4.3.1) and primary data collected by the researcher and his advisor. Both the gravity and magnetic data utilized in this thesis work were collected in a random distribution fashion. A brief description of the data acquisition and consequent reduction processes associated with both geophysical methods are summarized below.

4.2 The gravity data

4.2.1 Gravity data acquisition and distribution

A total of about 688 gravity data with an average spacing of 2-4km between consecutive measurement stations has been utilized in this thesis work. The distribution fashion of the points is random that follows seasonal roads, dry weather roads (gravel and asphalt) and off road transect (Fig. 4.1). As can be seen from (Fig. 4.1) there is good gravity data coverage throughout the study area. The gravity data obtained for this thesis work were collected by individual researchers (Abera Alemu, 1983; 1992) and the Ethiopian geological survey (EGS). The secondary data acquired and reprocessed from the work of Abera Alemu (1983; 1992), were collected using the Worden type gravimeter and Lacoste and Romberg model G gravimeter with reading precession of 0.1 and 0.05mGal, respectively. The secondary gravity data obtained from the EGS as cited in their survey reports were collected using the Lacoste and Romberg Model 304 gravimeter which also has a precision of 0.05mGal. All the secondary gravity data are uniformly tide to the International Gravity Standardization Net 1973 (IGSN 1973) gravity datum.

The theoretical gravity, g at latitude ϕ, is calculated using the 1967 gravity formula (Geodetic reference system 1967; Moritz, 1971).

The survey reports of the secondary gravity data indicate that station locations (Latitude, Longitude and elevations) were determined using classical surveying instruments (altimeters, theodolits) and hand held global positioning system (GPS).

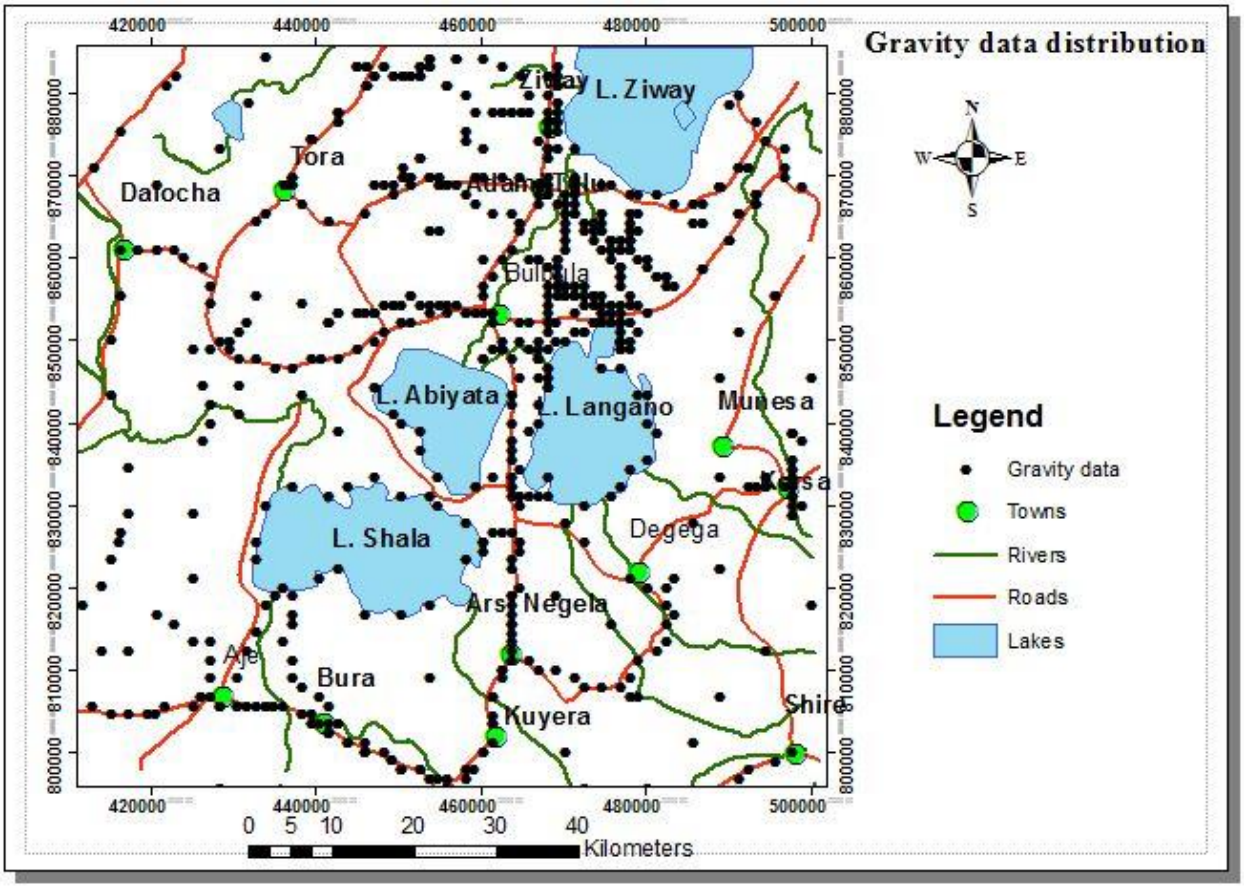

Figure 4.1 Gravity data distribution of the study area

4.2.2 Gravity data processing

4.2.2.1 Gravity data reduction

Before the results of a gravity survey are interpreted it is necessary to correct for all variations in the Earth's gravitational field which do not result from the differences of density in the underlying rocks (Kearey, et al., 2002). Observed gravity is the combined effects of instrumental, elevation, terrain and planetary sources in addition to the subsurface lateral mass variations that

are the objective of an exploration gravity survey (Hinze et al., 2013). All the secondary gravity data have been reprocessed by applying the standard gravity data correction procedures (Section 3.2.7) and using the average crustal density 2.67g/cm^3.

Finally, the end results of the gravity survey data including the free-air anomaly values and complete Bouguer anomaly values of all stations considered in this thesis work have been determined as part of the processing sequence using the Geosoft Oasis Montaj (version 7.1) gravity and magnetic data processing and mapping software.

4.2.2.2 Gravity data gridding and mapping

The computed free-air anomaly and complete Bouguer anomaly values including their corresponding elevation values have been regularly interpolated on a 0.3×0.3 km square grids and gridded using minimum curvature gridding option of the Geosoft Oasis Montaj (version 7.0) software (Section 5.1). Following the gridding, the elevation map (Fig. 5.1), the free-air anomaly map (Fig. 5.2) and the complete Bouguer anomaly map (Fig. 5.3) of the study area are compiled for further data processing (enhancing, mapping and modeling).

4.2.2.3 Regional – residual gravity anomaly separation and data enhancement

According to Tilahun Mammo (2010), prior to modeling the gravity data, relevant information can be extracted from the gravity data itself using various filtering techniques. This means that only reduction of gravity data into anomaly form can't enable us to translate the anomaly to reliable subsurface geological information. Techniques known as data enhancement or filtering help us to highlight anomalies of preference through certain spectral aspects of observed Bouguer gravity anomaly. In this regard, a suit of carefully chosen enhancement techniques enables us to shed structural trends, fault kinematics and intrusive bodies.

Before gravity data interpretation the most and primarily important step is the regional-residual separation of gravity anomaly which is part of data enhancement/flittering in the present study. The observed gravity anomaly represents the total effect of deep seated geologic sources which results long wavelength anomalies and shallow geologic sources that give rise to short wavelength anomalies. Detail analysis of gravity data needs to separate the regional from the observed data called regional-residual separation. This requires estimating the regional anomaly

using an appropriate standard technique so that the estimated regional component can be subtracted from the complete Bouguer to determine the residual anomaly component.

In this thesis work, the upward continuation filtering technique is used to estimate the regional gravity anomaly component. This technique suppress all the short wavelength (residual) components arising from shallow sources and enhances the long wave length (regional) components arising from deep seated sources. The residual gravity anomaly is obtained by subtracting estimated regional anomaly from the complete Bouguer anomaly (Section 5.1.2).

4.3 Magnetic data

4.3.1 Magnetic data acquisition and distribution

A total of about 458 magnetic data has been utilized in this thesis work. From a total of about 458 magnetic data 350 magnetic data is obtained from previous MSc thesis works. And a total of about 108 magnetic data is collected by the researcher and his advisor during the field work (Fig. 4.2). The distribution fashion of the point is random that follows seasonal roads, dry weather roads (gravel and asphalt) and off road transect (Fig. 4.3). The station interval of the magnetic data is 2-4km depending up on the change in surface geology. Geographic coordinates of the measurement stations are acquired using a hand Global Positing System (GPS) with an accuracy of 1-3m and magnetic data is measured using Earth magnetometer with an accuracy of 0.003nT. Before any measurement is made, a base station for all the observations occupied was established for the purpose of correcting the diurnal effect. For this purpose more than 25% of the stations were re-measured to verify the quality of the dataset and to allow for uncertainty calculation.

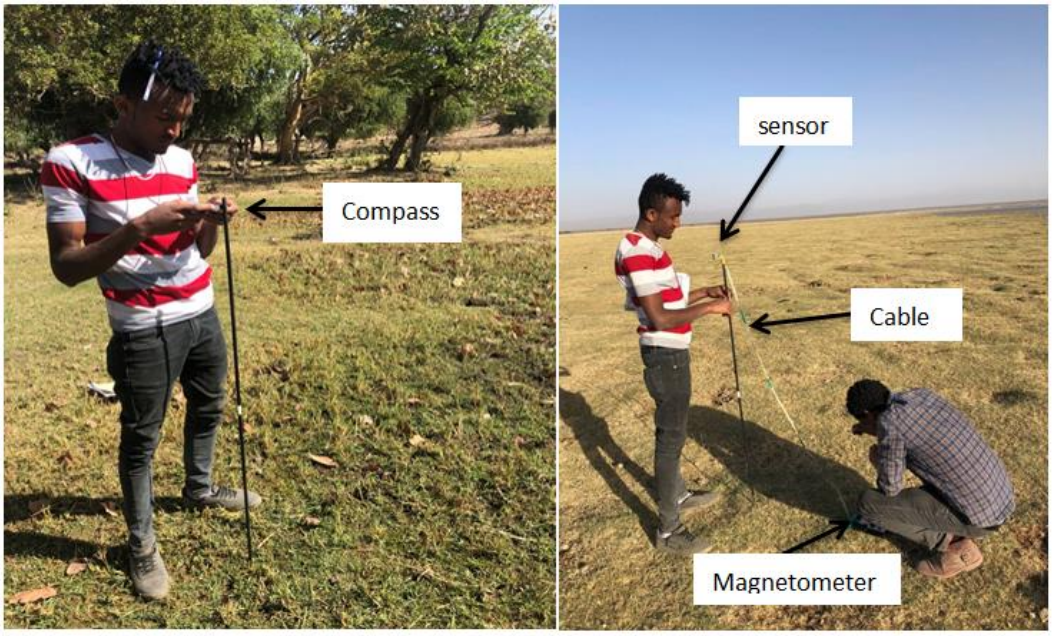

Figure 4.2 Magnetic data acquisition using Earth magnetometer (EM-2)

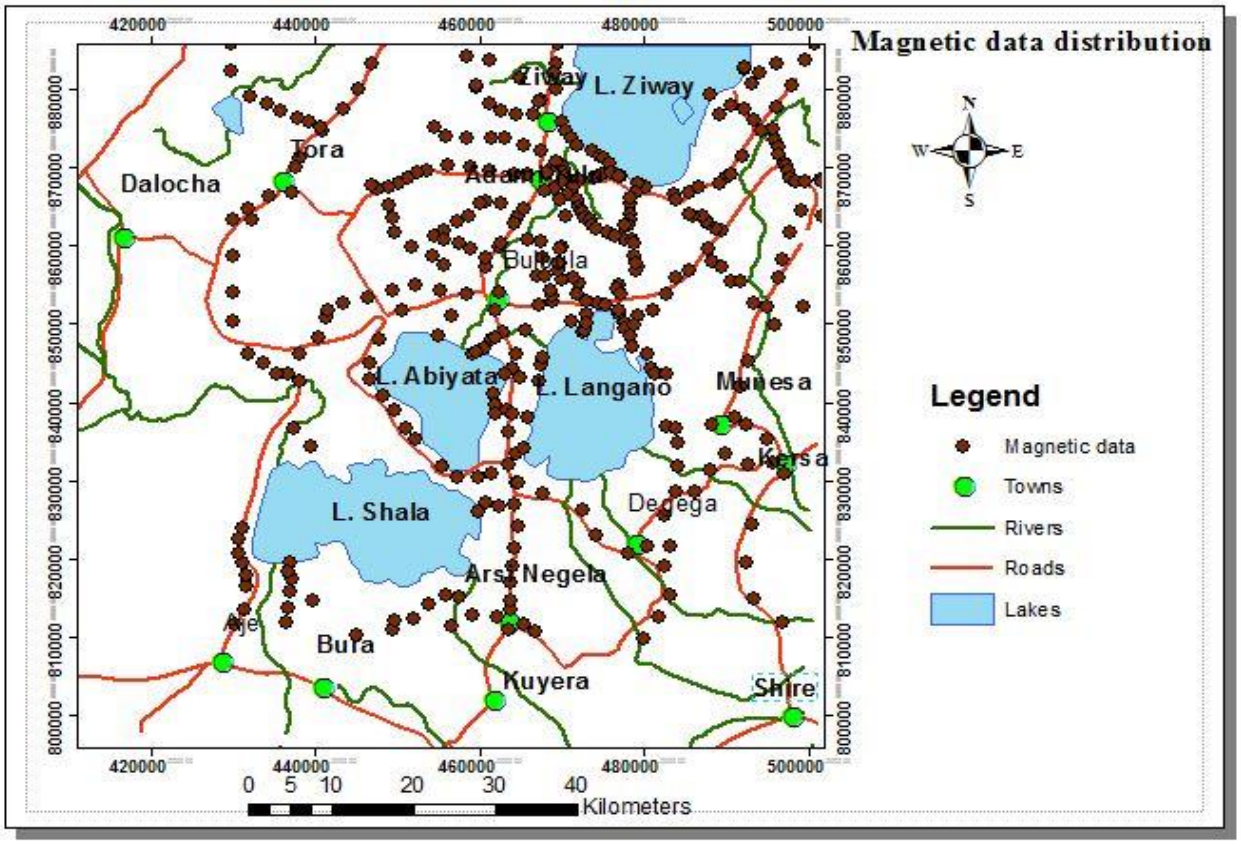

Figure 4.3 Magnetic data distribution of the study area

4.3.2 Magnetic data processing

4.3.2.1 Magnetic data reduction

Reduction of magnetic survey data principally aims at removing the effects of temporal variations in the earth's magnetic field that occur during the course of the survey, usually the diurnal effect (Dentith and Mudge, 2014, pp.116). That means magnetometers do not give the direct measurement of magnetic data for interpretation as additional factors affect the instruments. As a result, field observations are processed to minimize or remove these extraneous effects that result from indirect geological interest. This conversion procedure is commonly referred to as correction or reduction of the magnetic data.

In this thesis work, the effect of man-made objects and magnetic storms were tried to reduce by avoiding a magnetic survey measurements in the presence of such conditions. Diurnal correction of both the secondary and primary data were eliminated by a process called diurnal correction as discussed in Section 3.3.7. The diurnally corrected data (total magnetic intensity) were also further processed for IGRF correction to get the total magnetic anomaly at each station of the area. Thus, magnetic anomaly is nothing but the remaining magnetic field strength after taking into accounts the effect of all non-geologic factors, applying both diurnal and IGRF correction in the case of this work.

4.3.2.2 Magnetic data gridding and mapping

After the final reduced magnetic data was compiled the reduced magnetic values are regularly interpolated on a 1×1km square grids and gridded using minimum curvature gridding option of the Geosoft Oasis Montaj software (version 7.1). Following the gridding, the total magnetic intensity map (Fig. 5.12), the total magnetic anomaly map (Fig. 5.13) and the pole reduced total magnetic anomaly map (Fig. 5.14) of the study area are compiled for further data processing (enhancing, mapping and modeling).

4.3.2.3 Regional-residual magnetic anomaly separation and data enhancement

Only reduction of magnetic data into anomaly form cannot enable us to translate the anomaly to the correct subsurface geological information. Techniques known as data enhancement or filtering helps us to highlight anomalies of preference through certain spectral aspects of the pole

reduced total magnetic anomaly. In this regard, a suit of carefully chosen enhancement techniques enables us to shed structural trends, fault kinematics and intrusive bodies. The pole reduced total magnetic anomaly is the total effect of deep seated geologic sources which results long wavelength anomalies and shallow geologic sources that give rise to short wavelength anomalies. Detail analysis of magnetic data needs to separate the regional from the observed data called regional-residual separation. This requires estimating the regional anomaly using an appropriate standard technique so that the estimated regional component can be subtracted from the total magnetic anomaly to determine the residual anomaly component.

Before magnetic data interpretation the most and primarily important step is the regional-residual separation of magnetic anomaly which was part of data enhancement/filtering in the present work. In this thesis work, the upward continuation technique is used to estimate the regional gravity anomaly components. The upward continuation technique suppress all the short wavelength (residual) components arising from shallow sources and enhances the long wave length (regional) components arising from deep seated sources. Finally, the residual magnetic anomaly is obtained by subtracting the regional magnetic anomaly from the total magnetic anomaly.

4.3 Data presentation

Data presentation is one of the key stages in every gravity and magnetic survey which assists our interpretation. A successful geophysical survey needs careful data acquisition, processing, presentation and interpretation as given in the thesis flow chart (Fig. 1.3). Translating gravity and magnetic data results into geology requires an appropriate data presentation. The processed data of the two potential fields are presented in the form of profiles (1D), maps (2D) or models (2D or 3D).

In this thesis the final gravity data is presented in the form of free air anomaly map (Fig. 5.2), complete Bouguer anomaly map (Fig. 5.3), regional anomaly map (Fig. 5.5), residual anomaly map (Fig. 5.6) and derivative maps. The derivative maps include horizontal derivative map (Fig. 5.7), Analytical signal map (Fig. 5.8), Tilt derivative map (Fig. 5.9) and Euler Deconvolution map (Fig. 5.10 and Fig. 5.11). Moreover, an attempt has been made to present the gravity data in the form of 2D forward models (Fig. 6.2 and Fig. 6.3).

The magnetic data of this thesis work is presented in the form of maps including: the total magnetic intensity map (Fig. 5.12), the total magnetic anomaly map (Fig. 5.13), the pole reduced total magnetic anomaly map (Fig. 5.14), the regional magnetic anomaly map (Fig. 5.15), the residual magnetic anomaly map (Fig. 5.16) and derivative maps. The derivative maps include Analytical signal map (Fig. 5.17), Tilt derivative map (Fig. 5.18) and Euler Deconvolution map (Fig. 5.19 and Fig. 5.20).

CHAPTER FIVE

RESULTS, ANALYSIS AND INTERPRETATIONS

5.1 Gravity data Results, analysis and Interpretations

The gravity data utilized for this thesis work has a sufficient areal coverage and high resolution in order to interpret the subsurface geology of the study area at a local and semi-regional scale. Interpretation of the subsurface geology of the study area requires careful data processing and enhancement techniques. In the present work free air anomaly and complete Bouguer anomaly are considered since both are highly correlated with elevation of the study area.

5.1.1 Topographic and free-air anomaly maps

The topographic map (Fig. 5.1) is compiled from elevations of the observation point by using the Geosoft OasisMontaj software (Version 7.0). As can be observed from Figure 5.1 the study area is characterized by heterogeneously rugged topography. The highly elevated localities in the study area are located to the northwestern, western, southeastern and eastern parts of the study area. The NE-SW aligned lower elevated localities correspond to the rift floor of the CMER associated with quaternary volcanoes which appear to be reflected by circularly ridge shaped peaks. The transition from low lands (elevation up to 1527 m) of the rift floor including rift Lakes of the study area (Blue color) to high lands (elevation up to 3137 m) demarcates margins of the rift floor (pale yellow color). The transition zone (rift floor-elevated platforms) is marked by smoothly varying and elongated elevation contours (Fig. 5.1).

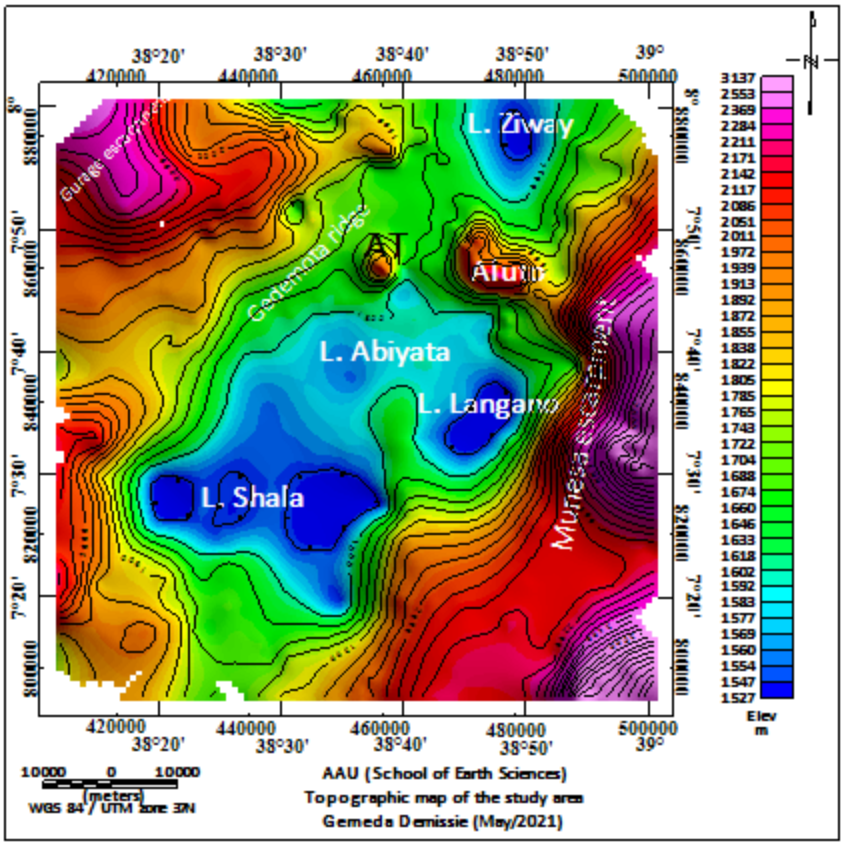

Figure 5.1 Topographic map of the study area. Where, AT is Adami Tulu

The free air anomaly (FAA) at each observation point is computed by applying the free air correction (Section 3.2.7.5). The free correction assumes existence of no topographic masses between the sea level and the observation point. Therefore, the free air correction compensates the observed gravity for the fact that it was measured at a given height above (or below) the mean sea level.

The free air anomaly map (Fig. 5.2) is compiled from the computed free air anomalies by using the Geosoft Oasis Montaj software (version 7.0). The free air anomaly map reveals values between -57mGal and 102mGal. The free air anomaly distribution is strongly correlated to the elevation of the gravity stations considered in the study area (Fig.5.1). Therefore, positive values of the FAA are correlated with the maximum topographic heights and the low anomaly values are associated with the rift floor which consists of the rift lakes (Lake Ziway, Lake Langano, Lake Abiyata and Lake Shala) of the study area.

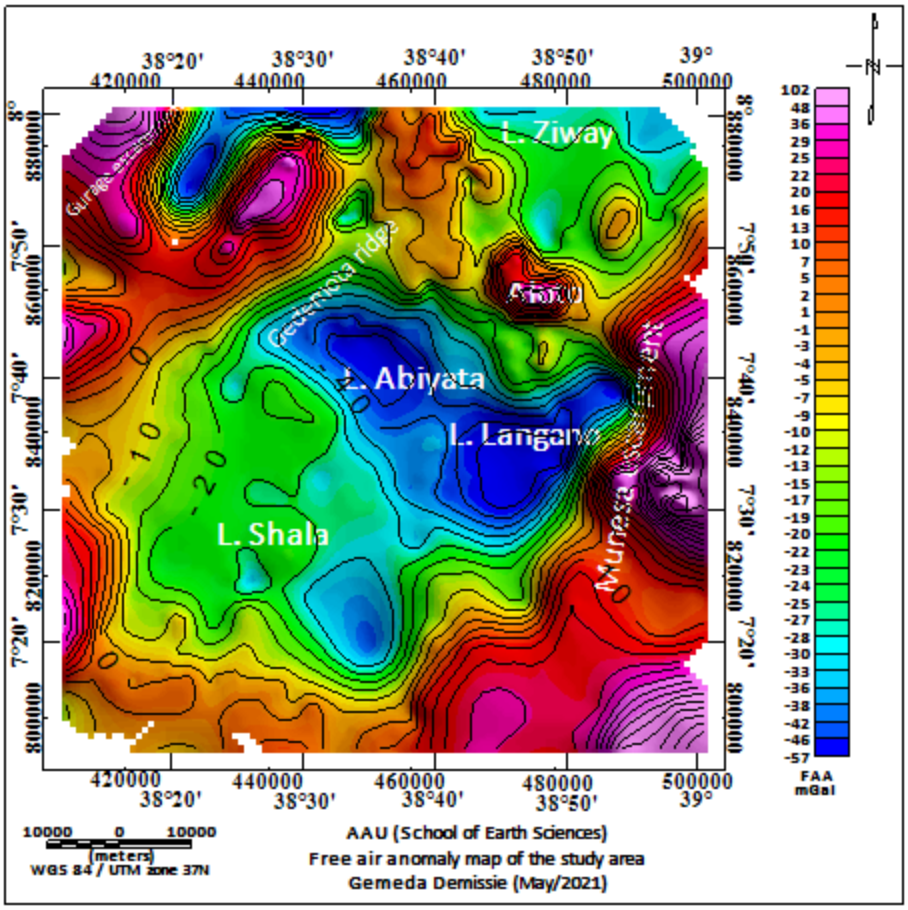

Figure 5.2 Free air gravity anomaly map of the study area

Figure 5.1 and Figure 5.2 generally appear to show that the pattern of the high and low elevation values and the corresponding high and low free air anomaly values verify existence of a positive correlation between elevation and free air anomaly (i. e. as elevation increases the corresponding free air anomalies also increases and vice versa). The rift floor, the Gedemota ridge and the Munesa escarpment are clearly demarcated (mapped) on both the free air and topographic maps and mark the major structural units (i. e. the Aluto volcano, the rift lakes, the Gedemota ridge and the Munesa escarpment) of the study area.

5.1.2 Complete Bouguer anomaly map

According to Hinze et al., (2013), the free air anomaly is not suitable for the interpretation of local gravity studies. Because it doesn't take into account the effect of masses between observation point and reference geoid. Therefore, the effect of the attraction of rock units between observation point and reference geoid can be precluded using Bouguer plate correction

(equation 3.15). The remaining gravity value after allowing the effect of elevation, theoretical gravity and the mass between observation point and geoid is simple Bouguer anomaly (Telford et al., 1990). In fact, for a Bouguer anomaly to be complete, the effect of topography (terrain correction) must be considered.

Closely examining the mathematical equations for CBA (equation 3.20) enables us to evaluate the effect of elevation in gravity survey. In this regard, it is better to consider the spatial variation in elevation of the area (Fig. 5.1) so as to interpret the subsurface geology based on gravity data. A casual glance of it implies that the spatial variation in Bouguer anomaly is negatively correlated with elevation (Fig. 5.1). This is verified by Hinze et al., (2013) who demonstrates the negative correlation of CBA and broad topographic variations that are isostatically compensated. Because of the relatively smaller size of the study area, the complete Bouguer anomaly map (Fig. 5.3) could be attributed to the effect of lower to upper crust density heterogeneities.

Figure 5.3 shows the complete Bouguer anomaly (CBA) map compiled for the study area which consists of the Aluto-Langano geothermal field and its environs. Three regions of gravity field signatures are observed by closely examining the CBA map: A relatively high CBA ranging from -185mGal to -210mGal and corresponding to the rift floor; a relatively intermediate CBA ranging from -211mGal to -225mGal and corresponding to the rift margins and a relatively low CBA ranging from -226mGal to -264mGal and corresponding to the Munesa and Gurage escarpments (Fig. 5.3).

The anomalous behavior of the gravity field over the Aluto region is clearly revealed by the CBA map (Fig. 5.3) by a sudden increase in the gravity anomaly.

The CBA map (Fig. 5.3) is the combined effect of deep (longer wavelength) and shallow (shorter wavelength) seated bodies. On the other hand, the shorter wavelength anomalies are masked by the longer wavelength anomalies. Hence, it is a difficult to get information regarding depth of shallow subsurface causative bodies. Therefore, it is compulsory to separate the regional and the residual anomaly and consequently employ the residual anomaly component for the sake of interpreting the gravity data in terms of shallow subsurface bodies and the regional anomaly component in terms of deep seated bodies.

In order to separate the regional and the residual anomaly data enhancement (filtering) techniques particularly the upward continuation technique is employed in this thesis work.

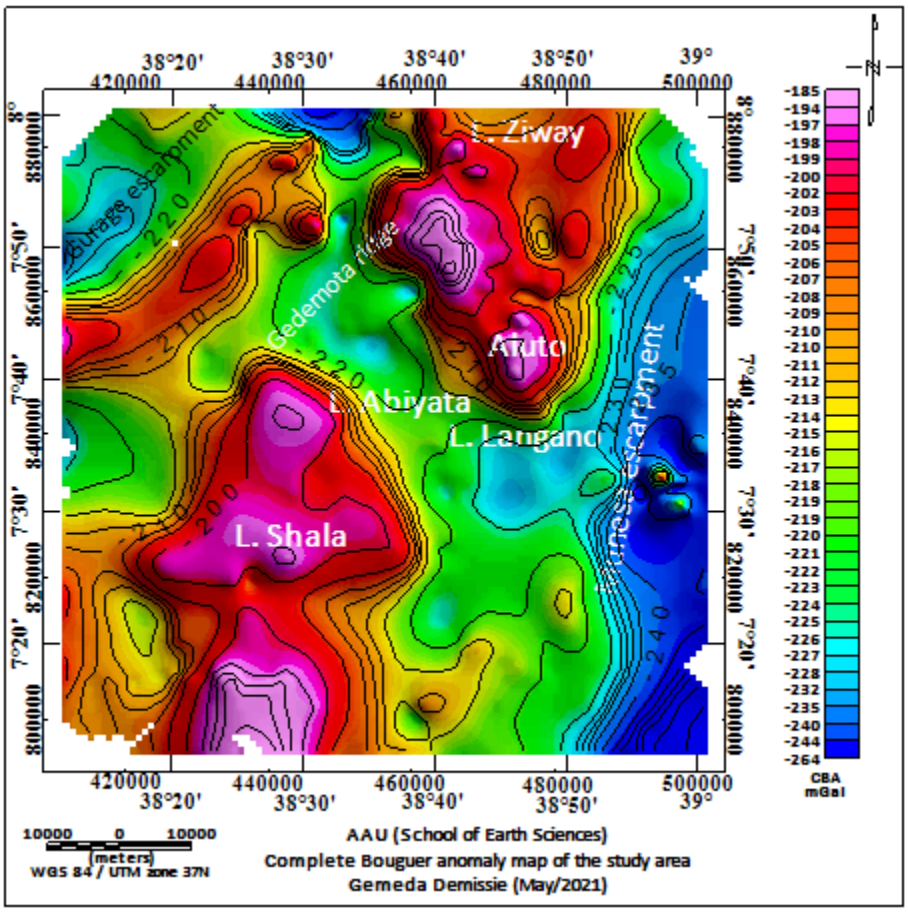

Figure 5.3 Complete Bouguer gravity anomaly map of the study area

5.1.2 Upward Continued Gravity Anomaly Map

According to Jacobsen (1987), the mathematical projection of potential fields like gravity field from a datum vertically up to another datum is known as upward continuation. The transformation of a gravity anomaly computed at a point (say $Q(x_0, y_0, z_0 = 0)$) on one given surface (say mean sea level (msl) surface $z = 0$) to a point (say $P(x_0, y_0, z_0 = -h)$) on some higher flat surface (upward continued surface $z < 0$) is called upward continuation (Abera Alemu, 2020). The gravitational attraction per unit mass of an anomalous source body of mass *dm* at a mean sea level point $Q(x_0, y_0, z_0 = 0)$ and a distance *R* from a source point $Q(x, y, z)$ (Fig. 5.4) is given by:

$$dg = \frac{G\,dm}{R^2} = \frac{G\,dm}{(x - x_0)^2 + (y - y_0)^2 + (z - z_0 = 0)^2} \qquad (5.1)$$

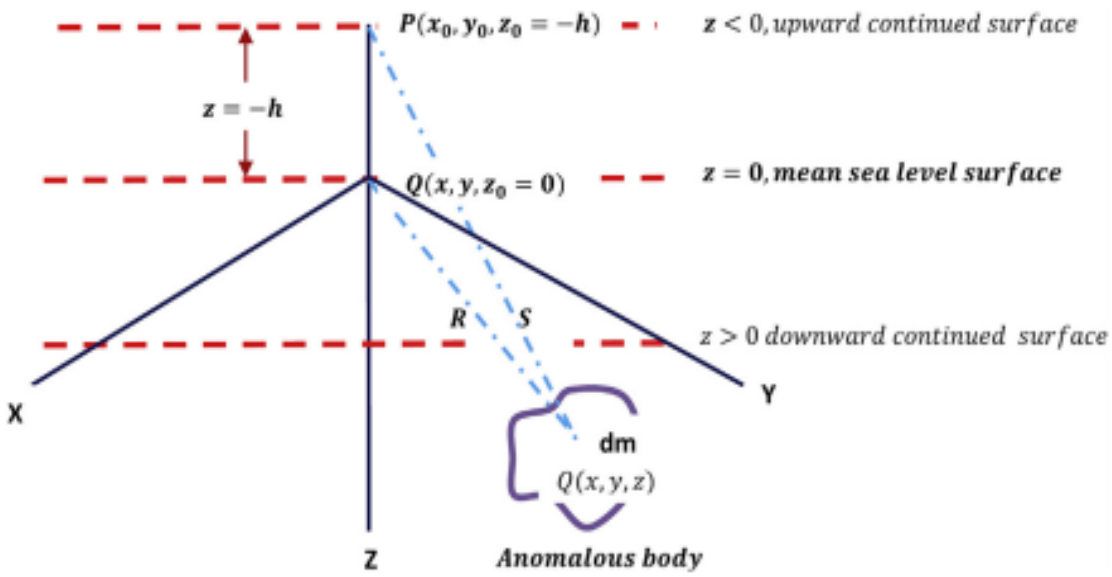

Figure 5.4 Pictorial representation of upward continuation technique in Cartesian coordinate system (modified from Abera Alemu, 2020)

The vertical component dg_z gives the gravity anomaly Δg_0 of a source at the msl surface point is:

$$dg_z = \Delta g_O = \frac{G\,dm}{R^2}\frac{z}{R} = G\,dm\,\frac{z}{R^3} = G\,dm\,\frac{z}{[(x - x_0)^2 + (y - y_0)^2 + (z)^2]^{3/2}} \qquad (5.2)$$

Similarly, the gravity anomaly Δg_P of the anomalous source at the upward continued surface point P is:

$$\Delta g_P = \frac{G\,dm}{S^2}\frac{z + h}{S} = G\,dm\,\frac{z + h}{S^3} = G\,dm\,\frac{z + h}{[(x - x_0)^2 + (y - y_0)^2 + (z + h)^2]^{3/2}} \qquad (5.3)$$

Upward continuation method simulates the anomaly as if the data has been obtained at that level. An upward continuation of a potential field to a height of h enables us to see anomaly sources at and below a depth of h/2 (Jacobsen, 1987). According to Hinze et al., (2013) an upward continuation is a smooth, low-wavenumber pass filter which enhances the anomalies from the broader, deeper sources at the expense of the shallow-sourced anomalies. It effectively attenuates noise without changing the physical significance of the data.

The upward continued gravity anomaly map or the regional anomaly map (Fig.5.5) is compiled by applying the upward continuation filter to the gridded complete Bouguer anomaly map using the Geosoft Oasis Montaj software (version 7.0). The map (Fig. 5.5) reflects the gravity effect of crustal masses buried at approximate depths varying from 5km up to the crust-mantle boundary depth. In this thesis work, this data enhancement technique has been employed to determine the gravity field variation caused by bodies buried at and below 5km depths (Section 5.1.3).

5.1.3 Regional gravity anomaly map

As explained in section 5.1.1 the complete Bouguer anomaly is the sum of the effects of features of long wave length, deep seated (regional anomaly) and short wave length, near surface (residual anomaly) components. Separation of both components is thus, compulsory to clearly see the effects of both deep seated and shallow seated anomalous sources contributing for the complete Bouguer anomaly generated. Although there are various methods of separation, an upward continuation method was used in this thesis work to approximate the regional anomaly using Geosoft Oasis Montaj software (version 7.0).

The regional gravity anomaly map (Fig. 5.5) of the study area is compiled by upward continuation of the gridded complete Bouguer gravity anomaly map (Fig. 5.3). Hopping to observe the effect of deep seated bodies (at and below 5km), the gridded CBA map (Fig. 5.3) is upward continued for 10km to compile the regional anomaly map (Fig. 5.5). Figure 5.5 provides an important insight in understanding the pattern of the regional gravity field of the study area.

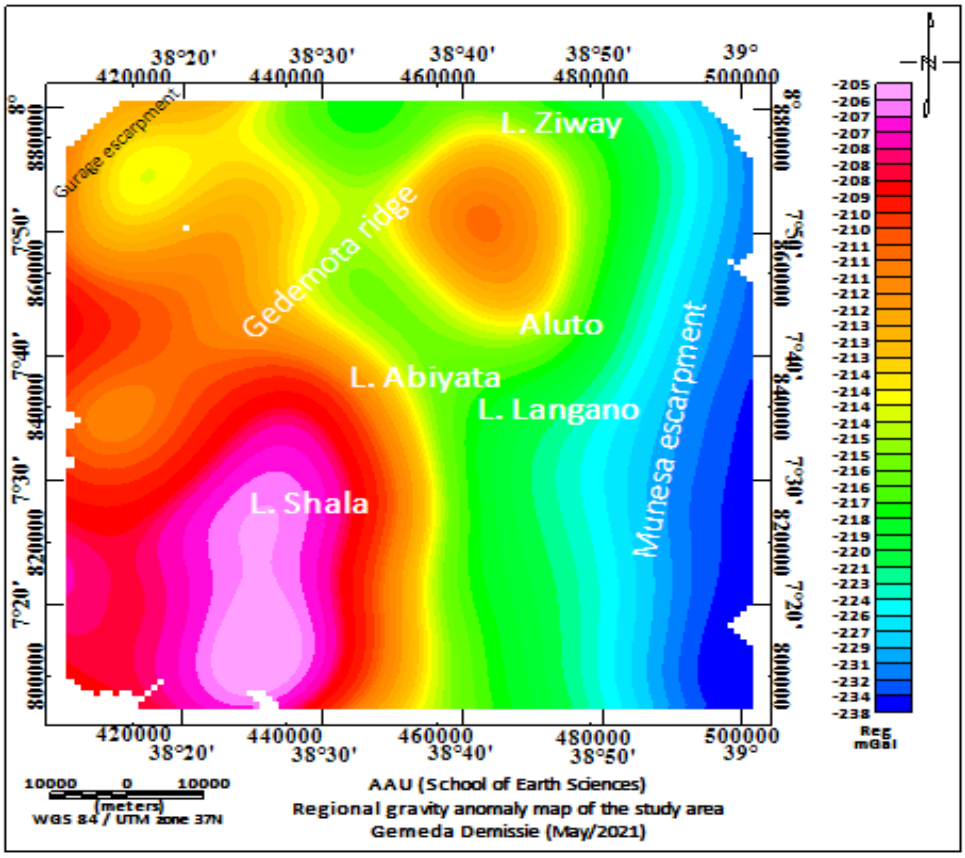

Figure 5.5 Regional Bouguer gravity anomaly maps of the Aluto-Langano geothermal field and its environs

Closely examining Figure 5.5 relatively low, intermediate and high regional gravity anomaly values are revealed. The Munesa escarpment is characterized by relatively low regional gravity anomaly. However, the Gurage escarpment which lies at the northwestern extreme of the study area is associated with relatively higher regional gravity anomaly as compared to the Munesa escarpment. The low regional gravity anomaly associated with the Munesa escarpment (Eastern border fault) could be interpreted to be the effect of voluminous deposits of low density Quaternary to Tertiary volcanic products which are composed of felsic lava and silicic pyroclastics observed on the geological map of the study area (Fig. 2.7). The relatively low regional gravity anomalies ranging from -221mGal to -238mGal observed over the study area could be interpreted as being the effect of deep seated bodies buried at depths greater than or equal to 5km. The intermediate regional anomalies ranging from -215mGal to -220mGal occur between the Munesa escarpment and the rift floor of the study area. The rift floor including the

Aluto volcano and the Shala caldera is associated with relatively high regional anomalies ranging from -216mGal to -205mGal.

The high regional gravity anomalies associated with the rift floor including the Aluto volcano and the Shala caldera could be interpreted as being the decrease in crustal thickness beneath the study area due to upwelling of denser materials closer to the surface.

5.1.4 Residual Bouguer gravity anomaly map

According to Dentith and Mudges (2014), Bouguer residual gravity anomaly can be obtained by subtracting the resultant upward continued data (regional Bouguer gravity anomaly) from the unfiltered data (complete Bouguer gravity anomaly). The residual gravity anomaly map (Fig. 5.6) of the Aluto-Langano geothermal field and its environs is compiled by substracting the gridded regional Bouguer gravity anomaly map (Fig.5.5) from the gridded CBA map (Fig. 5.3) using the Geosoft Oasis Montaj software (version 7.0). Figure 5.6 shows the effect of geologic bodies buried at depths less than 5km.

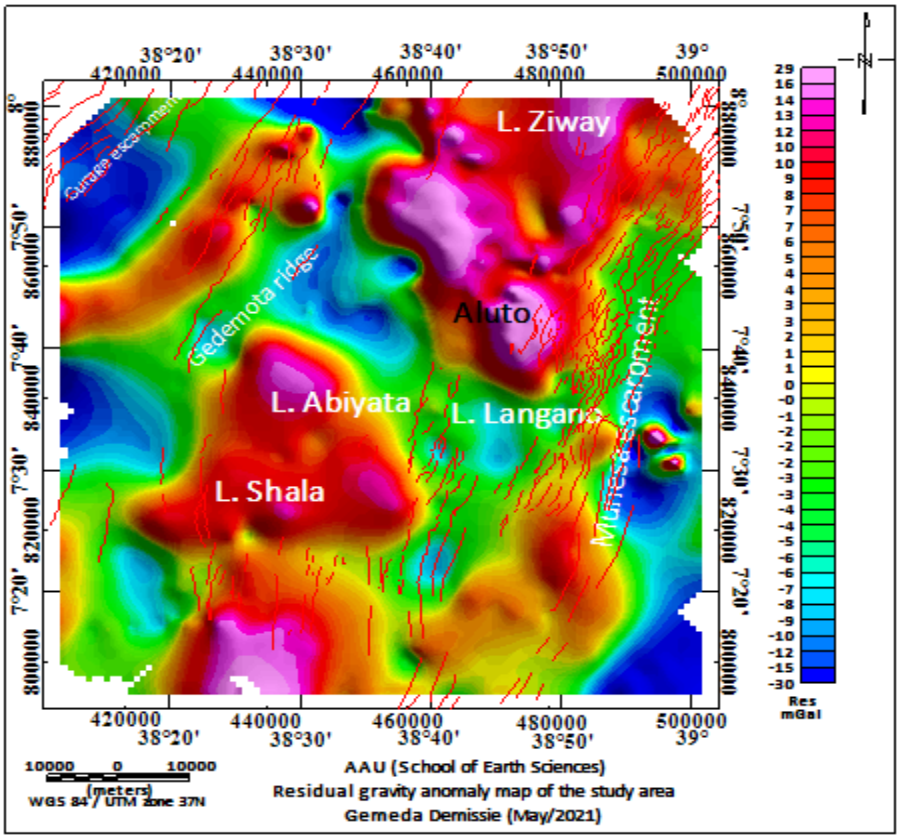

Figure 5.6 Residual gravity anomaly map of the study area. Where, smooth red lines are faults

The interpretation of the residual Bouguer gravity anomaly map (Fig. 5.6) in terms of geology is made in conjunction with the regional stratigraphy (Table 2.1), structural configuration (Fig. 2.2) and the simplified geological map (Fig. 2.7) of the study area. The compiled residual anomaly map (Fig. 5.6) reveals the distribution of negative and positive residual gravity anomalies ranging from -30mGal to 29mGal which are thought to arise from shallow subsurface (<5km) anomalous geologic source bodies. These local positive and negative residual gravity anomalies are related to denser intrusions and low density materials respectively.

The rift floor is characterized by several localized relatively positive residual anomalies (> 8mGal) aligned along the rift axis. Specifically, the peralkaline silicic volcanic centers of the Aluto volcano and the Shala caldera are characterized by positive gravity highs (> 10 mGal) (Fig. 5.6). The residual gravity maxima observed over the Aluto volcano and the Shala caldera are associated with the higher density materials supposed to exist beneath the Aluto volcano and the caldera (i.e. upward driven dense intrusions from the mantle to the crust by volcanic activity).

The NNE-SSW and NE-SW trending residual gravity anomaly maxima observed in Figure 5.6 show that the Aluto active volcanic center and the Shala caldera occur along the displacement lines of the WFB. These volcanic centers are thus underlain by higher density and hot magmatic intrusions (heat sources) and favor the possible occurrence of the geothermal system observed in the study area also manifested by fumaroles, hydrothermal alterations and hot springs.

The Munesa escarpment is characterized by relatively negative residual anomalies (< -6mGal) resulting from the lower density rocks mapped on the geologic map (Fig. 2.7). The geological map (Fig. 2.7) and field observations during geophysical data acquisition indicate that this escarpment is dominated by felsic lava flows and pyroclastic deposits (ignimbrite, welded and unwelded tuff units). Other possible cause of the negative residual gravity anomaly observed over the Munesa escarpment could be a reflection of its higher elevation (Fig. 5.1).

When we compare the regional gravity anomaly (Fig. 5.5) with the residual anomaly (Fig. 5.6), effects of the active zones of the WFB (Aluto and Shala volcanic complexes) are more pronounced on the residual gravity anomaly (Fig. 5.6). This indicates that the higher density intrusions occurring beneath the volcano-tectonically active zones are probably buried at shallower depths.

5.1.3 Horizontal derivative gravity map

Tilahun Mammo (2010) suggests that prior to modeling gravity data relevant information can be extracted from the gravity data itself using various data enhancement/filtering techniques. Among them horizontal derivative (HDR) is one that enables us to locate the boundaries of near surface geologic bodies of contrasting density (Blakely and Simpson, 1986). The horizontal derivative (HDR) is a mathematical anomaly enhancement method also known as horizontal gradient filter applied to an observed gravity anomaly (Δg) of preference at surface points (x, y) given by the mathematical formula:

$$HDR = H(x, y) = \sqrt{\left(\frac{\partial \Delta g}{\partial x}\right)^2 + \left(\frac{\partial \Delta g}{\partial y}\right)^2} \qquad (5.4)$$

Where, Δg is observed gravity anomaly of preference (i.e. Δg can be either Δg_B or Δg_{res} or Δg_R depending up on targeted depths of investigation), $\partial\Delta g/\partial x$ and $\partial\Delta g/\partial y$ are horizontal derivatives of the observed gravity anomaly of preference in the x and y directions respectively and H(x, y) is amplitude of the horizontal gradient computed at points (x, y) in the survey area.

In the present work since our targeted depth of interest is shallow anomalous body Δg_{res} is utilized. According to Abera Alemu (2020), the horizontal gradient maxima revealed by a HDR gravity map are useful in defining the lateral extent of anomalous source bodies such as sediment-filled valleys. Horizontal derivative maxima occur over the steepest parts of anomalies, and horizontal derivative minima over the flattest parts of anomalies. HDR works based on the principle that the maximum horizontal gradient is caused by a planar anomalous body tends to overlie the edge of the body and vertical discontinuities.

In this thesis work, the horizontal derivative (HDR) map (Fig. 5.7) is compiled by applying the horizontal gradient filter to the gridded residual gravity anomaly map (Fig. 5.6) in order to enhance and clearly demarcate the pattern of the tectonic relief of the study area. Gravity discontinuities in the HDR map (Fig. 5.7) are either structural or lithological contacts. Moreover, the HDR map (Fig. 5.7) reveals NE-SW, E-W and NNE-SSW oriented linear belts of positive, negative and intermediate horizontal derivative values. The lineated horizontal derivative maxima with steep slopes revealed by the map indicate boundaries of major geological features that could be interpreted as fault and/or lithological units in horizontal contacts at shallow depth.

In conjunction with the simplified geological map (Fig. 2.7) and structural configuration (Fig. 2.3) of the study area, the horizontal derivative map (Fig. 5.7) can be interpreted as follows: The eastern part of the study area is clearly reflected by continuous positive and negative horizontal gradients being correlated with a structural discontinuity, mainly the Munesa boarder fault; The northwestern part of the study area is also highlighted as NE-SW trending geological structures being associated with Gurage border fault. The Gedemota ridge which lies north of Lake Abiyata and southwest of Lake Ziway is marked by positive horizontal gradient indicating that it forms a linear arcuate structure. The rift floor including the Aluto volcano and the Shala caldera is characterized by negative and positive gradients which appear to be the effect of Quaternary faults and/or fractures. Hence, we can infer that the alignment of thermal springs and geothermal prospect zone follows these Quaternary faults that could also be verified by Engdawork Admasu and Selamawit Worku (2015).

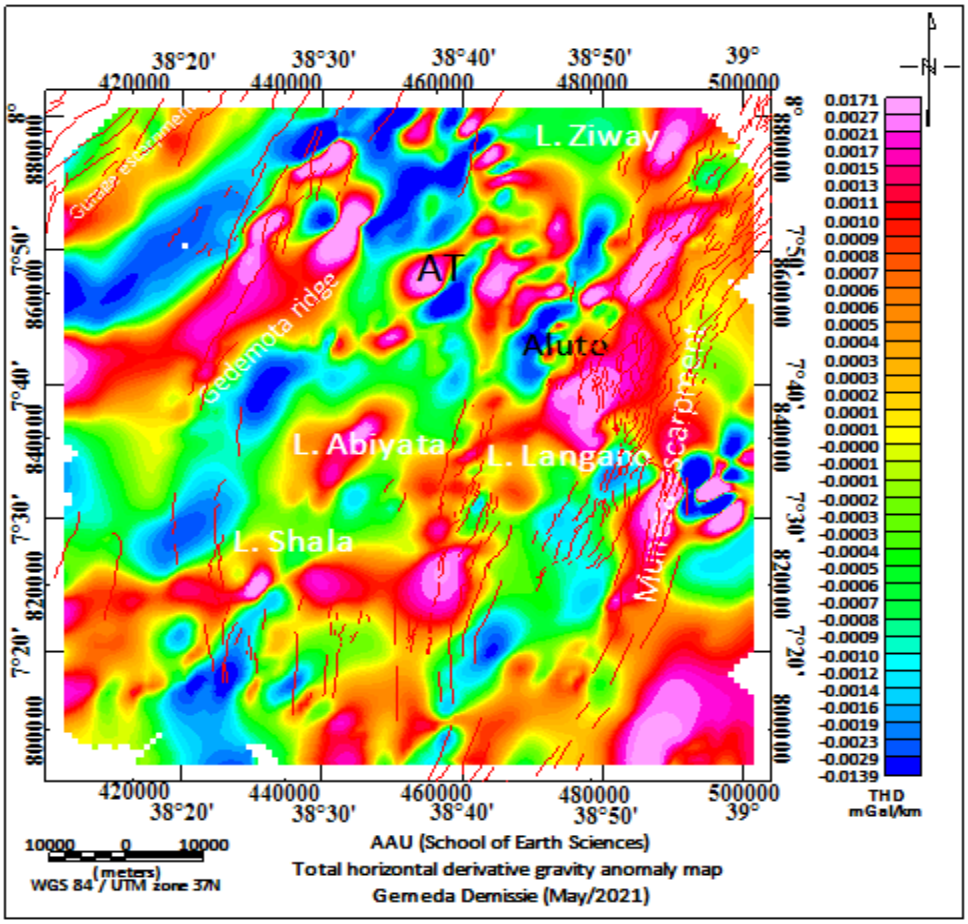

Figure 5.7 Total horizontal derivative gravity anomaly map rotated 135^0 ccw. Where, AT is Adami Tulu and smooth red lines are faults

5.1.4 Analytical signal gravity map

Dentith and Mudges (2014) explain analytical signal (AS) or total derivative as a powerful technique of interpretation in potential field data. According to Dentith and Mudges (2014), the AS enhances the effect of shallow seated source bodies at the expense of the effect of deep seated bodies.

The analytic signal of an observed gravity anomaly (Δg) of preference produced by a 3D anomalous source is given by:

$$A(x, y) = \sqrt{\left(\frac{\partial \Delta g}{\partial x}\right)^2 + \left(\frac{\partial \Delta g}{\partial y}\right)^2 + \left(\frac{\partial \Delta g}{\partial z}\right)^2} \qquad (5.5)$$

Where $A(x, y)$ is amplitude of the analytic signal value computed at point (x, y), Δg is the observed gravity anomaly of preference at point (x, y) and $\partial\Delta g/\partial x$, $\partial\Delta g/\partial y$ are the two horizontal derivatives and $\partial\Delta g/\partial z$ is the vertical derivative of the observed gravity anomaly of preference. The observed gravity anomaly (Δg) of preference can be taken to be regional gravity anomaly (Δg_R) if the anomalous source of interest has a deep origin and it can be taken to be residual gravity anomaly (Δg_{res}) if the anomalous source of interest has shallow origin.

In the present work analytical signal gravity map (Fig. 5.8) is generated by applying the analytical signal filter to the gridded residual Bouguer gravity anomaly using the Geosoft Oasis Montaj (version 7.0).

The compiled analytical signal map (Fig. 5.8) reveals the anomaly texture and highlights the discontinuities (the edge of source bodies and geologic contacts). HDR map (Fig. 5.7) is not intuitive because it does not incorporate the vertical derivative whereas the analytical signal map (Fig. 5.8) is often effective at highlighting geologically meaningful anomalous body buried at depths.

The purpose of compiling AS map (Fig. 5.8) is to make the HDR map (Fig. 5.7) more informative through capturing gradients in all directions and further enhancing detection of geologic boundaries and structures. The discontinuity in the AS gravity map is highly correlated with the geological boundaries (Fig. 2.7).

Therefore, interpretation of the AS map (Fig. 5.8) has been made in conjunction with the geological map (Fig. 2.7) of the study area. The maximum gradient in the AS map (Fig. 5.8) reveals the source body and geologic contacts. In the AS map (Fig. 5.8) the effect of shallow seated bodies is enhanced. Moreover, the analytical signal map reveals that the maximum analytical signal values are generally coincident with the residual gravity anomaly peaks and with known structural and lithological features/contacts over the study area. These positive analytical signal peaks are generally aligned in NE-SW and NNE-SSW direction which appears to act as a geothermal reservoir for the study area.

The Aluto volcanic complex is characterized by a cumulate of maximum value in the analytical signal map (Fig. 5.8). This could be due to the existence of higher density materials beneath the Aluto volcanic complex. In this regard, the AS map (Fig 5.8) reasonably agrees with the geological map (Fig. 2.7) of the study area as the lithological discontinuities are clearly reflected by gravity signal discontinuities. The lacustrine sediments extensively cover the largest portion of the geological map of the study area. And also, the area covered by this lithology is characterized by low values in the AS (Fig. 5.8) whereas the volcanic rocks both in the rift floor and its flanks are characterized by high gradients.

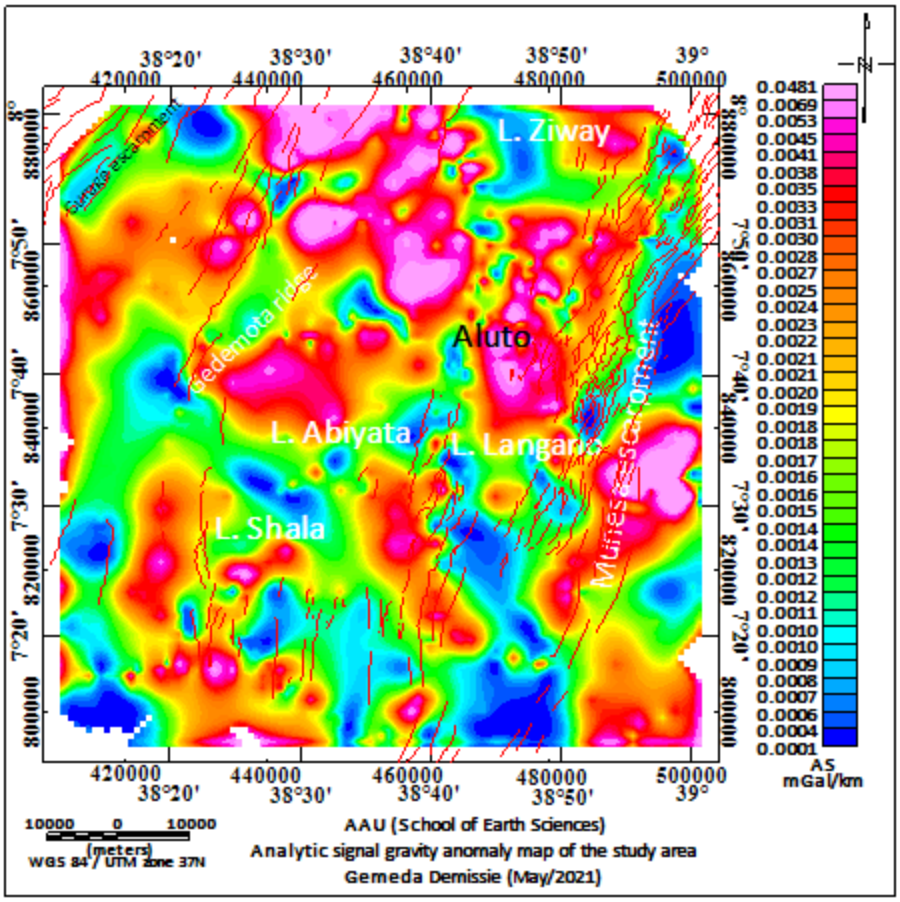

Figure 5.8 Gravity analytic signal map of the study area. Where, smooth red lines are determined faults

5.1.5 Tilt derivative gravity map

The tilt derivative and its total horizontal derivative are useful for mapping shallow basement structures and mineral exploration targets (Miller and Singh, 1994). According to Putri et al., (2019), edge detection in gravity data is a common technique of interpretation where faults and/or fractures with a significant density contrast can be detected. Hence, adequate information on edges of structural bodies can be obtained by a potential field data enhancement/filtering technique called tilt derivative (TDR). The TDR normalizes the first vertical derivative (VDR $= \frac{\partial \Delta g}{\partial z}$) by the total horizontal derivative (THDR $= \sqrt{(\frac{\partial \Delta g}{\partial x})^2 + (\frac{\partial \Delta g}{\partial y})^2}$) and uses the zero-point (zero-crossing) location to approximate the edge of the causative geological bodies (Miller and Singh, 1994). The TDR is mathematically expressed as:

$$TDR = \arctan\left(\frac{VDR}{THDR}\right) \quad (5.6a)$$

$$TDR = \arctan \frac{\frac{\partial \Delta g}{\partial z}}{\sqrt{\left(\frac{\partial \Delta g}{\partial x}\right)^2 + \left(\frac{\partial \Delta g}{\partial y}\right)^2}} \quad (5.6b)$$

Where, VDR=vertical derivative, THDR=total horizontal derivative, TDR = Tilt derivative (Miller and Singh, 1994).

TDR value is positive over source bodies, zero for the edge next to the source and negative outside source zones. The edge of the source can be fault, joint, rock density contrast, etc. (Putri et al., 2019).

The tilt derivative map (Fig. 5.9) of the study area is compiled by applying a tilt derivative filter to the gridded gravity analytical signal map (Fig. 5.8) using Geosoft Oasis Montaj software (version 7.0). Figure 5.9 reveals more detailed structural contacts/boundaries than the analytic signal map (Fig. 5.8). Thus, the study area is characterized by a set of numerous faults oriented in the NNE-SSW, NE-SW and NW-SE directions being coincident with the general structural setup (Fig. 2.3) of the study area. All these structures are indicated by red smooth lines on the TDR map (Fig. 5.9).

Moreover, the TDR map (Fig. 5.9) is more detail than the residual map (Fig. 5.6) and the AS map (Fig. 5.8) as the former enhances both short and long wavelength anomalies simultaneously. The difficulty in HDR (Fig. 5.7) and AS (Fig. 5.8) gravity maps is to identify the lithological and structural discontinuity at the same time which appears to be additional advantage in TDR technique of interpretation (Fig. 5.9).

The legend in Figure 5.9 provided by the color scale assists to identify the boundary (edge) of source bodies in such a way that the pale pink to red, yellow to dark-yellow and green to blue-black colors represents the source body, edge and the outside source bodies respectively.

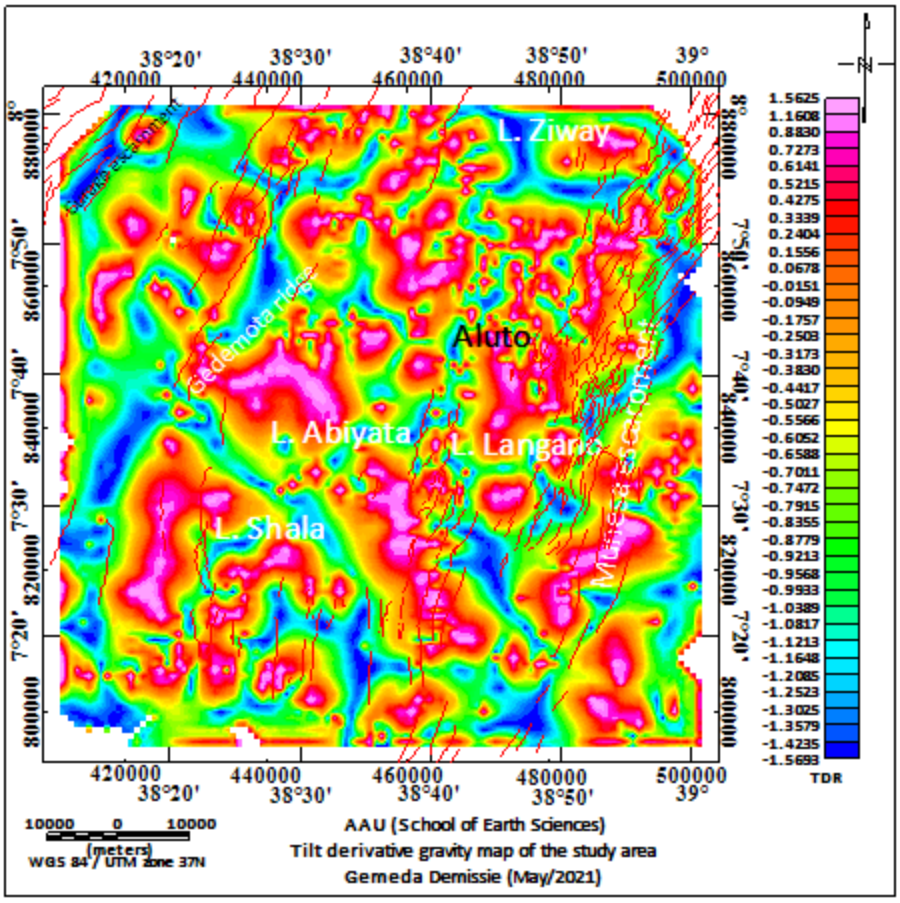

Figure 5.9 Gravity tilt derivative map of the study area. Where, smooth red lines are faults

5.1.6 Euler Deconvolution gravity map

According to Thompson (1982), Euler deconvolution (ED) is a mathematically established procedure used to estimate the source depth, nature and location of causative bodies beneath the surface of the Earth. That means, the ED is an established mathematical procedure based on the rate of change in the gravity anomaly field with distance from the source that is employed to estimate the **depth, location and nature** (3D, 2D or 1D nature) of a buried anomalous source(s). The objective of Euler deconvolution method is to produce one or more maps that display the locations and depths of the anomalous source bodies that generate the gravity anomalies of preference in 2D grid (Abera Alemu, 2020). And also, the Euler deconvolution method enables a 3D geologic interpretation of gravity anomalies by delineating gravimetric boundaries and calculating depths of anomalous sources.

The Euler deconvolution method can be applied to profile data or gridded map data. According to Abera Alemu (2020), for 3D anomalous sources buried at point $P(x_0, y_0, z_0)$, the Euler

deconvolution (Euler's homogeneity equation) at the surface point $Q(x, y, z)$ is mathematically expressed as:

$$(x - x_0)\frac{\partial \Delta g}{\partial x} + (y - y_0)\frac{\partial \Delta g}{\partial y} + (z - z_0)\frac{\partial \Delta g}{\partial z} = N(\Delta g - \beta) \quad (5.7)$$

Where, (x_0, y_0, z_0) is the position (location (x_0, y_0) and depth z_0) of the anomalous source body whose gravity anomaly Δg is computed at point $Q(x, y, z)$, β is the regional value of the gravity anomaly and N is Euler's structural index (SI) which characterizes degree of homogeneity of the anomalous source body defined as the fall of rate of the anomaly with distance from the source. The horizontal derivatives ($\partial \Delta g/\partial x$ and $\partial \Delta g/\partial y$), the vertical derivative ($\partial \Delta g/\partial z$), the regional value of the gravity anomaly β and structural index (SI) value assigned to the source body are used to compute the source locations (x_0, y_0, z_0) by solving a system of linear equations generated by Eq. (5.7) by the least squares adjustment method.

Table 5.1 gravity and magnetic structural index for different source geometries (Reynolds, 1997)

Geological model	No of infinite dimension	Magnetic SI	Gravity SI
Sphere	0	3	2
Pipe	1 (Z)	2	1
Horizontal cylinder	1 (X or Y)	2	1
Dyke	2 (Z and X or Y)	1	0
Sill	2 (X and Y)	1	0
Contact	3 (X, Y and Z)	0	NA

Structural index (SI) specification permits the equation to be solved for specific source location of specific field (Table 5.1). Choosing SI should be done using prior knowledge of source geometry. ED outlines different geologic structures generating the residual and regional anomalies in both gravity and magnetic surveys (Table 5.1).

Depth estimation for various anomaly source bodies of the Aluto-Langano geothermal field and its environs is made using the ED technique. The ED maps (Fig. 5.10 and Fig. 5.11) are compiled by applying a standard 3D Euler deconvolution filter to the gridded residual gravity map (Fig. 5.6) using the Geosoft Oasis Montaj software (version 7.0). Figure 5.10 and 5.11 reveal the spatial distribution (longitude, latitude), nature and depth of the causative bodies within the study area.

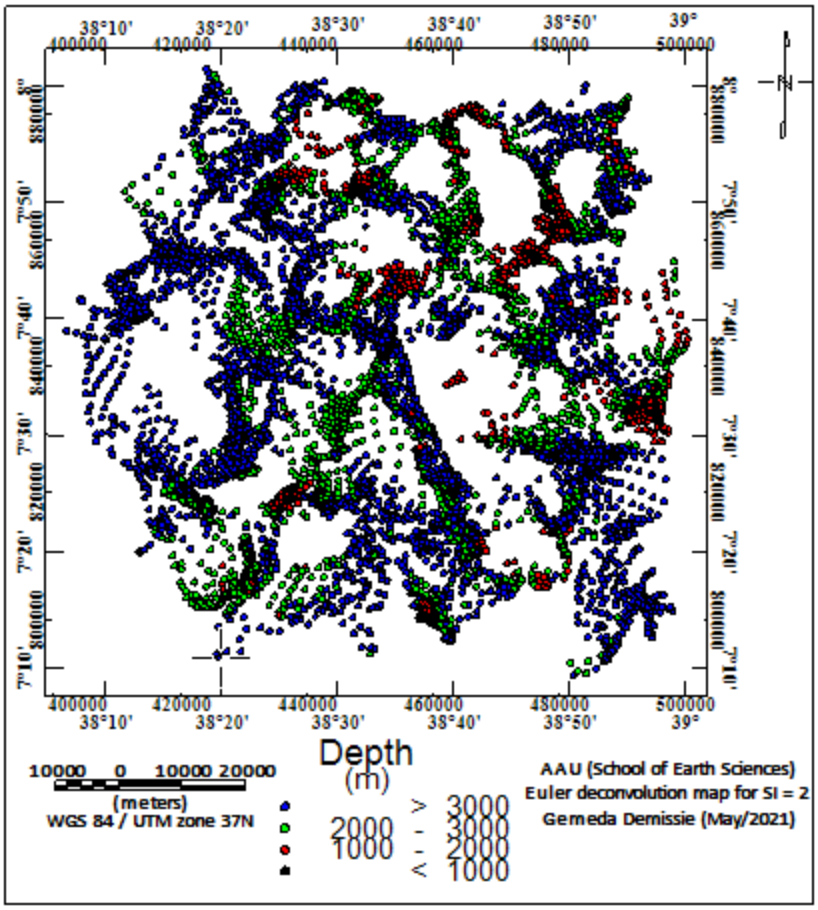

Figure 5.10 Euler deconvolution map for SI = 2 of the Aluto-Langano geothermal field and its environs

The optimal structural indices SI = 2 and SI = 0.5 are selected by a visual inspection of the maps until the best clustering of solutions is obtained. The structural indices SI = 2 and SI = 0.5 represent sphere and contacts respectively in the case of gravity.

Figure 5.10 shows the depth solutions of spherical bodies buried at different depths marked by different colored symbols plotted on the map. There are many solutions for 3D source bodies buried at depths greater than 3km (blue color) all over the study area. The map (Fig. 5.10) shows that the study area is dominated by 3D geologic bodies buried at depths greater than 3km. The map also shows occurrence of 3D geologic bodies buried at depths ranging from 2km to 3 km (pale green) beneath the Aluto volcano and the Shala caldera. The occurrences of 3D bodies buried at depths ranging from 2km to 3 km (pale green) are also evident beneath both the Munesa escarpment and Gurage escarpment. Figure 5.10 thus reveals a good evidence for the occurrence of a magma chamber (heat source) at shallower depths (2km-3km) beneath the Aluto

and Shala volcanic complexes. Figure 5.10 also shows 3D bodies occurring at a depth range of 1km to 2km (red color) which reveal a clear evidence for the existence of a magma chamber (heat source) at shallower depths beneath the Aluto volcano in consistent with drilling data (Abera Alemu, 1992). 3D bodies occurring at depths <1km (black color) also exist in the vicinities of the Aluto volcano, Shala caldera and between Lake Abiyata and Lake Langano.

The ED map (Fig. 5.11) compiled for a structural index of 0.5 show depth solutions for contacts/boundaries occurring beneath the study area. The map reveals existence of linear source bodies (contacts) occurring at depths greater than 3km (blue color), 2km to 3 km (yellow color), 1km to 2 km (red color) and <1km (black color) beneath the study area. Therefore, the study area is dominated by linear bodies occurring at variable depths with their distribution having specific orientations on a semi-regional scale. The Munesa escarpment, Gurage escarpment, the Gedemota ridge, the corridor between Lake Abiyata and Lake Langano and the minor faults/contacts are clearly marked on the ED map (Fig. 5.11). However, the Aluto and the Shala caldera are not marked by existence of linear structures/faults. These phenomena may be due to the existence of a shallow magma chamber associated with the volcanic complexes where the rocks are in ductile (semi ductile) state and do not tend to undergo brittle deformation.

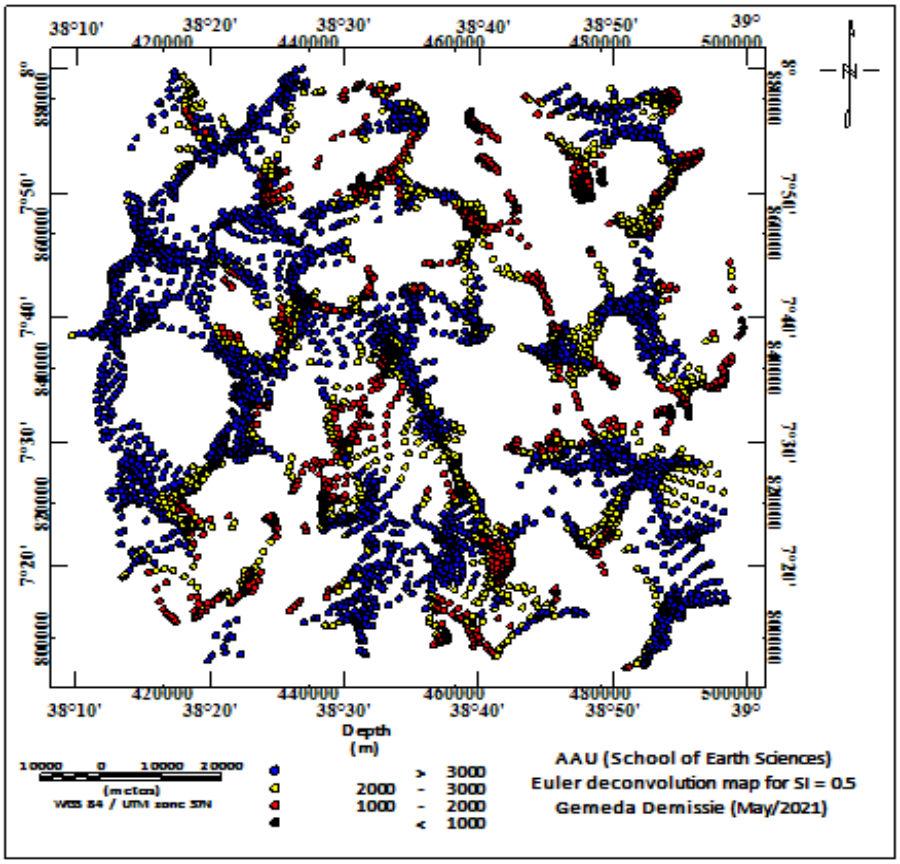

Figure 5.11 Gravity Euler deconvolution map of the study area for SI = 0.5

5.2 Magnetic data results, analysis and interpretations

The objective of magnetic surveying is to identify and characterize the Earth's crust that is associated with anomalous regions by assisting and supporting the interpretation of the gravity data. Since the study area is found within the CMER which is located near the magnetic equator the interpretation of magnetic data is claimed to be ambiguous due to bipolar nature of the Earth's magnetic field. Thus, the magnetic anomaly maps considered in this thesis work are compiled by applying a reduction to pole (RTP) filter to the observed total magnetic anomaly in order to avoid the ambiguity in the interpretation of the data. Consequently, upward continuation, analytical signal, tilt derivative and Euler deconvolution filters are applied to the pole reduced total magnetic anomaly for further qualitative and quantitative interpretation of the magnetic data considered in this study.

5.2.1 Reduction to the pole of the magnetic anomalies

Reduction to the pole (RTP) is a technique that converts magnetic anomaly to symmetrical pattern which would have been observed with vertical magnetization. It reduces dipole filed of equatorial region anomalies to monopole field by translating the magnetic anomaly directly above the causative body as gravity (Yaogauo and Oldenberg, 2001).

Reduction to the pole has an amplitude component and a phase component. When reducing to the pole from equatorial latitudes, North-South features can blow-up due to the strong amplitude correction that is applied when the declination + wavenumber direction is ð/2 (i.e. a magnetic East-West wavenumber). By applying higher latitude for the amplitude correction alone, this problem can be reduced or eliminated at the expense of under-correcting the amplitudes of North-South features.

An amplitude inclination of 90 causes only the phase component to be applied to the data (no amplitude correction), and a value of 0 (zero) causes phase and amplitude components to be applied over the entire range. The default amplitude inclination value is 20 degrees in the Northern Hemisphere. In the Southern Hemisphere, the amplitude inclination value is negative and the default is –20 degrees.

RTP operator is expressed as:

$$L(\theta) = \frac{1}{[\sin(I) + i\cos(I)\cos(D - \theta)^2]} \qquad (5.8)$$

Where, θ is the wave number direction, D=Declination and I is the inclination.

The reduction to pole filtering operation of this work has been made using an average inclination and declination of -1.94^0 and $+1.4^0$ as well as an amplitude correction inclination of $+20^0$. Accordingly, the regional magnetic anomaly map, the residual magnetic anomaly map, the analytical signal map, the tilt derivative map and the Euler deconvolution map are compiled for a further interpretation of the RTP magnetic data.

5.2.2 Total magnetic field intensity map

The total magnetic field intensity (TMI) map (Fig. 5.12) is compiled after correcting all the magnetic data points for diurnal variations in earth's magnetic field. The map is supposed to

show the combined effect of rock magnetization and dipole field of the Aluto-Langano geothermal field and its environs. The total magnetic field intensity values in the study area vary from a minimum of 34526nT to a maximum of 36325nT.

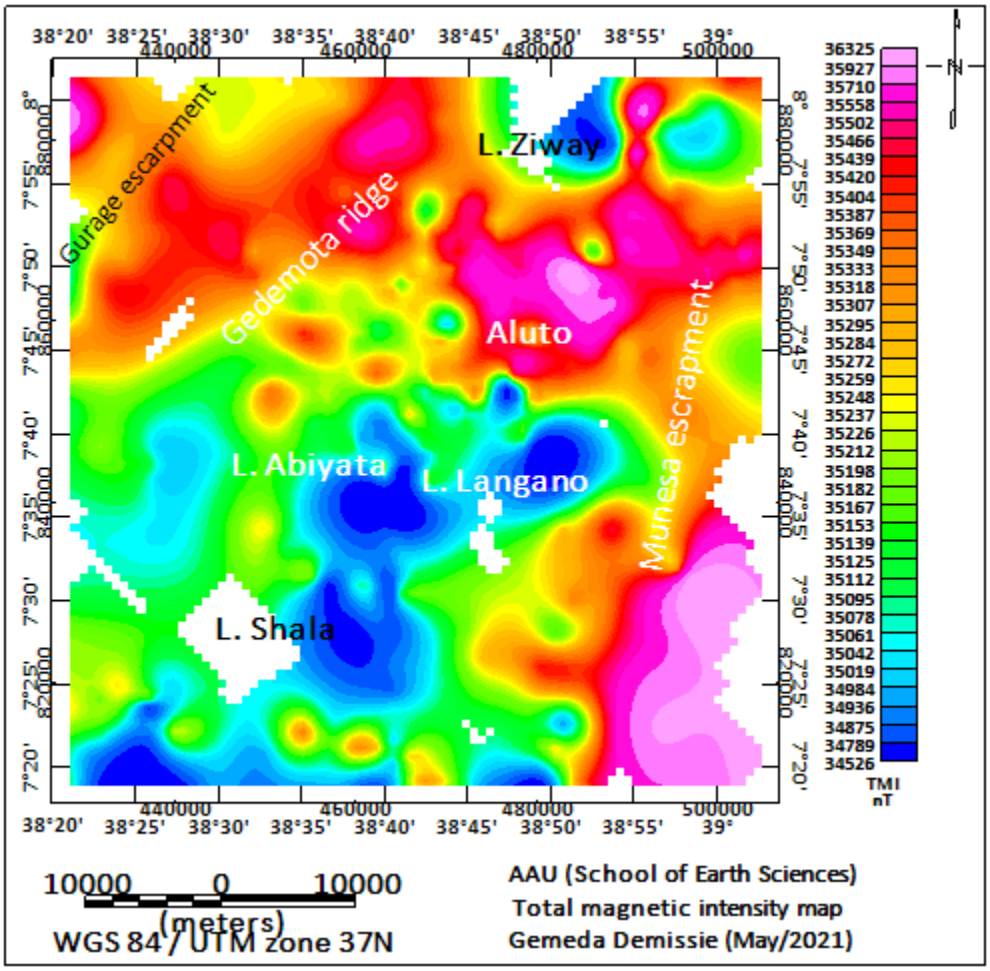

Figure 5.12 Total magnetic intensity map of the study area

The maximum total magnetic field intensity values in the study area occur at the locations of the Aluto volcanic complex, the Munesa escarpment and the Gurage escarpment. Whereas, the minimum total magnetic field intensity values occur at the locations of the Lake Ziway, the Lake Abiyata and Lake Langano.

From a geologic point of view the total magnetic field intensity map is not viable for a further interpretation in terms of geology as geological interpretation of magnetic data heavily depends on magnetization of rocks (rock magnetism) treated in the sections that follow here.

5.2.3 Total magnetic field anomaly map

The total magnetic anomaly (TMA) map (Fig. 5.13) of the study area is generated by removing the dipole field from the total magnetic intensity by IGRF correction using Geosoft Oasis Montaj software (version 7.0). The IGRF value of the study area is the value automatically obtained by Geosoft Oasis Montaj software (version 7.0). The total magnetic anomaly shows the effect of both deep seated and shallow sources.

It is determined that interpretation of the total magnetic anomaly in terms of geology at equatorial areas (low magnetic latitudes) does not give results matching the geological units of interest due to the dipolar nature of the total magnetic field (Section 5.2.1). Hence, for a further interpretation of the total magnetic anomaly in terms of geology it is imperative to apply the reduced to pole (RTP) filter to the gridded total magnetic anomaly map (Fig. 5.13).

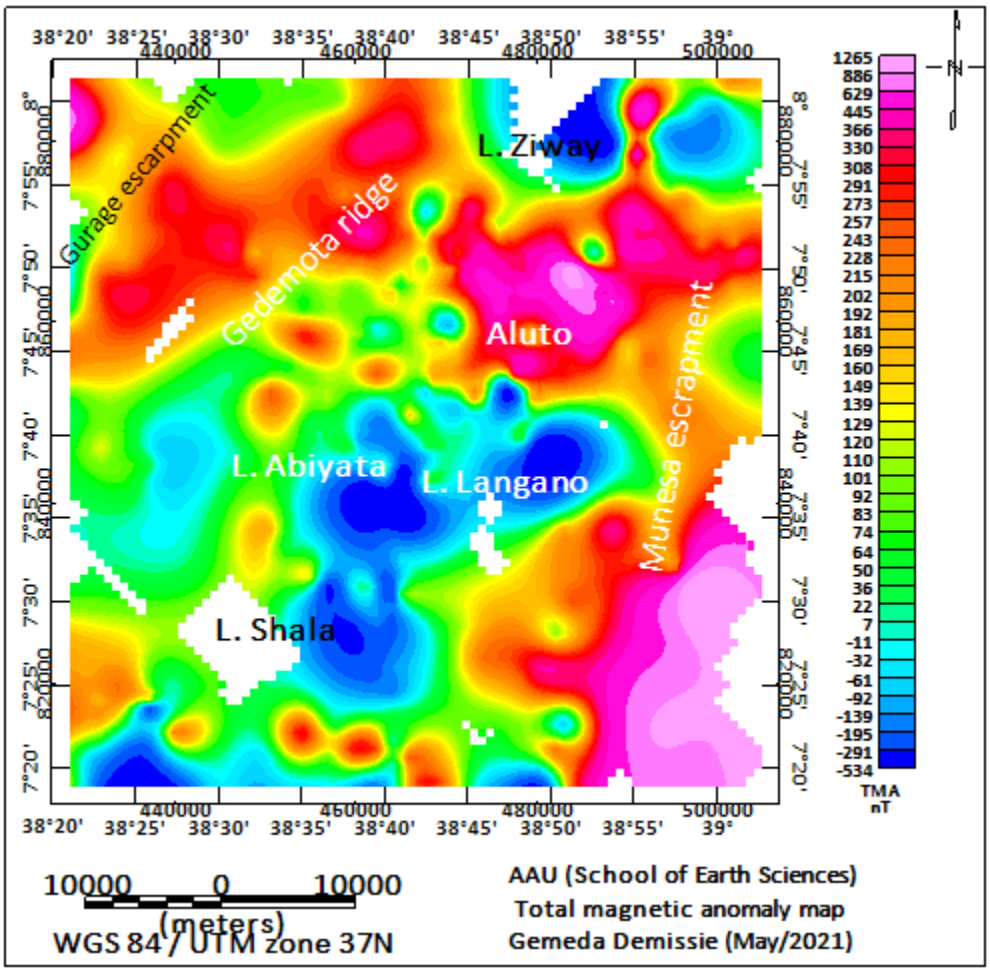

Figure 5.13 Total magnetic anomaly map of the study area

Interpretation of the RTP total magnetic field anomaly in terms of geology is discussed in more detail in the sections that follow here.

5.2.4 Pole reduced total magnetic field anomaly map

The RTP total magnetic field anomaly map (Fig. 5.14) is compiled by applying the RTP filter to the gridded TMA map (Fig. 5.13). The RTP total magnetic field anomaly values in the study area vary from a minimum of -886nT to a maximum of 290nT.

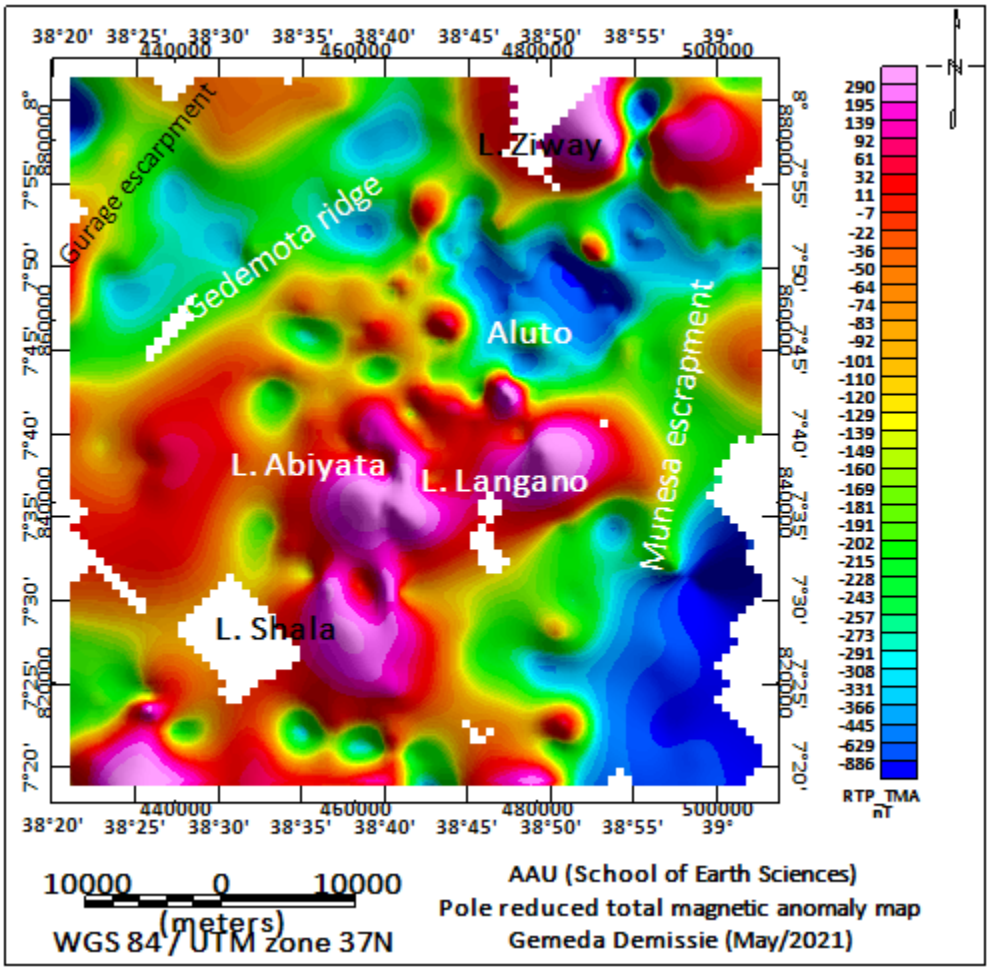

Figure 5.14 Pole reduced total magnetic anomaly map of the area

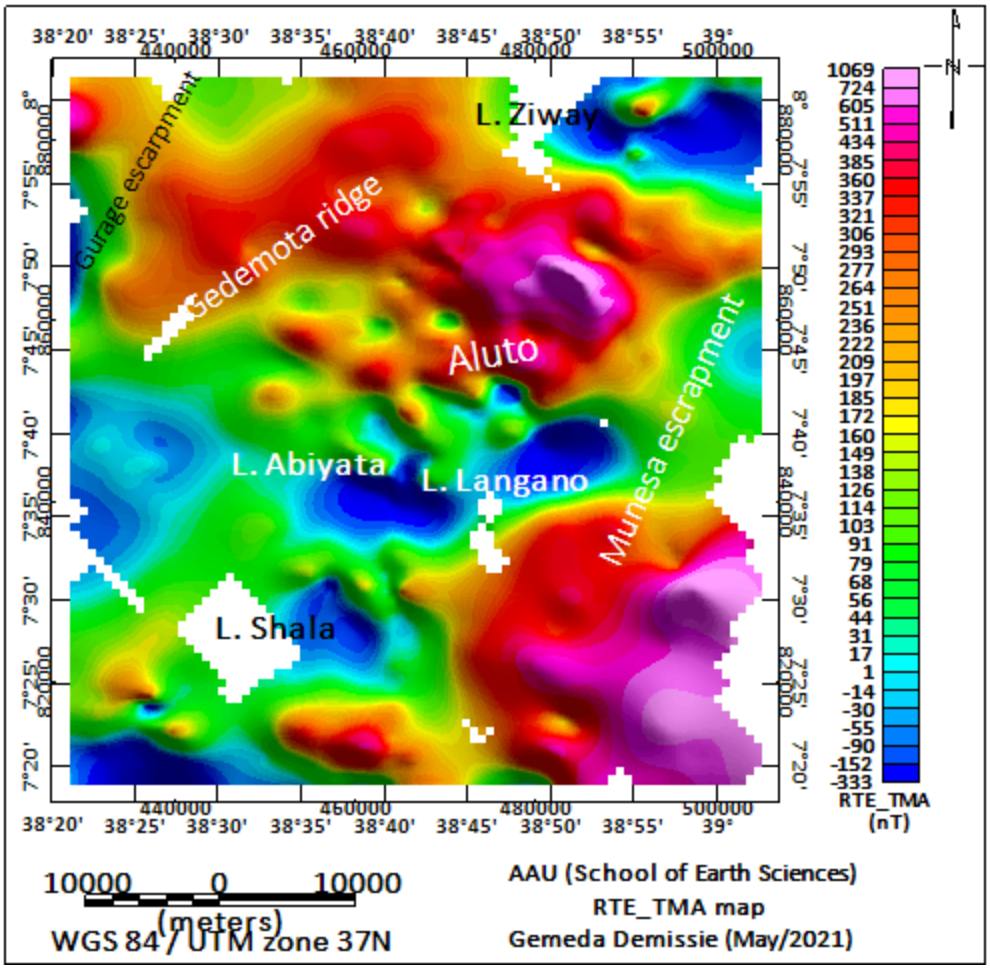

Reduce to equator total magnetic anomaly map

The maximum RTP total magnetic field anomaly values in the study area occur at the locations of the Lake Ziway, the Lake Abiyata, Lake Langano, south of the Lake Shala and western part of the study area. Whereas, the minimum values occur at the locations of the Aluto volcanic complex and east of Lake Shala. The Munesa and the Gurage escarpments are characterized by intermediate RTP total magnetic field anomaly value.

Since the RTP total magnetic anomaly map (Fig.5.14) is the sum effect of both deep and shallow sources it is appropriate to isolate the effect of deep seated bodies from those of the shallow sources by applying appropriate filtering techniques. In order to isolate the regional from the residual anomalies the upward continuation filter with a cut off wavelength 10km is applied to the gridded RTP total magnetic anomaly map (Fig. 5.13)

5.2.5 The RTP regional magnetic anomaly map

The RTP regional magnetic anomaly map (Fig. 5.15) is compiled by applying the upward continuation filter with cutoff wavelength of 10km to the gridded RTP total magnetic anomaly map (Fig. 5.13) using Geosoft Oasis Montaj software (version 7.0). Figure 5.15 provides an important understanding in the pattern of the RTP regional magnetic field of the study area. Thus, Figure 5.15 shows existence of linear low, intermediate and high RTP regional magnetic anomalies varying from a minimum of -624nT to a maximum of -28nT seated at and below 5km. The eastern part of the study area including the Munesa escarpment is associated with NNE-SSW oriented/trending low RTP regional magnetic anomaly responses. However, the Gurage escarpment which lies at the northwestern extreme of the study area is associated with relatively higher RTP regional magnetic anomaly as compared to the Munesa escarpment. The low RTP regional magnetic anomaly associated with the Munesa escarpment (Eastern border fault) could be interpreted to be the effect of voluminous deposits of low magnetic susceptibility Quaternary to Tertiary volcanic products which are composed of felsic lava and silicic pyroclastics observed on the geological map of the study area (Fig. 2.7). The relatively low RTP regional magnetic anomalies ranging from -624nT to -140nT observed over the study area could be interpreted as being the effect of deep seated bodies buried at depths greater than or equal to 5km. The intermediate RTP regional magnetic anomalies ranging from -135nT to -80nT occur at a locations of eastern margin of Lake Langano, eastern margin of Lake Shala, northern margin of Lake Abiyata and northwestern part of the study area. The areas corresponding to Lake Shala, Lake Langano, Lake Abiyata and Lake Ziway are characterized by relatively high RTP regional magnetic anomalies ranging from -76nT to -28nT.

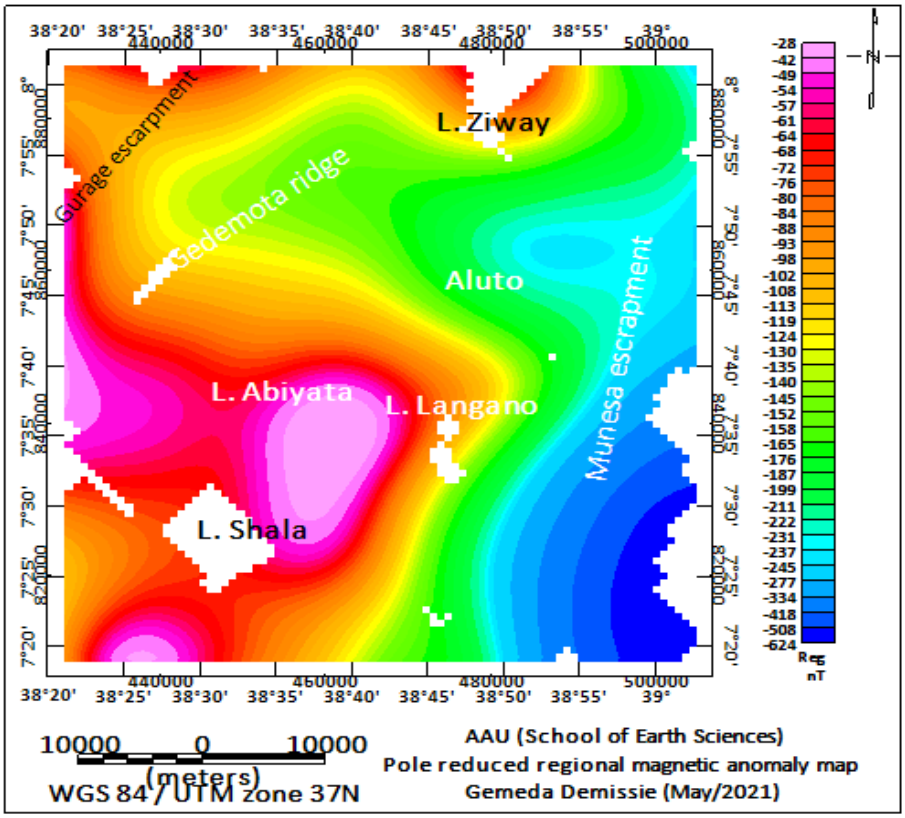

Figure 5.15 RTP regional magnetic anomaly map of the study area

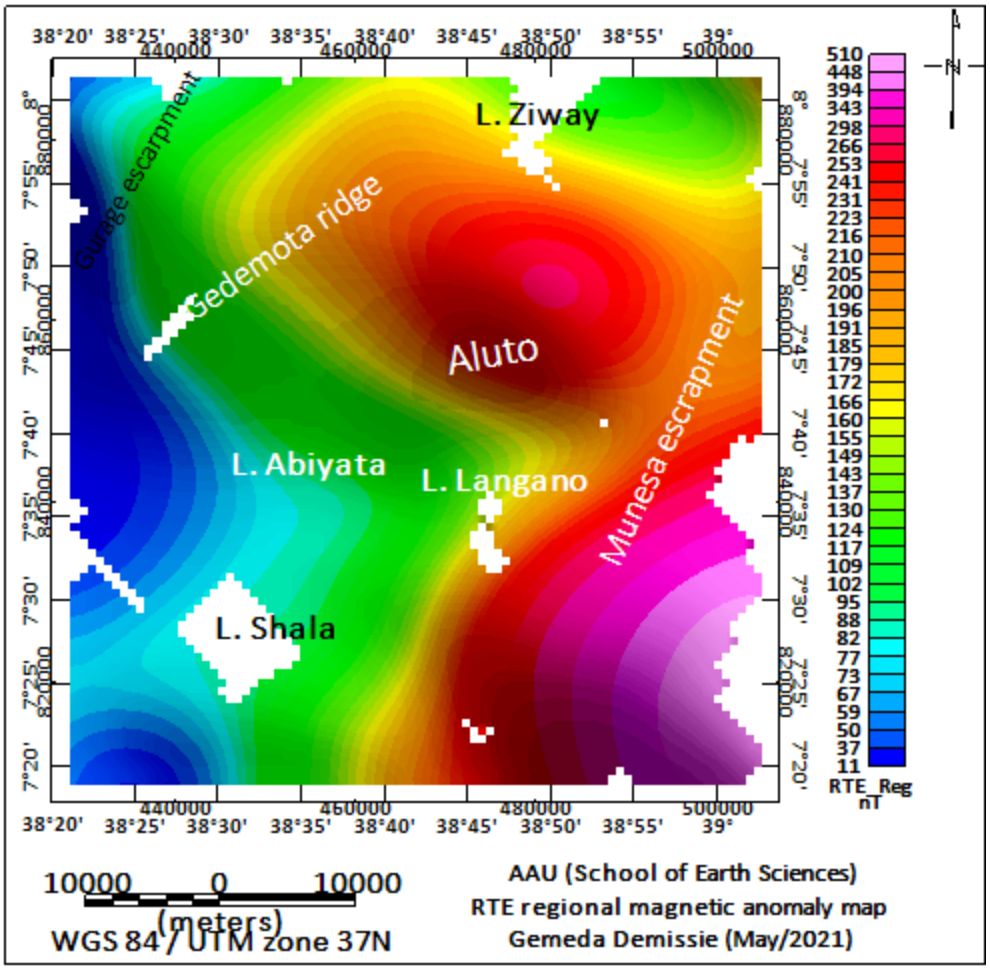

5.2.6 The RTP residual magnetic anomaly map

The RTP residual magnetic anomaly map (Fig. 5.16) of this study is compiled by subtracting the gridded RTP regional magnetic anomaly map (Fig. 5.15) from the gridded RTP total magnetic anomaly map (Fig. 5.14) using Geosoft Oasis Montaj software (version 7.0). The interpretation of the RTP residual magnetic anomaly map (Fig. 5.16) in terms of geology is made in conjunction with the simplified geological map (Fig. 2.7) of the study area. Figure 5.16 shows that the RTP residual magnetic anomaly values in the study area vary from a minimum of -860nT to a maximum of 657nT being primarily due to the effect of variation in geology and buried intrusions/shallow magma chambers at shallow depths (<5km). These local positive and negative RTP residual magnetic anomalies are related to low and high magnetic susceptibility materials respectively. The northwestern and southeastern parts of the study area including the Aluto volcano and the Shala caldera are associated with low RTP residual magnetic anomalies

(<-24nT). Specifically, the peralkaline silicic volcanic centers of the Aluto volcano is characterized by negative magnetic lows (<-201nT) (Fig. 5.16). The residual magnetic minima observed over the Aluto volcano are associated with the low susceptibility values of the volcanic materials as a result of heat treatment by the underlying magma chamber (i.e. upward driven hot intrusions from the mantle to the crust by volcanic activity). This volcanic center is thus underlain by low magnetic susceptibility and hot magmatic intrusions (heat sources) that favors the possible occurrence of the geothermal system observed in the study area which is verified also by surface geothermal manifestations (fumaroles, hydrothermal alterations and hot springs).

The zones corresponding to Lake Langano, Lake Abiyata, Lake Ziway and the Munesa escarpment are associated with high residual magnetic anomalies. The high residual magnetic anomaly zones coinciding with the locations of Lake Ziway and its flanking areas including Lake Abiyata and Lake Langano and the flanking areas are attributed to thick accumulation lacustrine sediments likely derived from the surrounding volcanic units (Fig. 2.7) and having high magnetic susceptibility values.

When we compare the RTP regional magnetic anomaly (Fig. 5.15) with the residual anomaly (Fig. 5.16), effects of the active zones of the WFB (Aluto and Shala volcanic complexes) are more pronounced on the RTP residual magnetic anomaly (Fig. 5.16). This indicates that the low magnetic susceptibility hot intrusions occurring beneath the volcano-tectonically active zones are probably buried at shallower depths (<5km).

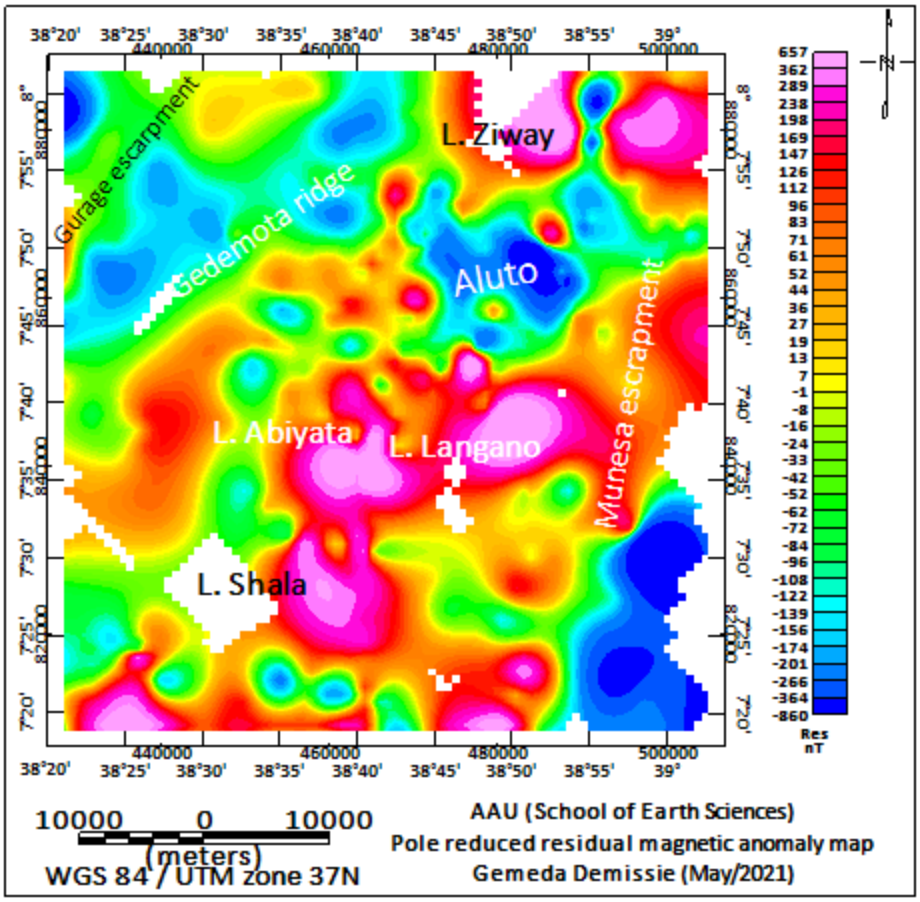

Figure 5.16 RTP residual magnetic anomaly map of the study area

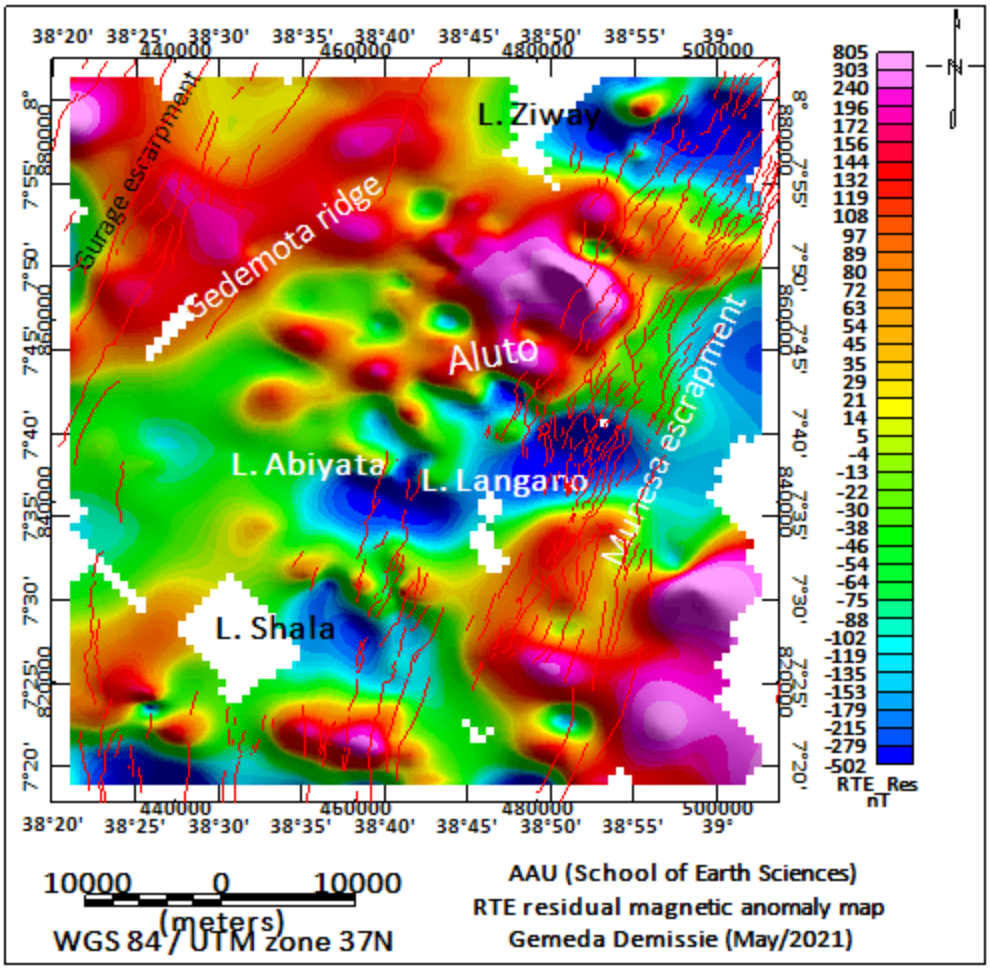

5.2.7 Analytical signal magnetic anomaly map

According to Dentith and Mudges (2014) the analytical signal of a potential field is compiled by combining the 3-directional derivatives along three orthogonal directions of the magnetic anomaly of preference at locations (x, y). The earth's total magnetic field intensity is a vector quantity which depends both on the direction and magnitude of the magnetization. Because of this it is difficult to interpret the magnetic anomaly of the equatorial region. To solve this problem, the analytical signal (AS) (a magnetic anomaly enhancement method) which doesn't depend on direction but on strength of magnetization (Lingerew Nebere, 2015) is utilized. Moreover, the analytical signal makes the interpretation of magnetic data of low magnetic latitudes (equatorial region) easier. The analytical signal (AS) (total gradient) of the magnetic anomaly ΔB of preference produced by a 3D anomalous source is expressed mathematically as:

$$AS(x,y) = \sqrt{\left(\frac{\partial \Delta B}{\partial x}\right)^2 + \left(\frac{\partial \Delta B}{\partial y}\right)^2 + \left(\frac{\partial \Delta B}{\partial z}\right)^2} \quad (5.9)$$

Where *AS(x, y)* is the amplitude of the analytic signal at point (*x*, *y*), ΔB is the observed magnetic anomaly of preference at point (*x*, *y*) and $\partial\Delta B/\partial x$, $\partial\Delta B/\partial y$ are the two horizontal derivatives and $\partial\Delta B/\partial z$ is the vertical derivative of the observed magnetic anomaly. The observed magnetic anomaly of preference can be taken to be the regional magnetic anomaly (ΔB_R) if the anomalous source has a deep origin or the residual magnetic anomaly (ΔB_{res}) if the anomalous source of interest has a shallow origin. For this thesis work the residual magnetic anomaly is preferred since the anomalous source of shallow origin is interested.

The analytical signal (AS) map (Fig. 5.17) of the study area is compiled by applying the analytical signal filter to the gridded residual magnetic anomaly map (Fig.5.16) using the Geosoft Oasis Montaj (version 7.0). The maximum gradient in the AS map (Fig. 5.17) reveals the source body and structural and/or lithological discontinuity regardless of the direction of magnetization. It is easier to infer source position from AS map (Fig. 5.17) as it enhances short wave length anomalies.

The Aluto volcanic complex is characterized by a cumulate of maximum value in the analytical signal map (Fig. 5.17) which could be a reflection of effects of the volcanic rocks. The AS map (Fig. 5.17) reasonably agrees with the geological map (Fig. 2.7) of the study area as the lithological discontinuities are clearly reflected by magnetic signal discontinuity. The lacustrine sediments extensively cover the largest portion of the geological map of the study area. And also, the area covered by this lithology is characterized by low values in the AS (Fig. 5.17) whereas the volcanic rocks both in the rift floor and its flanks are characterized by high gradients. Susceptibility contrasts in the basaltic units (Fig. 2.7) result in large analytic signal gradients as compared with the surrounding sediments and low magnetic susceptibility rock units (ignimbrite, tuffs, rhyolite and other pyroclastic volcanic rocks).

From the analytic signal map (Fig. 5.17), one can notice that all the faults mapped in the study area are not associated with high analytic signal gradients. Therefore, the geologic contacts are possibly attributed to the variation in the magnetic susceptibilities of the different geologic units (intrusive bodies, country rocks, structural contacts).

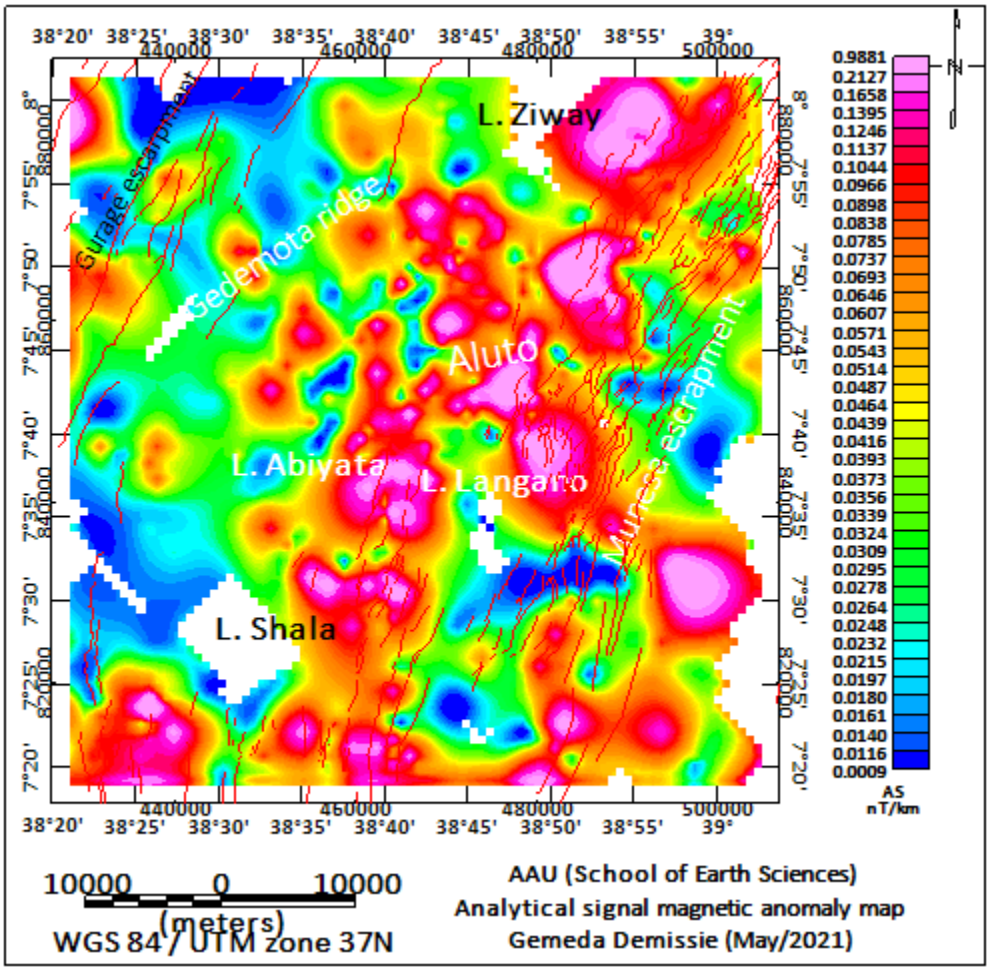

Figure 5.17 Magnetic analytic signal map of the study area

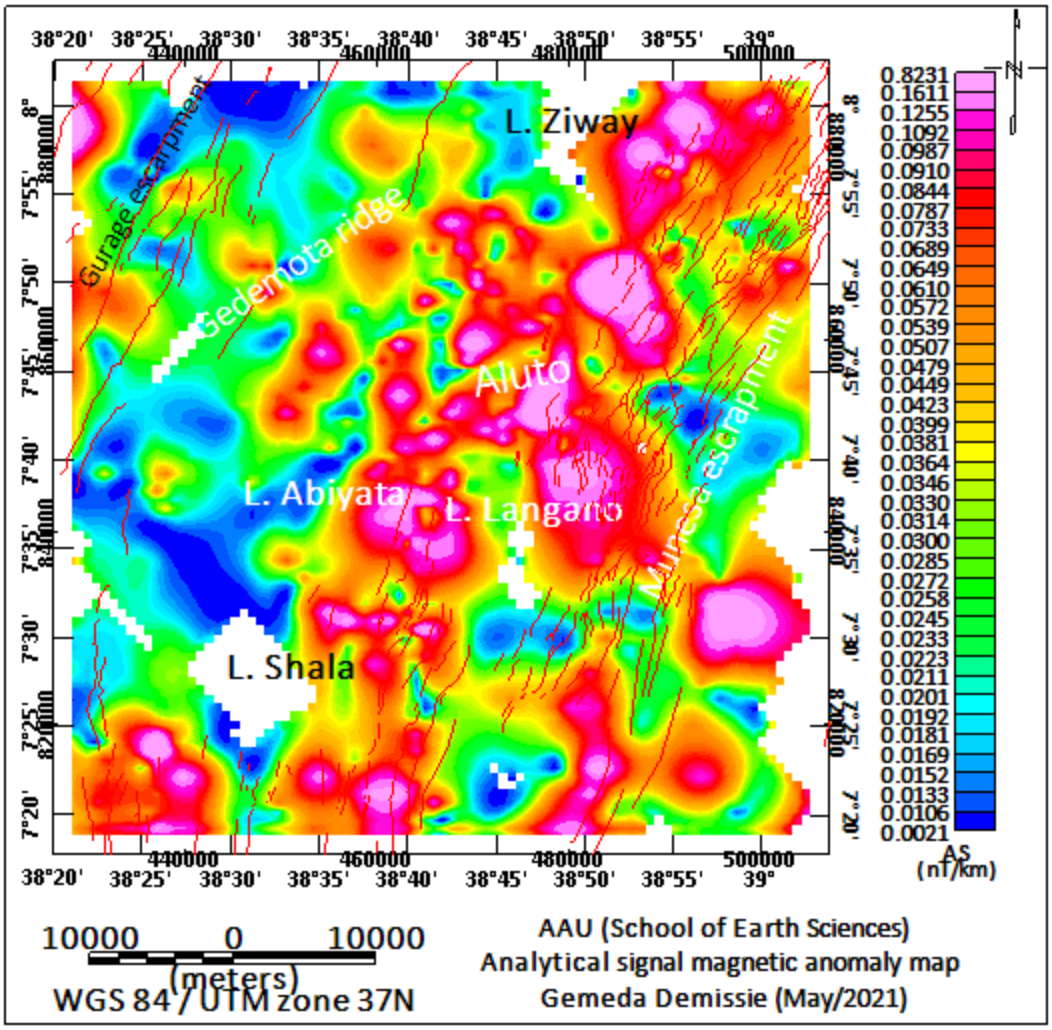

5.2.8 Tilt derivative magnetic field map

The tilt derivative map (Fig. 5.18) of the study area is compiled by applying the tilt derivative filter to the magnetic analytical signal map (Fig. 5.17) using Geosoft Oasis Montaj software (version 7.0). The map is supposed to easily identify the location of faults and geological boundaries in the study area.

Similar to the gravity tilt derivative map (Fig. 5.9) in Section 5.1.5, the magnetic tilt derivative map (Fig. 5.18) shows positive values reflecting source bodies, values close to zero (zero crossing) corresponding to discontinuities and the negative values reflecting bodies outside of the source body. Thus, the color scale in Figure 5.18 assists to identify the boundary (edge) of source bodies (yellow to dark-yellow), the outside source bodies (green to blue-black colors) and source bodies (pale pink to red).

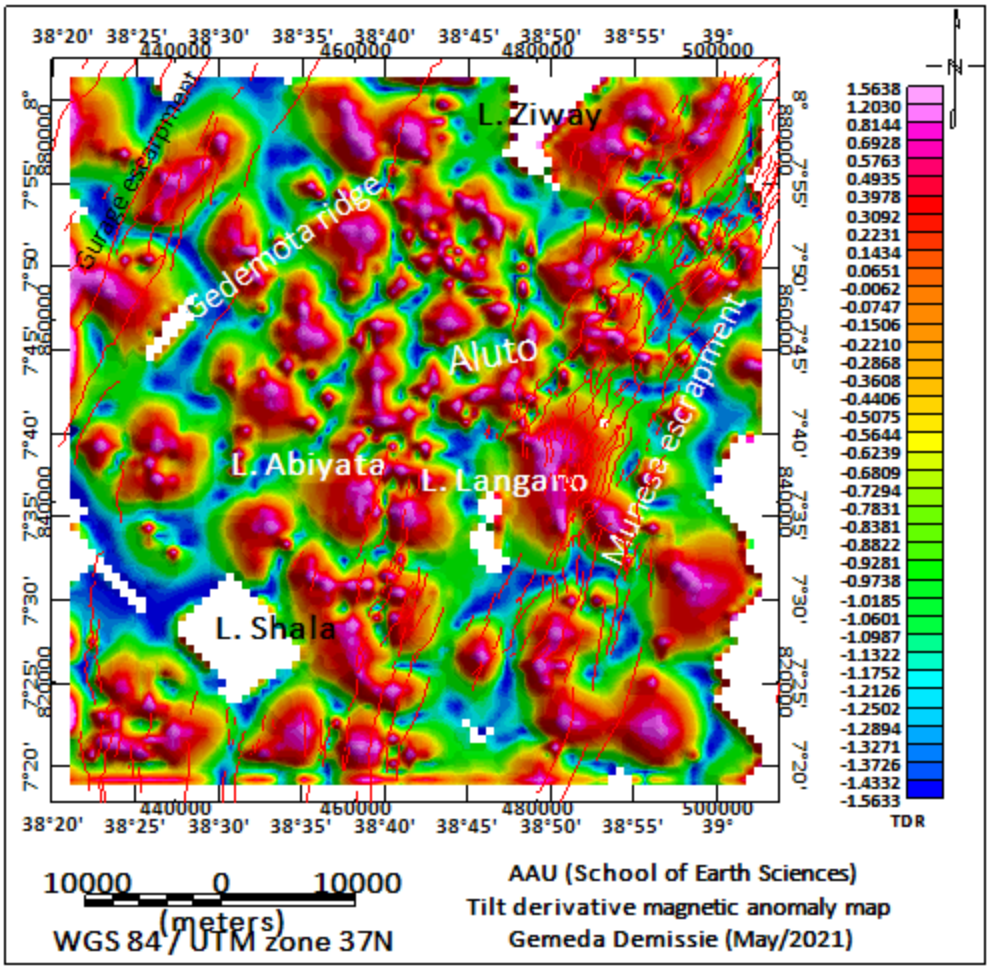

Figure 5.18 magnetic tilt derivative map of the study area. Where smooth red lines are faults

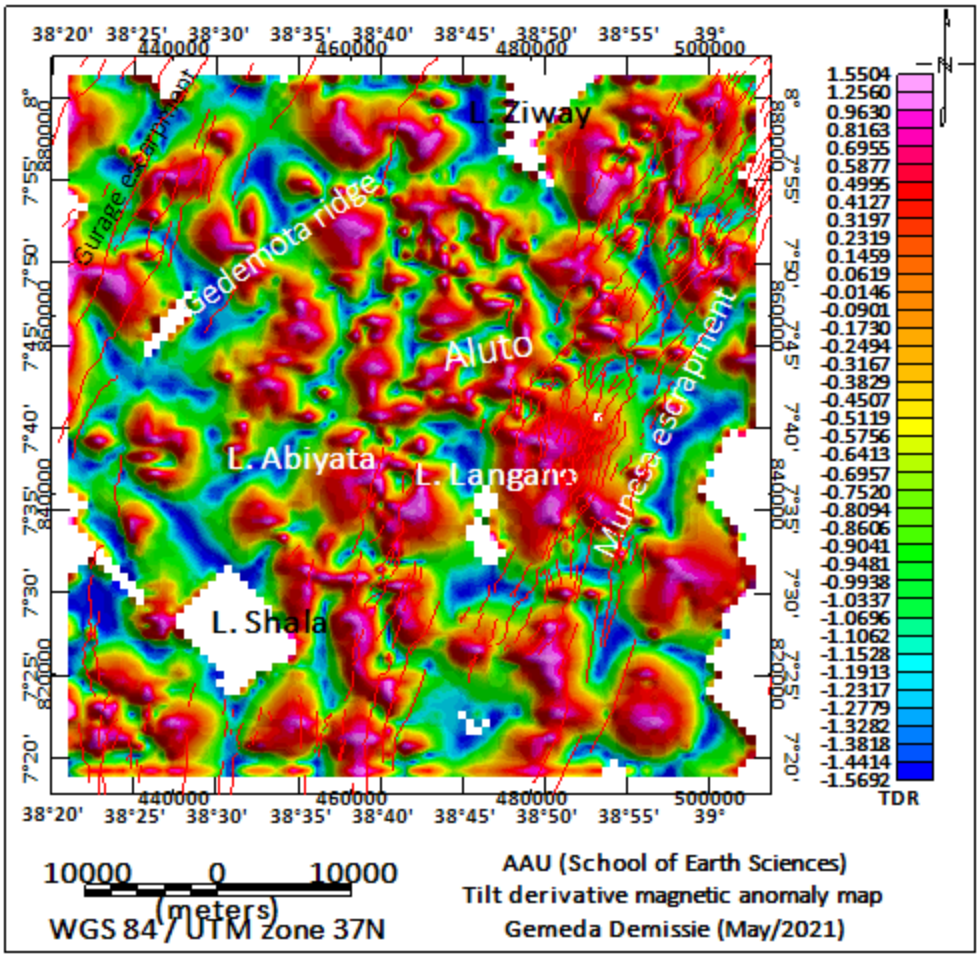

The tilt derivative map (Fig. 5.18) reveals more detailed structural contacts/boundaries than the analytical signal map (Fig. 5.17). A close examination of Figure 5.18 reveals additional information regarding the structural and lithological discontinuities in the study area in conjunction with the geological map (Fig. 2.7), structural map (Fig. 2.3) and the pole reduced residual magnetic anomaly map (Fig. 5.16). Accordingly, the study area is characterized by sets of numerous faults trending in the NNE-SSW, NE-SW and NW-SE directions being coincident with the general structural setup (Fig. 2.3) of the study area dominated by NNE-SSW and NE-SW trending structures overlaid on the tilt derivative map (Fig. 5.18).

5.2.9 Euler deconvolution magnetic map

The Euler deconvolution (ED) technique is employed in order to estimate the nature, depth and location (spatial distribution) of the magnetic sources. In standard Euler deconvolution process,

each model contains solutions of a particular structural type defined by the structural index (SI) (Table 5.1). Choice of the SI should be done using a prior knowledge of source geometry. The ED outlines different geologic bodies outlined in Table 5.1 generating either the residual or the regional anomalies in both gravity and magnetic surveys

Depth estimation for various anomaly source bodies of the Aluto-Langano geothermal field and its environs is made using the ED technique. The Euler deconvolution maps (Fig. 5.19 and Fig. 5.20) of the study area are compiled by applying a standard 3D Euler deconvolution filter to the gridded residual magnetic anomaly map (Fig. 5.16) using the Geosoft Oasis Montaj software (version 7.0). Figure 5.19 and 5.20 reveal the spatial distribution (longitude, latitude), nature and depth of the causative bodies within the study area. The optimal structural indices SI = 3 and SI = 0 are selected by a visual inspection of the maps until the best clustering of solutions is obtained. With regard to the magnetic data considered here, the structural indices SI = 3 represents a sphere (3D source) and SI = 0 represents contacts.

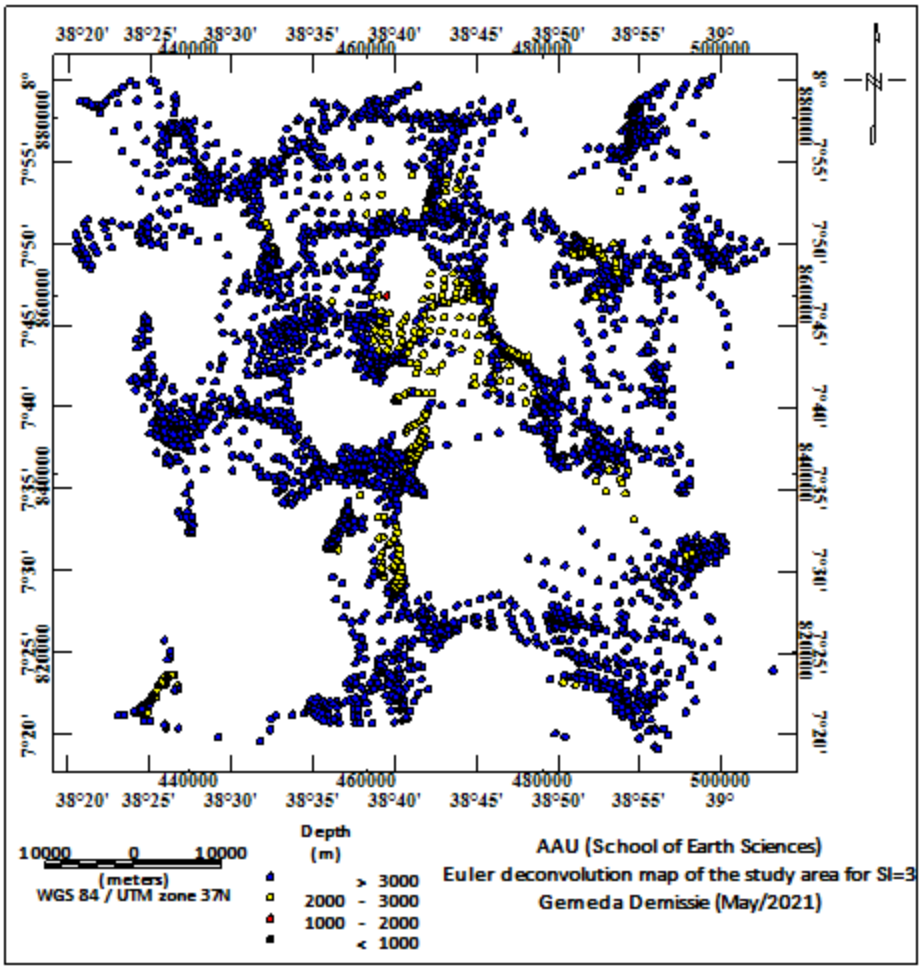

Figure 5.19 Euler deconvolution map for SI = 3

Figure 5.19 shows the depth solutions of spherical bodies buried at different depths marked by different colored symbols plotted on the map. There appear to be many solutions for 3D source bodies (blue color) buried at depths greater than 3 km beneath most parts the study area. The map also shows occurrence of 3D geologic bodies (yellow color) buried at depths ranging from 2km to 3km beneath the Aluto volcano and the Shala caldera. The occurrences of 3D bodies (yellow color) buried at depths ranging from 2km to 3km are also evident east of Lake Shala and between Lake Abiyata and Lake Langano. Figure 5.19 thus reveals a good evidence for the occurrence of a magma chamber (heat source) at shallower depths (2km-3km) beneath the Aluto and Shala volcanic complexes. Figure 5.19 also shows 3D bodies (red color) occurring at a depth range of 1km to 2km. 3D bodies occurring at depths <1km (black color) also exist in the vicinities of the Aluto volcano, Shala caldera, south of Lake Ziway and between Lake Abiyata and Lake Langano.

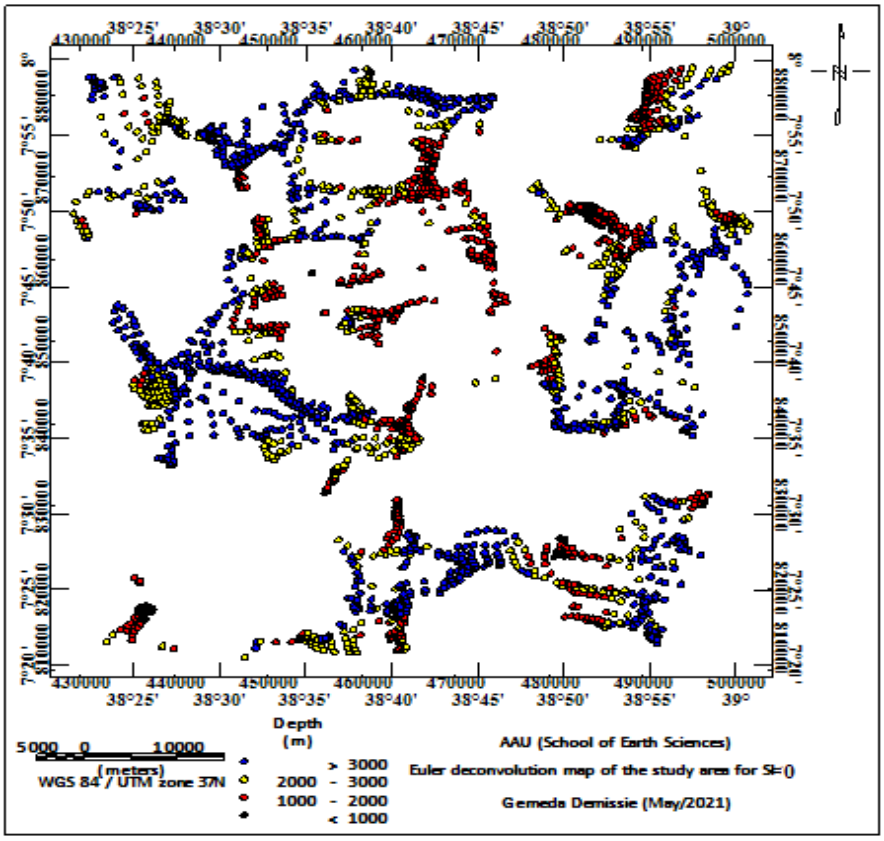

Figure 5.20 Euler deconvolution map for SI = 0

The ED map (Fig. 5.20) compiled for a structural index (SI = 0) shows depth solutions for contacts/boundaries occurring beneath the study area. The map reveals existence of linear source bodies (contacts) occurring at depths greater than 3km (blue color), 2km to 3 km (yellow color), 1km to 2km (red color) and <1km (black color) beneath the study area. The map shows the study area is dominated by linear bodies occurring at variable depths with their distribution having specific orientations on a semi-regional scale. The Munesa escarpment, Gurage escarpment, the Gedemota ridge, the corridor between Lake Abiyata and Lake Langano and the minor faults/contacts are clearly marked on the ED map (Fig. 5.20). However, the Aluto and the Shala caldera are not marked by existence of linear structures/faults. These phenomena may be due to the existence of a shallow magma chamber associated with the volcanic complexes where the rocks are in ductile (semi ductile) state and do not tend to undergo brittle deformation so as to generate contacts/faults.

CHAPTER SIX

GRAVITY MODELING

6.1 Introduction

The observed Bouguer anomaly compiled for a survey area is split into its regional and residual anomaly components and the anomaly of preference (either the regional or residual anomalies) presented in the form of profiles are employed for quantitative interpretation (Abera Alemu, 2020). However, before carrying out a quantitative interpretation of the anomalies, it is necessary to differentiate if the anomalies are generated by anomalous geologic bodies of either 2D or 3D nature. Two-dimensional (2D) model assume that the earth is two-dimensional (i.e. 2D bodies vary with depth (the Z direction) and in the direction of the profile (X direction; perpendicular to strike). 2D models do not change in the strike direction (Y direction). 2D blocks and surfaces are presumed to extend to infinity in the strike direction. GM-SYS allows profiles to be skewed (i.e. not perpendicular) to the strike of the model. The angle measured from the profile to the strike direction is entered as the "relative strike" under the *Set Azi./Strike Angle* option in the **Profile** menu. For profiles perpendicular to the strike, the relative strike is 90°. Gravity anomaly contours that are elongated in one horizontal direction in such a way that the anomaly length is at least twice the anomaly width are thought represent 2D anomalies. 2D anomalies are determined to be generated by anomalous geologic structures that theoretically extend to a large distance or to infinity in the elongate direction. Anomalous geologic bodies of 2D nature (rift valley, anticlines, synclines, horizontal dikes, vertical dikes, etc.) embedded into host rocks can be approximated to model with known 2D geometric figures. Gravity anomalies that have any shape of lateral extent in all directions represent 3D anomalies. 3D anomalies are generated by Earth materials (sedimentary basins, salt domes, ore deposits, etc.) which theoretically extend to finite distances in all directions (Abera Alemu).

Geophysical understanding of the subsurface at a local scale has an invaluable implication on shallow subsurface studies as the former is a result of key geologic processes originating in a shallower environment. With this understanding, 2D gravity models constrained by well-log data

and seismic velocity model (Maguire et al., 2006) adopted from the work of Haile Kebede et al., (2021) are constructed along two profiles drawn on the residual gravity map (Fig. 6.1). The observed residual anomaly values are extracted along profile P1 (Fig. 6.1) running across the rift axis and along profile P2 (Fig. 6.1) running along the rift axis and intentionally selected to intersect at the Aluto volcanic complex. The 2D gravity models are constructed for the purpose of sampling the shallow subsurface structures of the study area. Although gravity data in isolation suffer from non-uniqueness, they are powerful tools when used in conjunction with borehole data and seismic data.

In this thesis work, results of seismic data from the EAGLE (Maguire et al, 2006) with additional information from previous geological (e.g., Woldegebriel et al., 1990) and geophysical (e.g., Mickus et al., 2007) studies were incorporated in constructing a 2D forward gravity models along two selected profiles (P1 and P2).

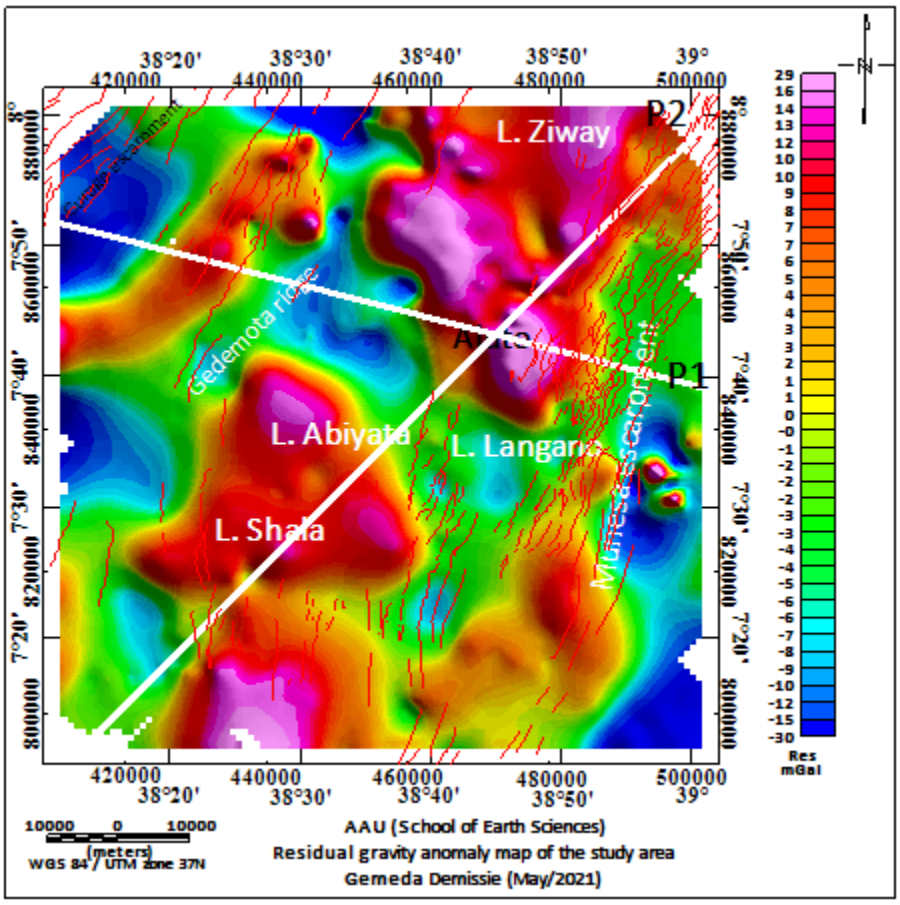

Figure 6.1 Residual gravity anomaly map. Labels: The red solid line represents faults. The line along P1 and P2 are model profile lines

6.2 Initial density model

The 2D forward gravity modeling requires a priori constraining information for the final model to be reasonable and acceptable with a least tolerable error. The required a priori information considered in this thesis work are adopted from the work of Haile Kebede et al., (2021) compiled from well-log data information, seismic velocity model (Maguire et al., 2006) and the depths determined from the spectral analysis, Werner Deconvolution and SPI (Table 6.1). The parameters obtained from this work (Table 6.1) include density, interfaces and corresponding causative source depths.

Table 6.1 Number of layers, depth to top of the layer and density value approximation for the six horizons (Adopted from the work of Haile Kebede et al., 2021)

Layer	Layer Geology	Depth to top of the layer (m)	Density (gcm^{-3})	References (Source for the parameters)
1	Pyroclastic and Lava flows (Silicic products)	0	2.477	Well-log data, Seismic study, Spectral analysis, Werner De-convolution
2	Lacustrine sediments	1000	2.34	Well-log data, Seismic study and Blaikie et al. (2014)
3	Bofa Basalt, tuff and breccias	1500	2.81	Well-log data, Seismic study, Spectral analysis, Werner De-convolution (Alemu, 1992)
4	Tertiary Ignimbrite	2500	2.58	Well-log data, Seismic study, Spectral analysis, Werner De-convolution (Alemu, 1992)
5	Mesozoic sediment	2900	2.5	(Mammo, 2010), Multi-Layer 3D gravity forward modeling
6	Crystalline basement	3000	2.74	Gravity analysis result (depth), seismic velocity-density conversion (Maguire et al., 2006)

Based on the work of Haile Kebede et al., (2021) six density layers have been identified for the initial models which include:

1. Pyroclastic and lava flows (silicic products) with a mean density of 2.477g/cm^3
2. Lacustrine sediments with a mean density of 2.34g/cm^3
3. Bofa basalts, tuffs and breccias with a mean density of 2.81g/cm^3
4. Tertiary ignimbrites with a mean density of 2.58g/cm^3
5. Mesozoic sediments with a mean density of 2.5g/cm^3 and
6. Crystalline basements with a mean density of 2.74g/cm^3

In addition to the above six main layer's, a mafic intrusion (ρ=3.0g/cm^3) inferred to occur beneath the Aluto volcano is considered in the constructed models.

6.3 2D gravity model along profile P1

The 2D gravity model (Fig. 6.2) is constructed along profile P1 running in the E-NW direction which is intended to show variation in density and lithological units across the rift axis encompassing the Aluto volcanic complex. The profile is chosen in such a way that it crosses the major structural units of the study area which include the Gedemota ridge, the Aluto volcanic complex and the Munesa escarpment. The aim of constructing this model is to characterize structure of the shallow crust in terms of geologic units (suitable for geothermal sources) related to the major volcano-tectonically active zones of the WFB in the study area.

Figure 6.2 reveals image of the shallow subsurface varying to a maximum depth of 5km constructed from the residual gravity anomaly map (Fig. 6.1) compiled for the study area. The residual gravity values extracted along profile P1 are used as an input to construct the 2D gravity profile (Fig. 6.2).

The 2D gravity model (Fig. 6.2) consists of six layers identified based on the depth/lithology and density constraints considered for the initial model (Table 6.1). A further adjustment of these model parameters resulted in a least root mean square error (RMS) of 0.324% fit between the observed and calculated gravity values (Fig. 6.2).

The top layer corresponds to the silicic products (ρ=2.477g/cm^3) with thicknesses varying from 500m to 800m.The second layer corresponds to the Lacustrine sediments (ρ=2.34g/cm^3) which cover most parts of the rift floor observed on the geological map (Fig. 2.7). The third layer matches the Bofa basalt having a density value of 2.81g/cm^3 with thicknesses varying from 400m to 600m also observed on the geologic map (Fig. 2.7). The fourth layer is attributed to the Tertiary ignimbrites (Fig. 2.7) having density value of 2.58g/cm^3 with thicknesses varying from 700m to 800m and overlying the Mesozoic sediments. The fifth layer consists of Mesozoic sediments (ρ = 2.5g/cm^3) and a mafic intrusion (ρ = 3.0g/cm^3) occurring beneath the Aluto volcano and inferred to be a magma chamber (heat source). The sixth layer comprises crystalline basement (ρ = 2.74g/cm^3) with thicknesses varying from 1000m to 1200m.

In addition to mapping the existence of magmatic intrusion beneath the Aluto volcano, the compiled model reveals a clear image of the lateral and vertical discontinuities of the geological formations and structures including faults occurring beneath the study area.

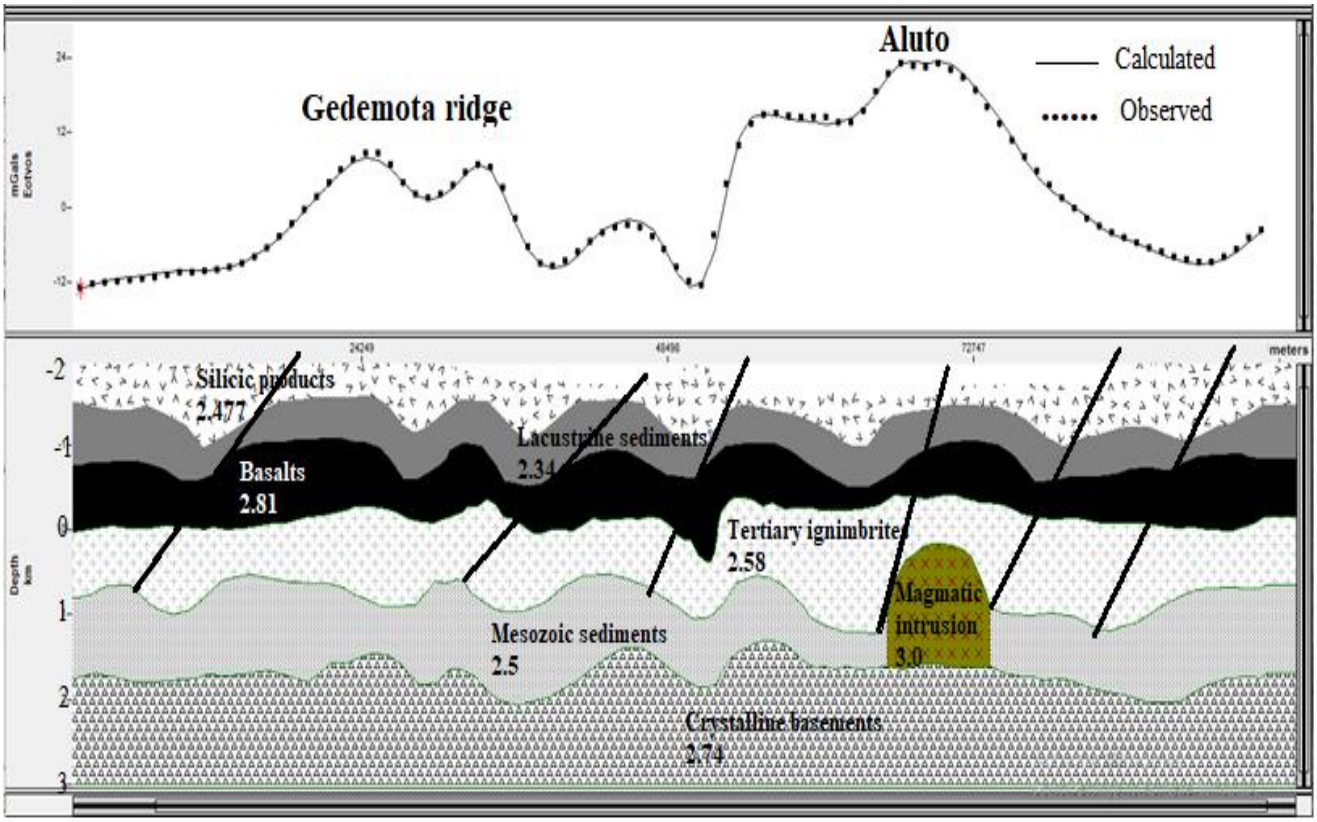

Figure 6.2 gravity models along profile P1. Density values are given in g/cm^3. Where, black bold lines are inferred faults

Figure 6.2 appears to show existence of the interaction of intrusion and fault structures which could act as conduits for the transport of a melt system. Moreover, the model (Fig. 6.2) appears to show the interaction of Quaternary faults of the WFB with the inferred mafic intrusion which could possibly supply a deeper melt to the shallow magma chambers and create favorable conditions for the occurrence of geothermal sources.

The maximum value along the gravity anomaly profile (Fig. 6.2) could be thought to be the response of a mafic intrusion (ρ=3.0g/cm^3) that occurs beneath the Aluto volcanic complex. This result is in fair agreement with the previous seismic survey results (Tiberi et al., 2005; Maguire et al., 2006) inferring the depth of the intrusion is as shallow as 3-4km. The erratic change

(maximum to minimum or vice versa) of the gravity anomaly observed at places along the gravity profile (Fig. 6.2) could be attributed to the effects of the WFB and the border faults. This effect is evidently visible on the eastern rift margin where the Munesa border fault (MBF) located. The fluctuation (up and down) of the gravity profile (Fig. 6.2) could also be attributed to the presence of grabens and horsts related to the mapped subsurface layers of the model.

6.3 2D gravity model along profile P2

The image of the shallow crust (Fig. 6.3) along the rift axis of the study area crossing the Aluto volcanic complex is constructed from the residual gravity map (Fig. 6.1). The residual gravity values extracted along profile P2 (Fig. 6.1) are used as an input to construct the 2D gravity profile (Fig. 6.3). The profile is designated to run beginning from the southwestern part of Lake Shala towards the Aluto volcanic complex which is determined to be a promising geothermal prospect site in the study area.

The density layers are the same with those of the 2D model (Fig. 6.2) compiled across the rift axis beneath the Aluto volcanic complex. However, thicknesses of each density layer and the structural patterns do not match. Due to the alignment of the gravity profile parallel to the rift axis, most of the rift floor marginal faults are not dissected by the model section. Hence, the compiled model (Fig. 6.3) does not appear to show the existence of subsurface faults and fractures occurring beneath the selected profile P2.

Six density layers identified when sampling the upper crust along profile P2 (Fig. 6.3) appear to be similar to those of the 2D gravity model compiled along profile P1 (Fig. 6.2).

Figure 6.3 reveals that the top layer corresponds to the silicic products (ρ=2.477g/cm^3) with thicknesses varying from 300m to 400m. The second layer corresponds to the Lacustrine sediments (ρ=2.34g/cm^3) which cover most parts of the rift floor observed on the geological map (Fig. 2.7). The third layer matches the Bofa basalt having a density value of 2.81g/cm^3 with thicknesses varying from 200m to 400m also observed on the geologic map (Fig. 2.7). The fourth layer is attributed to the Tertiary ignimbrites (Fig. 2.7) having density value of 2.58g/cm^3 with thicknesses varying from 500m to 800m and overlying the Mesozoic sediments. The fifth layer consists of Mesozoic sediments (ρ = 2.5g/cm^3) and a mafic intrusion (ρ = 3.0g/cm^3) occurring

beneath the Aluto volcano and inferred to be a magma chamber (heat source). The sixth layer comprises crystalline basement ($\rho = 2.74 g/cm^3$) with thicknesses varying from 1100m to 1200m.

Figure 6.3 also reveals a shallow mafic intrusion beneath the Aluto volcanic complex with its upper interface occurring at a depth as shallow as 2.5km.

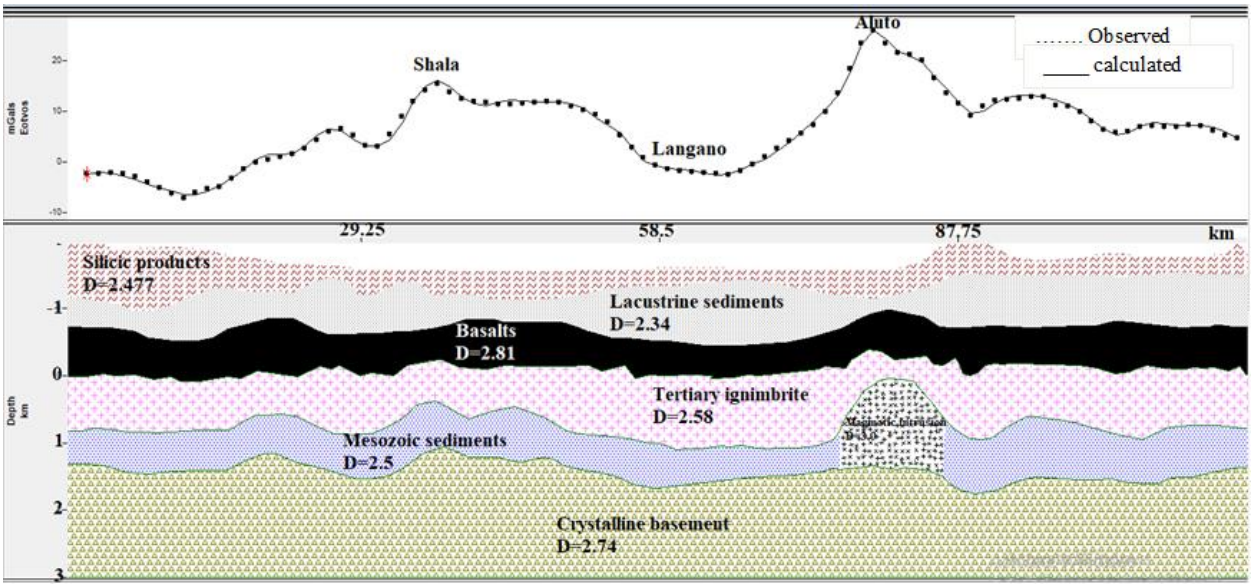

Figure 6.3 gravity model along profile P2. Density values are given in g/cm^3.

CHAPTER SEVEN

DISCUSSION AND IMPLICATIONS

7.1 Discussion

Results of the gravity and magnetic anomaly maps, profiles and models are translated into geology of the Aluto-Langano geothermal field and its environs. Evaluating these results in combination with the existing geological and geophysical data could give a better understanding about the geothermal sources occurring beneath the study area. The topographic, gravity and magnetic survey results of this study are briefly discussed in this section with a special emphasis given to the geothermal sources occurring beneath the study area.

The topographic map (Fig. 5.1) and free-air anomaly map (Fig. 5.2) reveals a clear physiographic variation of the study area. Minimum and maximum values in both elevation and free-air anomaly map indicate the rift floor and the adjacent plateaus respectively.

Intensities of the gravity and magnetic anomaly field are generally related to the subsurface geologic materials of the study area. For instance, intensity of the gravity anomaly field (Fig. 5.3) increases with decreasing elevation and vice versa. From the CBA map (Fig. 5.3), the Munesa escarpment is relatively dominated by lower Bouguer anomalies (-264mGal) as compared to the Bouguer anomalies (-232mGal) associated with the Gurage escarpment located at the northwestern extreme of the study area. This designates appearance of a steep gravity anomaly gradient over the Munesa escarpment and a lower gravity gradient over the Gurage escarpment. Moreover, the elevated platforms (shoulders of the Munesa escarpment and the Gurage escarpment) are characterized by minimum gravity anomalies ranging from -226mGal to -258mGal possibly due to the effect of crustal thickening and high elevations. On the other hand, the rift floor of the study area is characterized by relatively narrow and high complete Bouguer gravity anomaly (Fig. 5.3). Relatively narrow and high complete Bouguer gravity anomalies (Fig. 5.3) and total magnetic anomalies (Fig. 5.14) occurring over the rift floor show linear narrow zone generally oriented in a NNE-SSW and NE-SW directions. This linear narrow zone

run parallel and close to the Munesa escarpment and the Gedemota ridge connecting all the rhyolitic volcanic complexes and/or calderas related to the WFB.

The regional gravity and magnetic anomaly maps (Fig. 5.5 and Fig. 5.15) reveal that long wavelength gravity and magnetic minima occur over the shoulders of the Gurage escarpment and the Munesa escarpment. The gravity minima occurring over the Munesa and the Gurage escarpments are inferred to indicate that the escarpments are underlain either by a thick low density material or partial affected by low density asthenospheric material. The magnetic minima occurring over the escarpments are thought to indicate that the escarpments are underlain by low susceptibility volcanic materials.

The residual gravity map (Fig. 5.6) reveals two separate prominent features that correlate with gravity maxima over the rift floor and gravity minima over the Munesa and Gurage escarpments. The residual gravity maxima occurring over the rift floor are correlated with the volcano tectonically active zones of the WFB. The residual magnetic minima occurring over the Aluto volcanic complex could be thought to be the effect of low susceptibility magmatic intrusion occurring at shallow depth.

Comparison of regional gravity with the residual gravity anomaly maps shows that the strong positive anomaly zones associated with the WFB are more evident on the residual anomaly map. This indicates that the sources of these anomalous zones are most probably occurring at shallower depths. Similar results have been inferred by superimposing the fault patterns affecting the study area on the residual gravity anomaly map (Fig. 5.6) and analytic signal map (Fig.5.8). These results show that the volcanic centers are not affected by active faults, rather propagation of the fault systems are shifted/displaced at locations where they encounter the volcanic centers. This confirms the presence of hot magma chamber at shallow depth beneath these volcanic centers and behaves in a ductile manner and does not sustain brittle deformation/faulting.

The hot springs, fumaroles and alterations of volcanic rocks observed over the Aluto-Langano geothermal field are surface manifestations that indicate the presence of magmatic intrusions and magma chambers at shallow depths. Moreover, the compiled Euler deconvolution gravity map (Fig. 5.10) and Euler deconvolution magnetic map (Fig. 5.19) also show the existence of shallow heat sources beneath the Aluto volcano and other localities in the study area.

7.2 Implications

The high temperature geothermal resource of Ethiopia is located within and associated with the MER and its development is related with shallow magma chambers following the axis of the rift (Greenfield et al., 2019; Samrock et al., 2018). According to Selamawit Worku and Engdawork Admasu (2015), the geothermal resources are mainly controlled by the Quaternary structures within the rift floor. Gravity data alone does not indicate the occurrence of the geothermal resource. However, results of gravity data in conjunction with magnetic data provide vital information on key elements of the geothermal resource (e.g. heat source, reservoirs and cap rock) in the form of geologic structures. These combined potential field methods in the present study provided an insight on the deep heat sources which supply heat for shallow magma chambers/intrusions. In this study, interpretations of maps, profiles and models assisted by geologic information's reveal a good constraint not only on the deep heat sources but also the role of geological structures in melt transport to the shallow magma chambers. Gravity maxima on the CBA map (Fig. 5.3) and regional anomaly map (Fig. 5.5) in conjunction with the existing results of geological studies (Bekele Abebe et al., 2007; Ebinger et al., 2001) and geophysical studies (Bastow et al., 2010; Greenfield et al., 2019; Samrock et al., 2018) indicate the presence of deep sourced melt supply beneath the Aluto volcano-tectonic segment.

The anomaly source beneath the Aluto volcanic complex could be of shallow origin and its effect is observed to disappear on the upward continuation gravity map (Fig. 5.5 and Fig. 5.15).

The short wavelength circular shaped anomalies (Fig. 5.5) occurring over the Aluto volcanic complex could be attributed to be effects of shallow intrusion and/or magma chamber. The Quaternary fractures and/or faults of the WFB revealed by the Horizontal derivative (HDR) map (Fig. 5.7) appear to have played a great role in acting as conduits for migration of hydrothermal fluids from the heat sources (shallow magma chambers) to the surface. The Analytical signal (AS) gravity map (Fig. 5.8) reveals existence of gravity maxima over the Aluto volcanic complex which demonstrates that the occurrence of a heat source beneath the volcanic complex. This is supported by the Euler deconvolution (ED) gravity map (Fig. 5.10) which shows the occurrence of three dimensional (3D) geological bodies (e.g., hot spots and craters) buried at shallow depths (2km-3km) beneath the Aluto volcano.

The magnetic data in conjunction with the available lithological unit of the study area also reveal the presence of persistent magmatic heat sources beneath the Aluto volcano. The residual magnetic anomaly map (Fig. 5.16) shows anomaly minima over the Aluto volcano. These magnetic anomaly minima designate the existence of thick hydrothermal demagnetization zone where the rocks tend to have low magnetic susceptibility contrast.

The NNE-SSW structure evidenced by the magnetic tilt derivative map (Fig. 5.18), gravity tilt derivative map (Fig. 5.9) and surface structural map (Fig. 2.3) over the Aluto volcanic complex is attributed to create a favorable condition for the occurrence of hydrothermal fluid zones.

The gravity models (Fig. 6.1 and 6.2) in conjunction with the residual gravity (Fig. 5.5), THD gravity (Fig. 5.8), AS gravity (Fig. 5.9), TDR gravity (Fig. 5.10), ED gravity (Fig. 5.11), RTP residual magnetic (Fig. 5.16), AS magnetic (Fig. 5.17), TDR magnetic (Fig. 5.18) and ED magnetic (Fig. 5.19) maps provide important background to understand the heat source occurring beneath the Aluto volcanic complex. The 2D density model (Fig. 6.2 and Fig. 6.3) illustrate that addition of mafic materials to the upper crust provides melt for the shallow magma chamber through the Quaternary faults acting as conduits. The melt which is highly buoyant and less dense than the host rock (crystalline basement) enforced by geopressure rises through the faults and fractures to the shallow subsurface to form shallow magma chambers. Absence of a melt supply from the deeper intrusion to the shallow magma chambers may result in collapse of the magma pond forming the Aluto caldera. This process tends to create a favorable condition that favours the occurrences of geothermal resources in the central sector of the MER, specifically beneath the Aluto caldera. The younger shallow faults and cracks might have acted as conduits for the hydrothermal fluids detected at the surface as hot springs, fumaroles and altered grounds observed over the Aluto geothermal prospect site.

The gravity and magnetic survey results have clearly mapped the WFB and its relevance in relation to geothermal sources in the study area. Without the younger faults and/or fractures of the WFB there would have been no transportation of melt from the deeper intrusions to shallower magma chamber, no conduits for the migration of groundwater to the shallow magma chamber and no passage of thermal fluids to the surface which are detected as surface thermal manifestations.

CHAPTER EIGHT

CONCLUSIONS AND RECOMMENDATIONS

8.1 Conclusions

Analysis and interpretation of the gravity and magnetic data in conjunction with the available geological and geophysical data of this study have provided vital information regarding the geothermal sources of the study area. Based on the interpretations made and results obtained from geologically constrained geophysical studies conducted over the Aluto-Langano geothermal field and its environs, the following conclusions are forwarded.

- Results of the study show that anomalies of both the gravity and magnetic data are closely associated with the main lithologies and structures of the study area.
- The study area is characterized by relatively low Bouguer anomalies over the escarpments (the Munesa and the Gurage escarpments) and high anomalies over the rift axis including the Aluto volcanic complex.
- Comparison of the complete Bouguer anomaly and RTP total magnetic anomaly maps reveal that relatively high gravity anomaly values and low total magnetic anomaly values are associated with the Aluto volcanic complex. Hence, the study suggests existence of a magma chamber/magmatic intrusion acting as a heat source beneath the Aluto volcano. The high (relatively positive) gravity anomaly values suggest that the magma chamber has a high density contrast and the relatively low magnetic anomaly values suggest that the magma chamber has a low susceptibility value due to heat treatment of the rocks beneath the Aluto volcano.
- Comparison of the regional gravity and magnetic anomaly maps with the residual gravity and magnetic anomaly maps reveal that the Quaternary volcano-tectonically active zone of the WFB is more evident on the residual maps indicating that the magma chamber/intrusion related to the WFB is found at shallower depths. This phenomenon is supported by surface manifestations (hot springs, fumaroles and hydrothermally altered grounds) observed over the Aluto-Langano geothermal prospect area.

- Analytical signal and Euler deconvolution gravity maps compiled for the study area are consistent with the complete Bouguer anomaly map and its derivatives in explaining distribution of the anomaly sources beneath the rift floor and the escarpments (Munesa and Gurage escarpments). These results are found to be in fair agreement with the volcano-tectonic map and geological map of the study area.
- Analytical signal and Euler deconvolution magnetic maps compiled for the study area are consistent with the total magnetic anomaly map and its derivatives in explaining the distribution of the anomaly sources beneath the rift floor and the escarpments. These results are also found to be in fair agreement with the volcano-tectonic map and geological map of the study area.
- The computed 2D gravity models of the shallow subsurface reveal the occurrence of magma chamber/intrusion (ρ=3.0g/cm^3) extending to a depth range of 2-3km beneath the Aluto Volcanic complex.
- Results of the study infer that Quaternary faults of the WFB play a vital role in transporting melt from a deeper intrusion to a shallower magma chamber, acting as conduits for migration of surface and/or groundwater to a shallower magma chamber and transporting thermal fluid to the surface (detected as surface thermal manifestations) beneath the Aluto-Langano geothermal system.

8.2 Recommendations

- Limitation in areal coverage of magnetic data over the study area precludes interpretation of the magnetic field data (in conjunction with the available geodata) in terms of geothermal sources occurring beneath the study area. Hence, additional magnetic data could be vital for a better investigation of the geologic structures associated with the geothermal sources occurring beneath the study area.
- To understand and isolate the magnetic effect of deep and shallow geothermal sources, it is recommended to produce a general Curie isotherm map of the area which is non-existent at the moment.

References

Abera Alemu (1983). Crustal Modeling from gravity data in the Ethiopian Rift. MSc Thesis. Addis Ababa University, Addis Ababa, Ethiopia.

Abera Alemu (1992). The Gravity Field and Crustal Structure of the Main Ethiopian Rift. Report **No. 26.** TRITA GEOD 1026. Stockholm, Sweden.

Abera Alemu (2020). *Geophysics: Principles, Practices and Applications of Geophysical Methods to Resource Exploration and Geohazard Studies*. Addis Ababa, Ethiopia, 115-272 pp.

Abera Tessema, and Antoine, L.A.G. (2004). Processing and interpretation of the gravity field of the East African Rift: implication for crustal extension. Tectonophysics, **394**: 87–110.

Baker, B.H, Mohr, P.A. and Williams, L.A.J. (1972). Geology of the East Rift System of Africa. Geo.Soc. Am., Spec. Paper., 136:67pp

Baker, J.A., Thirlwall, M.F. and Menzies, M.A. (1996). Sr-Nd-Pb isotopic and trace element evidence for crustal contamination of plume-derived flood basalts: Oligocene flood volcanism in western Yemen, *Geochimica et Cosmochimica Acta*, **60**: 2559– 2581.

Bastow, I. D., Pilidou, S., Kendall J.M., and Stuart, G. W. (2010). Melt induced seismic anisotropy and magma assisted rifting in Ethiopia: Evidence from surface waves, Geochem. *Geophy., Geosys.* **11**: 05-11.

Berhanu Gizaw. (1989). Geochemical investigation of the Aluto-Langano Geothermal field, Ethiopian Rift Valley. Unpublished MPH. Thesis, Department of Earth Science, University of Leeds, 237 pp.

Befekadu Oluma, Abiy Hunegnaw, Mohammedberhan, A. and Ketsela Tadesse (1986). Geothermal Exploration Project Lakes: Corbetti Geothermal Prospect, Geophysical Exploration.

Bekele Abebe, Acocella, V., Tesfaye Korme and Dereje Ayalew (2007). Quaternary faulting and volcanism in the Main Ethiopian Rift. *J. Afr. Earth Sci*. **48**: 115–124.

Biggs, J., Bastow, I. D., Keir, D. and Lewi, E. (2011). Pulses of deformation reveal frequently recurring shallow magmatic activity beneath the Main Ethiopian Rift, *Geochem. Geophy., Geosyst.* **12**: 0-10.

Blakely, R.J. and Simpson, R.W. (1986). Approximating edges of source bodies from magnetic or gravity anomalies. *Geophysics*, **51**: 1494–1498.

Blakely, R.J. (1995). Potential Pheory in Gravity and Magnetic Applications. Cambridge University Press, Cambridge, 321pp.

Boccaletti, M., Mazzuoli, R., Bonini, M., Trua, T. and Bekele Abebe (1999). Plio-Quaternary volcano-tectonic activity in the northern sector of the Main Ethiopian Rift (MER): relationships with oblique rifting, *J. Afr. Earth Sci.* **29**: 679–698.

Bonini, M., Corti, G., Innocenti, F., Manetti, P., Mazzarini, F., Tsegaye Abebe and Pecskay Z. (2005). Evolution of the Main Ethiopian Rift in the frame of Afar and Kenya rifts propagation, retrieved from http://dx.doi:10.1029/2004TC001680 on 20.11.2019.

Casey, M., Ebinger, C.J., Keir, D., Gloaguen, R. and Mohamad, F. (2006). Strain accommodation in transitional rifts: extension by magma intrusion and faulting in Ethiopian magmatic segments, *Geol. Soci*. **259**: 143–163.

Corti, G. (2009). Continental rift evolution: from rift initiation to incipient break-up in the Main Ethiopian *Rift. East Afr. Earth Sci.* **96**: 1–53.

Corti, G., Sani, F., Philippon, M., Sokoutis, D., Willingshofer, E. and Molin, P. (2013). Quaternary volcano-tectonic activity in the Soddo region, western margin of the Southern Main Ethiopian Rift. *Tectonics*. **32**: 861–879. doi:10.1002/tect.20052.

Dentith, M. and Mudge, S. (2014). Geophysics for the Mineral Exploration Geoscientist. Cambridge university press, New York, 426 pp.

Di Paola, G.M. (1972). The Ethiopian Rift Valley (between 7^0 and 8^0 40' lat. North). *Bulletin of Volcanology*, **36**: 517–560.

Dobrin, M.B. and C.H. Savit (1988). Introduction to Geophysical Prospecting, 4th Edition, McGraw-Hill, London.

Ebinger, C. (2005). Continental breakup: the East African perspective. *Astronomy and Geophysics*, **46 (2)**: 16–2.21.

Ebinger, C. J., and Casey, M. (2001). Continental breakup in magmatic provinces: *An Ethiopian example*, *Geology*, **29**: 527–530.

Ebinger, C. J., Yemane, T., Harding, D. J., Tesfaye, S., Kelley, S. S. and Rex, D. C. (2000). Rift deflection, migration, and propagation: Linkage of the Ethiopian and Eastern rift. *Africa, Geol. Soc. Am. Bull.* **112**: 163–176.

ELC Electroconsult, 1986, Exploitation of Aluto-Langano geothermal resources feasibility report, Geothermal Exploration Project, Ethiopian Lake District Rift: Milan, Italy, ELC Electroconsult, 289 p.

ELC Electroconsult . (2015). Geothermal Surface Exploration in Aluto Langano, Ethiopia. Milano - Italy.

ELC Electroconsult, (2016). *Gravimetric report in Aluto Langano area, Ethiopia.* Milano, Italy, 10 pp.

Engdawork Admasu and Selamawit Worku (2015). Characterization of Quaternary Extensional Structures: Tulumoye Geothermal Prospect, Ethiopia. *GRC Transact*. **39**: 25-32.

Ernst and Nihon, Y. S. (2010). *Study on geothermal power development project in the Aluto Langano Field, Ethiopia*, West Japan Engineering Consultants, Inc. .125 pp.

Giday Woldegebriel, Aronson J. L., and Walter R. C. (1990) Geology, geochronology, and rift basin development in the central sector of the Main Ethiopia Rift, *Geol. Society of America Bulletin* **102**: 439-458.

Greenfield, T., Keir, D., Kendall, J.M. and Atalay Ayele (2019). Seismicity of the BoraTulumoye volcanic field, 2016– 2017, *Geochem. Geophys. Geosyst*. **20**: 548–570.

Giday Woldegebriel, Heiken, G., White, T.D., Berhane, A., Hart, W.K., Renne, P.R. (2000). Volcanism, tectonism, sedimentation, and the paleoanthropological record in the Ethiopian Rift System. **In**: McCoy FW, and Heiken G., (Eds.), Volcanic Hazards and Disasters in Human Antiquity. *Geological Society of America Special Paper,* **345**: 83-99

Hayward, N.J. and Ebinger, C. J. (1996). Variations in the along-axis segmentation of the Afar Rift system. *Tectonics,* **15**: 244-257.

Heiskanen, W.A. and Moritz, H., (1967). Physical Geodesy, Freeman, San Francisco.

Hill, D. P., Bailey, R. A. and Ryall, A. S. (1985). Active tectonic and magmatic processes beneath Long Valley Caldera, *eastern California,* **3**: 111-120.

Hinze, W.J., von Frese, R.R. and Saad, A.H. (2013). Gravity and Magnetic Exploration: Principles, Practices, and Applications, Cambridge University Press, New York, 550 pp.

Hoffman, C., Courtillot, V., Féraud, G., Rochette, P., Gezahegn Yirgu, Ketefo, E. and Pik, R. (1997). Timing of the Ethiopian basalt event and implications for plume birth and global change, Nature, 389: 838–841.

Hutchison, W.A., Mother, T.A., Pyle, D.M., Biggs, J. and Gezahegn Yirgu (2015). Structural controls on fluid pathways in an active rift system: A case study of the Aluto volcanic complex, Geosphere, 11: 1-21.

Jacobsen, B.H., (1987). A case for upward continuation as a standard separation filter for potential-field maps. *Geophysics,* **52**:1138–1148.

Kazmin, V. (1980), Transform faults in the East African Rift system, Atti Convegni Lincei, 47, 65 – 73.

Kazmin, V. and Berhe, S., (1978). Geology and development of the Nazreth area. Ethiopian Institute of Geological Survey.

Kazmin, V., Seifemichael Berhe, Nicoletti, M. and Petrucciani, C. (1980). Evolution of the northern part of the Ethiopian Rift. Accad. 47: 275–291.

Kearey, P. Brooks. M. and Hill, I. (2002). An Introduction to Geophysical Exploration, 3rd ed., Blackwell Science Ltd. Britain, 257 pp.

Keir, D., Ebinger, C.J., Stuart, G.W., Daly, E. and Atalay Ayele (2006). Strain accommodation by magmatism and faulting as rifting proceeds to breakup: seismicity of the northern Ethiopian rift, retrieved from http://dx.doi.org/10.1029/2005JB003748 on 06.02. 2020.

Keranen, K., Klemperer S. L., Gloaguen R. and the EAGLE working group (2004). Three dimensional seismic imaging of a protoridge axis in the Main Ethiopian rift, *Geol.* **32**:949-952.

Keranen, K., Klemperer, S.L., Julia, J., Lawrence, J.L. and Nyblade, A. (2009). Low lowercrustal Velocity across Ethiopia: Is the Main Ethiopian Rift a narrow rift in a hot craton?, retrieved from http://dx.doi.org/10.1029/2008GC002293 on 11.03.2019.

Kieffer, B., Arndt, N., LaPierre, H., Bastien, F., Bosch, D., Pecher, A., Gezahegn Yirgu, Dereje Ayalew, Weis, D., Jerram, D., Keller, F. and Meugniot, C. (2004). Flood and shield basalts from Ethiopia: Magmas from the African Superswell, J. Petrology 45: 793–834.

Le Turdu, C., Tiercelin, J.J., Gibert, E., Travi, Y., Lezzar, K.E., Richert, J.P., Massault, M., Gasse, F., Bonnefille, R., Decobert, M., Gensous, B., Jeudy, V., Tamrat, E., Mohammed, M.U., Martens, K., Balemwal Atnafu, Tesfaye Cherent, Williamson, D. and Taieb, M. (1999). The Ziway– Shala Lake basin system, Main Ethiopian Rift: influence of volcanism, tectonics and climatic forcing on basin formation and sedimantation. *Palaeogeography, Palaeoclimatology, Palaeoecology*, **150**: 135–177.

Lillie, R. J. (1999). Whole Earth Geophysics: An Introduction text to geologists and geophysicists. Prentice-Hall, Inc. Upper Saddle River, New Jersey, USA

LIoyd, E. F. (1977). Geological factors influencing Geothermal Exploration in the Langano Region, Ethiopia. NZ Geological Survey, Rotorua, New Zealand. Unpublished Report. PP.73

Lingerew Nebere (2017). Reduction to the pole and analytic signal interpretation technique of magnetic data in equatorial area, Ethiopia. *International journal of scientific Engineering and research,* **5**: 466-468.

Lowrie, W. (2007). Fundamentals of Geophysics. 2 nd ed., Cambridge University Press, New York, 357 pp.

Matthew, M., Bonaccorso, A. and Guglielmino, F. (2007). Ground deformations in the Island of Pantelleria (Italy): Insights into the dynamic of the current interruptive period, *Geophys. Resis*. J. **112**: 25-40

Mege, D., and Tesfaye Korme (2004). Dyke swarm emplacement in the Ethiopian Large Igneous Province: Not only a matter of stress. *Journal of Volcanology and Geothermal Research,* **132**: 283–310.

Mekuria, N., Gizaw, B., Teklu, A. and Gizaw, T. (1987), Geochemistry of the Aluto-Langano geothermal field, Ethiopia, *Ethiopian Institute of Geological Surveys, Internal Report*, **5**: 1-55.

Merga Tassew (2015). Expansion Work and Experience Gained in Operation of Aluto Langano Geothermal Power Plant. *Addis Ababa, Ethiopian Electric Power.*

Meseret Teklemariam (2006). Overview of geothermal resource utilization and potential in East African Rift System. Geothermal Resource Council, Transactions 2006.

Meseret Teklemariam. (1996). Water-rock interaction Processes in the Aluto-Langano geothermal field, Ethiopia. PhD. Thesis, Department of Earth Sciences, University of Pisa, 295 pp.

Meseret Teklemariam & Kibret Beyene (2000).Geochemical monitoring of the Aluto-Langano Geothermal Field, Ethiopia. Addis Ababa.

Meseret Teklemariam and Kibret Beyene (2001). Geochemical monitoring of the Aluto-Langano geothermal field, Ethiopia. **In:** *Proceedings of Twenty-Sixth Workshop on Geothermal Reservoir Engineering* pp. 1-25, *Geological survey of Ethiopia, Addis Ababa, Ethiopia 20*

Meseret Teklemariam and Kibret Beyene (2002). Geochemical Monitoring of the Aluto-Langano Geothermal Field, Ethiopia. Addis Ababa.

Meseret Teklemariam and Solomon Kebede (2010). Strategy for Geothermal Resource Exploration and Development in Ethiopia. *Geological Survey of Ethiopia, Addis Ababa, Ethiopia.*

Meyer, W., Pigler, A., Rosler, A. and Stets, J. (1975). Tectonic evolution of the Main Ethiopian Rift in southern Ethiopia. Schweizerbart, Stuttgart, 352–361.

Mickus, K., Ketsela Tadesse, Keller, G.R. and Befekadu Oluma (2007). Gravity analysis of the main Ethiopian rift, *J. Afr. Earth Sci.* **48**: 59–69.

Miller, H.G. and Singh, V. (1994). Potential field tilt-a new concept for location of potential field sources. J. Appl. Geophys, 32: 213–217. Mohr, P. (1962). The Ethiopian Rift System. *Bulletin of the Geophysical Observatory of Addis Ababa,* **5**:33-62.

Milsom, J. (2003). Field Geophysics: The Geophysical Guide Field Series. Third edition. John Wiley and Sons Ltd. West Sussex, England.

Mohr, P.A., 1966: Chebbi Volcano (Ethiopia), bull.volcanol, 29, p797 – 810.

Mohr, P. (1967). The Ethiopian Rift System. Bulletin of the Geophysical Observatory of Addis Ababa, 11: 1–65.

Mohr P. (1971). Outline of tectonics of Ethiopia. Tectonics of Africa, 4: 445- 458.

Mohr, P.A. (1983). Volcanotectonic aspects of the Ethiopian Rift evolution. *Bull. Cent. Rech. Explor. Prod. Elf – Aquitaine*. **7**: 175–189.

Mohr, P. and Zanettin, B. (1988). The Ethiopian flood basalt province. Kluwer Academic Publishers, 4: 63–110

Moore, J. N., Allis, R. G., Nemcok, M., Powell, T. S., Bruton, C. J., Wannamaker, P. E., Raharjo, I. B. and Norman, D. I. (2008). The evolution of volcano-hosted geothermal systems based on deep wells from Karaha-Telaga Bodas, Indonesia, *American Journal of Science,* **308**: 1–48.

Nafe J.E. and Drake C. L. (1957). Variation with depth in shallow and deep water marine sediments of porosity, density and the velocities of compressional and shear waves. *Geophysics*, **22**: 523-552.

Pierrick, A. (2015). Gravimetry for geothermal exploration. Doctoral Dissertation, University of Neuchâtel, Switzerland, 223 pp.

Putri, D., Nanda, M., Rizal S., Idroes, R., and Ismail, N. (2019). Interpretation of gravity satellite data to delineate structural features connected to geothermal resources at Bur Ni Geureudong geothermal field, **In**: *proceedings of the 3rd International Conference on Natural and Environmental Sciences*, pp.6, Syiah Kuala, Indonesia.

Reynolds, J.M. (1997). An Introduction to Applied and Environmental Geophysics. John Wiley and Sons Ltd, England, UK, 799 pp.

Samrock F., Grayver, A. V., Eysteinsson, H. and Saar, M. (2018). Magnetotelluric image of transcrustal magmatic system beneath the Tulumoye geothermal prospect in the Ethiopian Rift, *Geophys. Research Letters*, **45**: 847–855.

Selamawit Worku (2016). Sub-surface geology, hydrothermal alteration and 3d modeling of wells la-9d and la-10d in the Aluto Langano geothermal field, Ethiopia. Master's thesis,University of Iceland, 103 pp.

Solomon Kebede, Tadesse Mamo and Tsegay Abebe (1984). Explanation to the Geologic Map of Aluto-Langano Geothermal Area. *EIGS Report With Accompanying 1:20,000 Scale Geologic Map of Aluto Volcano.* 261: 57.

Solomon Kebede (2016). Country update on geothermal exploration and development in Ethiopia. **In:** Proceedings of the 6th African Rift Geothermal Conference pp.1-15, Addis Ababa, Ethiopia.

Tadiwos Chernet, Hart, W. K., Aronson, J. L. and Walter, R. C. (1998). New age constraints on the timing of volcanism and tectonism in the northern main Ethiopian rift– southern Afar transition zone, Ethiopia, *Journal of Volcanology and Geothermal Research*, **80**: 267-280.

Teklu, A. (2004). Geochemical study of the Aluto-Langano Geothermal Field and the surrounding area. Ethiopia, Addis Ababa.

Telford, W.S, Geldart, L.P. and Sheriff, R.E. (1990). Applied Geophysics, 2nd ed., Cambridge University Press, Cambridge, UK, 784 pp.

Tenalem Ayenew (1998). The hydrogeological system of the lake district basin, Ethiopia. P.HD. thesis, ITC, Enschede, the Netherlands. 259pp

Tilahun Mammo (2010). Delineation of sub-basalt sedimentary basins in hydrocarbon exploration in North Ethiopia. *Marine and petroleum geology,* **27**: 895–908.

Thompson D.T. (1982). A new technique for making computer-assisted depth estimates from magnetic data. *Geophysics,* **47**: 31–37.

Tsegaye Abebe (2000). *Limitations of a geothermal system in a continental rift zone: example the Ethiopian rift valley*, World Geothermal Congress, Kyushu – Tohoku, Japan.

Tsegaye Abebe, Manetti, P., Bonini, M., Corti, G., Innocenti, F., Mazzarini, F. and Pecskay, Z. (2005). Geological map (scale 1: 200,000) of the northern Main Ethiopian Rift and its implication for the volcano-tectonic evolution of the rift, *Geol. Soc. Am.* **821**: 51-97.

Tsegaye Abebe, Balestrieri, M.L. and Bigazzi, G. (2010). The Central Main Ethiopian Rift is younger than 8 Ma: Confirmation through apatite fission – track thermochronology, *Terra Nova,* **22**: 470–476.

Wilks. M., Rawlinson, N., Kendall, J.M. Nowacki, A. Biggs, J. Ayele, A. and Wookey, J. (2020). Coupled Magmatic and Hydrothermal Systems of the Restless Aluto Caldera, Ethiopia, retrieved from https://doi.org/10.3389/feart.2020.579699 on 02.20.2020

Wolfenden, E. (2003). Evolution of the southern Red Sea Rift: Birth of a magmatic margin. PhD thesis, Royal Holloway, University of London, UK, 150 pp.

Wolfenden, E., Ebinger, C., Gezahegn Yirgu, Deino, A. and Dereje Ayalew (2004). Evolution of the northern Main Ethiopian rift: birth of a triple junction, *Earth and Planetary Science Letters,* **224**: 213–228.

Yaogauo, L., and Oldenberg, D.W. (2001). Stable reduction to the pole at the magnetic equator. *Geophysics*, **66**: 571-578.